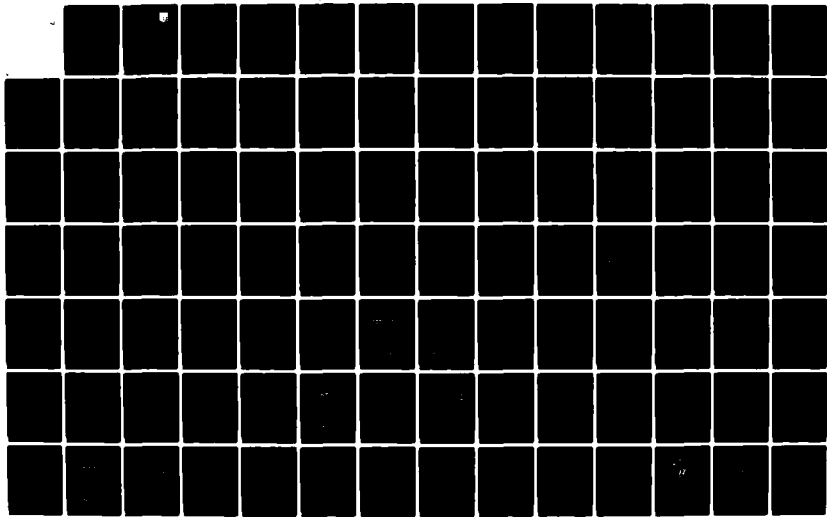AD-A141 739   ACTIVE SUPPRESSION OF AEROELASTIC INSTABILITIES FOR   1/2
              FORWARD SWEPT WINGS(U) AIR FORCE WRIGHT AERONAUTICAL
              LABS WRIGHT-PATTERSON AFB OH   T E NOLL ET AL. DEC 83
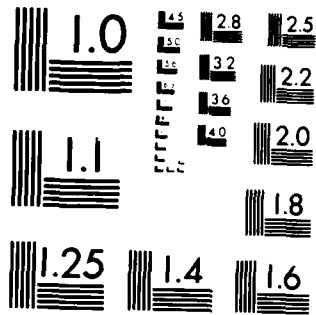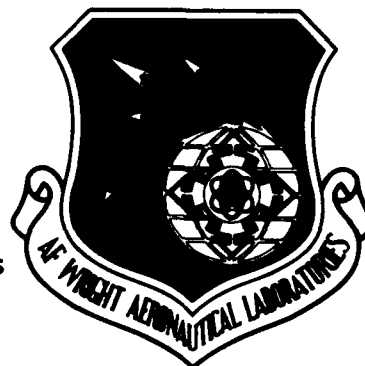UNCLASSIFIED AFWAL-TR-84-3002   F/G 1/1   NL

MICROCOPY RESOLUTION TEST CHART
NATIONAL BUREAU OF STANDARDS 1963 A

AD-A141 739

AFWAL-TR-84-3002

Active Suppression of Aeroelastic Instabilities
for Forward Swept Wings

T. E. Noll
Flight Dynamics Laboratory
Air Force Wright Aeronautical Laboratories

F. E. Eastep
University of Dayton

and

R. A. Calico
Air Force Institute of Technology

December 1983

Final Technical Report for the period January 1982 - December 1983

DTIC
ELECTE
MAY 3 1 1984
S   E
D

FLIGHT DYNAMICS LABORATORY
AIR FORCE WRIGHT AERONAUTICAL LABORATORIES
AIR FORCE SYSTEMS COMMAND
WRIGHT-PATTERSON AIR FORCE BASE, OH 45433

DTIC FILE COPY

84   05   30   098

THOMAS E. NOLL
Project Engineer
Aeroelastic Group
Analysis & Optimization Branch

FREDERICK A. PICCHIONI, LT COL, USAF
Chief, Analysis & Optimization Branch
Structures & Dynamics Division

FOR THE COMMANDER

RALPH L. KUSTER, JR., COL, USAF
Chief, Structures & Dynamics Division

REPORT DOCUMENTATION PAGE	READ INSTRUCTIONS BEFORE COMPLETING FORM

1. REPORT NUMBER AFWAL-TR-84-3002	2. GOVT ACCESSION NO. AD-A141739	3. RECIPIENT'S CATALOG NUMBER

4. TITLE (and Subtitle) Active Suppression of Aeroelastic Instabilities for Forward Swept Wings	5. TYPE OF REPORT & PERIOD COVERED Final Report January 1982 – December 1983
	6. PERFORMING ORG. REPORT NUMBER In-House

7. AUTHOR(s) Thomas E. Noll, Franklin E. Eastep and Robert A. Calico	8. CONTRACT OR GRANT NUMBER(s)

9. PERFORMING ORGANIZATION NAME AND ADDRESS Analysis and Optimization Branch Flight Dynamics Laboratory Air Force Wright Aeronautical Laboratories Wright-Patterson AFB OH 45433	10. PROGRAM ELEMENT, PROJECT, TASK AREA & WORK UNIT NUMBERS Project 2401 Task 240102 Work Unit 24010239

11. CONTROLLING OFFICE NAME AND ADDRESS Air Force Wright Aeronautical Laboratories Air Force Systems Command Wright-Patterson AFB OH 45433	12. REPORT DATE December 1983
	13. NUMBER OF PAGES 170

14. MONITORING AGENCY NAME & ADDRESS(if different from Controlling Office)	15. SECURITY CLASS. (of this report)
	15a. DECLASSIFICATION/DOWNGRADING SCHEDULE

16. DISTRIBUTION STATEMENT (of this Report)

Approved for public release; distribution unlimited

17. DISTRIBUTION STATEMENT (of the abstract entered in Block 20, if different from Report)

18. SUPPLEMENTARY NOTES

19. KEY WORDS (Continue on reverse side if necessary and identify by block number)

Aeroelasticity
Active Feedback Controls
Forward Swept Wing
Flutter
Divergence

20. ABSTRACT (Continue on reverse side if necessary and identify by block number)

Analytical studies are conducted to investigate the potential of using active feedback control systems for preventing multiple aeroelastic instabilities (in close proximity) from occurring within the flight envelope of an advanced forward swept wing aircraft. With the addition of wing mounted external stores, the classical bending/torsion flutter instability is driven to lower airspeeds into the vicinity of the aeroelastic instabilities more commonly associated with a forward swept wing (divergence or body freedom flutter). For these studies a typical forward swept wing configuration, adversely mass ballasted to create

DD FORM 1 JAN 73 1473   EDITION OF 1 NOV 65 IS OBSOLETE

BLOCK 20 (Cont'd)

the dynamic characteristics similar to those caused by adding external stores, is investigated. The goal of this study is to establish concept feasibility so that the technology can be considered for future aircraft application during a design as an alternative or option for preventing aeroelastic instabilities. Analyses are conducted to design active systems for the forward swept wing, cantilevered, free in rigid pitch only, and free in rigid pitch and plunge. They are designed such that both aeroelastic instabilities are suppressed simultaneously to a velocity 20 percent above the unaugmented bending/ torsion flutter speed with gain margins of at least ± 6db at this speed condition. Obtaining large phase margins is also taken into consideration during the design analyses. The study presents the logic used in designing the various systems and provides data that demonstrate the adequacy and sensitivity of the system over the velocity range of interest. Root locus design procedures and Pade' polynomial approximations of the doublet-lattice unsteady aerodynamic force coefficients are used in the development of the various systems. The use of two wing control surfaces is found to be the most promising for this application. A leading edge control surface commanded by displacement is used to prevent the instabilities related to the divergence tendencies of the first bending mode while a trailing edge surface commanded by angular acceleration controls the higher frequency bending/torsion flutter mode.

FOREWORD

The research presented in this report was supported by the
Air Force Wright Aeronautical Laboratories (AFWAL). The work was per-
formed between January 1982 and December 1983. Dr Thomas Noll was the
principal investigator.

AFWAL support was directed by the Aeroelastic Group, Analysis and
Optimization Branch, Structures and Dynamics Division, Flight Dynamics
Laboratory under work unit number 24010239, "Aeroelastic Study of
Swept Wings with Anisotropic Behavior".

Accession For	
NTIS GRA&I	X
DTIC TAB	☐
Unannounced	☐
Justification	
By	
Distribution/	
Availability Codes	
Dist	Avail and/or Special
A-1	

iii
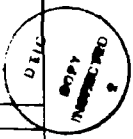
TABLE OF CONTENTS

LIST OF ILLUSTRATIONS

LIST OF TABLES

XIII

LIST OF SYMBOLS

A	State Space Matrix
A_i	Matrix Polynomial Coefficients of Unaugmented Equations of Motion
b	Reference Semichord
c	Linear Distance
C_i	Aerodynamic Polynomial Coefficient Matrices
C_{ij}	Generalized Damping
d	Dumbbell Distance
D_i	Denominator Polynomial Coefficient
$\bar{D}_i$	Average Denominator Polynomial Coefficient
e	Static Unbalance
F	Force
F_n	Matrix Polynomial Coefficients of Unaugmented Equations of Motion
g	Structural Damping
h	Displacement
h_i	Modal Participation Coefficients
i	$\sqrt{-1}$
I	Identity Matrix
I_α	Inertia
J	Quadratic Cost Function
k	Reduced Frequency
K	Feedback Gain

K_{ij}	Generalized Stiffness
m	Mass
M	Magnitude of Transfer Function
M_{ij}	Generalized Mass
N_i	Numerator Polynomial Coefficient
P_j	Pressure
q	Generalized Coordinate
$\tilde{q}$	State Variables
Q_{ij}	Generalized Force
S	Laplace Variable
$\tilde{s}$	Reference Area
t	Time
T_i	Feedback Compensation
V	Velocity
x	Spatial Coordinate
y	Spatial Coordinate
z	Spatial Coordinate
α	Angle of Twist
δ_i	Control Displacement
$\bar{\delta}$	Logarithmic Decrement
λ	Eigenvalue
ξ	Damping Factor
ρ	Density
σ	Real Part of Eigenvalue

τ	Time Constant
ω	Frequency
ϕ	Phase Lag

Subscripts, Superscripts and Abbreviations

a	Augmented
C	Control Surface
D	Denominator
D	Divergence
f	Flutter
LE	Leading Edge
N	Numerator
NM	Not Measured
P	Passive
s	Structural
T	Transpose of Matrix
TE	Trailing Edge
-1	Inverse of Matrix

CHAPTER I

INTRODUCTION

Aeroelasticity is defined as the mutual interaction
of the aircraft structural and inertial forces with the
steady and unsteady aerodynamic forces induced by the
flexible vehicle. Aeroelastic phenomena are classified
as either "static" (not time varying), such as
divergence and control surface reversal or "dynamic"
(time varying), such as flutter, dynamic response and
buffeting.   In general, the steady and unsteady
aerodynamic forces produce elastic displacements which
in turn cause the aerodynamic force to change. This
interaction results in one of three conditions following
a disturbance: (1) elastic displacements attaining
stable equilibrium, (2) elastic displacements reaching a
limit cycle condition (time varying problems only), or
(3) elastic displacements resulting in a structural
failure.

Static divergence occurs when the aerodynamic force
resulting from the wing deformation equals the
structural elastic restoring force, causing the wing to
continue to deform until failure.   Flutter is an

1

unstable oscillation of the lifting surface at some characteristic frequency (referred to as the flutter frequency). At flight conditions below the flutter speed of the aircraft, a disturbance to the wing results in a decaying elastic displacement. At the flutter speed, the negative aerodynamic damping overcomes the wing structural damping and results in a sustained harmonic oscillation. At a condition above the flutter speed, the lifting surface generally diverges in an oscillatory sense until a catastrophic structural failure of the wing occurs. In some cases where structural or other nonlinearities are important, a limit cycle oscillation may occur at speeds above the flutter speed with the amplitude of the oscillation dependent upon the speed.

In accordance with military specifications, it is a requirement that an aircraft be designed such that neither flutter nor divergence can occur at speeds lower than 15 percent (margin of safety) above the maximum aircraft flight velocity. When an aircraft carries wing mounted external stores, it is quite possible that aeroelastic instabilities will occur deep within the flight envelope of the clean wing fighter. Traditionally, speed placards (restrictions) are used to obtain the necessary speed margins of safety. These

speed restrictions can severly degrade the flight envelope of a high performance fighter.

Forward Swept Wings

To delay the severe drag effects of compressibility at high subsonic Mach numbers, it is necessary in the design of flight vehicles to decrease the thickness ratio of the airfoil and to increase the sweep angle of the wing. For an aft swept wing, bending deformation tends to reduce the local angle of attack. This unloading of the wing, referred to as wash-out, virtually eliminates the problem of divergence for the aft swept wing. When the wing is swept forward the bending deformation tends to increase the local angle of attack and the aerodynamic loading. This characteristic, commonly referred to as wash-in results in the low static divergence speed of a cantilever forward swept wing.

The forward swept wing has been long recognized as able to provide some improved performance benefits over the aft swept wing, provided the weight needed to solve the potential aeroelastic problems (divergence) can be made minimal. In 1931, Knight and Noyes[1] showed that a forward swept wing encountered stall at higher angles of attack than a similar aft swept wing. Thus, besides reducing drag (sweep angle effect) forward swept wings were found to produce higher lift coefficients than the

aft swept wing of comparable sweep angle. In 1941, an investigation by Jones[2] showed that swept back wings at high angles of attack could at times produce a rolling or pitching instability because of the premature tip stall. Since forward swept wings at high angles of attack stall first at the wing root, they were found not to be susceptible to these rolling or pitching instabilities. A study conducted by Diederick and Budiansky[3] in 1948 addressed the static divergence problems of forward and aft swept metallic wings. The study concluded that to obtain sufficiently high divergence speeds at moderate forward sweep angles, the increase in structural weight required by higher bending stiffness became prohibitive. As a result, interest in a practical application of the forward swept wing reached a minimum.

In the mid 1970's Krone[4] completed a study in which laminated composite materials were used in such a manner that the divergence speed of a cantilever forward swept wing was improved to a desired airspeed with a minimum weight penalty. Since composite fiber materials have higher specific stiffness and strength characteristics than conventional metals and have directional properties, the orientation of the fibers in a particular direction can change the deformation of the wing under aerodynamic loading. Therefore, the

tailoring of advanced composite materials can reduce the wash-in of the forward swept wing and increase the divergence speed. This study spurred additional and renewed interest in the development of forward swept wing technology. Subsequently, the application of composite materials to forward swept wings was evaluated through detailed analytical studies[5,6] and wind tunnel tests.[7-9]

In many of the forward swept wing studies performed prior to 1980, the effect of motion of the entire aircraft as a rigid body was assumed to be negligible. As a result the flutter speed of a cantilever forward swept wing was calculated to be higher than the static divergence speed and was not the most pressing problem. When the rigid body pitch mode was included in the analyses[10,11], a dynamic instability was predicted to occur at a velocity lower than the static divergence speed of the cantilever wing. Wind tunnel tests[12] involving a forward swept wing free in rigid pitch also encounterd the low speed dynamic instability. This instability was termed pitch/bending flutter or body freedom flutter.

This low velocity instability involves coupling of the aircraft short period mode and a wing bending mode. To further describe the phenomenon, Figure 1 illustrates the coupling behavior of the critical modes of various

5

FORWARD SWEPT CONFIGURATION
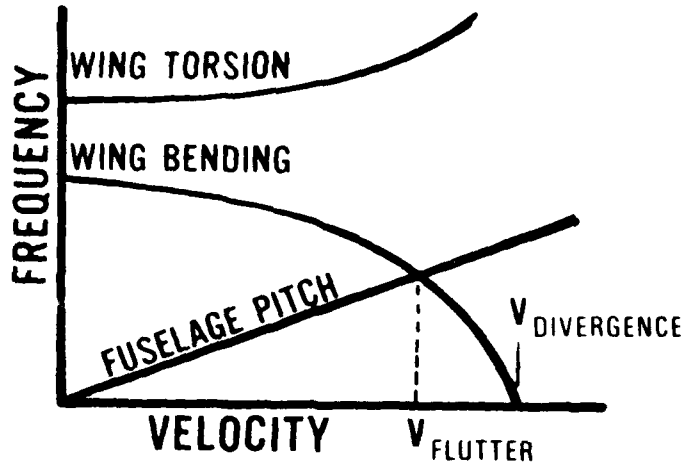
AFT SWEPT CONFIGURATION
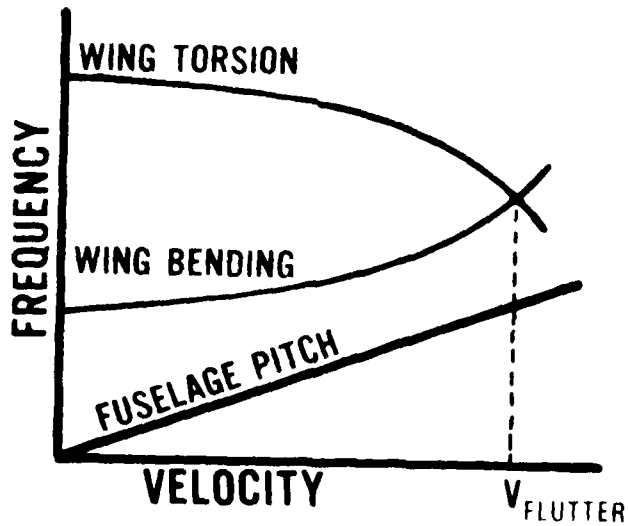
Figure 1   Flutter with Fuselage Pitch Degree of Freedom

6

aircraft configurations. For a cantilever forward swept wing, the bending mode frequency drops with increasing speed until it becomes zero and static divergence occurs. For a forward swept wing aircraft free in pitch, the bending mode frequency still drops but the presence of the short period mode at a lower frequency causes a coalescence of the two modes resulting in a low speed dynamic instability. This instability has been found in rare instances on straight or slightly aft swept wing aircraft in the past.[13,14] For an aft swept wing aircraft classical coupling of the wing torsion mode with a wing bending mode results in bending/torsion flutter whether the model is cantilevered or free in pitch. Although body freedom flutter is calculated to be more critical than divergence of a cantilever forward swept wing for selected aircraft configurations, one should not generalize these findings. It is conceivable that wing divergence may, for peculiar forward swept wing aircraft configurations, be the most critical aeroelastic instability. Therefore, divergence of a cantilever wing should not be disregarded in the development of any new and promising aeroelastic control procedures.

Aeroelastic Control Technology

During the last decade, active control technology has been shown to have promise as a technique of

7

preventing dynamic aeroelastic instabilities in lieu of conventional flutter prevention procedures (adding stiffness or ballast weights). The principles and procedures of applying these concepts are well documented as a result of the significant amount of research performed in the 1970's to develop active flutter suppression technology and in the early 1980's to advance digital flight control and adaptive control principles. Just recently, investigations concerning the use of active controls to delay the onset of divergence[15] and body freedom flutter[10,16] have been completed.

Griffin and Eastep[15] studied the suppression of both static divergence and, separately, bending/torsion flutter using different forward swept wing configurations. For these investigations, a leading edge surface commanded by vertical displacement was found to be best for suppressing static divergence, and a trailing edge surface commanded by acceleration was best for controlling bending/torsion flutter for the configurations studied.

Miller, Wykes and Brosnan[10] were concerned primarily with investigating the body freedom flutter instability associated with the free to pitch and plunge forward swept wing aircraft. They demonstrated by analyses the capability of suppressing the rigid

8

body/wing bending flutter mode, improving flying and ride qualities, and reducing wing gust loads. An active feedback control system with outboard ailerons and an accelerometer located near the control surface was used. Chipman, Zislin and Waters[16] concluded that active controls could prevent or delay the onset of static divergence using only displacement feedback; and that body freedom flutter could be controlled best by using a feedback signal dominated by displacement. The control surface used for these studies was a trailing edge outboard flap.

Technology Needs

Future weapon requirements, restricted by inflationary costs define the need for a multimission fighter. It is speculated that the forward swept wing fighter will evolve in operational deployment similar to what had occurred in the past for aft swept wing fighters. That is, the forward swept wing fighter will be designed for an air superiority primary mission but will be used in off-design missions for air-to-ground sorties. To obtain this multirole capability, the forward swept wing fighter will need to carry external stores conformally on the fuselage and under the wings. However, the adverse mass and inertia distribution on the wings caused by the external stores have traditionally resulted in severe bending/torsion flutter

problems restricting the aircraft to lower speeds and smaller payloads. External stores carried by the forward swept wing fighter will cause the higher frequency bending/torsion flutter mode to drop within the flight envelope of the vehicle or come in close proximity to the aeroelastic instabilities more commonly associated with the forward swept wing. Conventional flutter prevention techniques of ballasting the wing, or stiffening the wing are not suited for solving store flutter problems. Also, the use of speed placards to avoid aeroelastic instabilities can cause severe speed restrictions resulting in a degradation of aircraft performance and survivability.

Active feedback control systems offer significant *promise of* alleviating external store flutter problems in the future. Therefore, the purpose of the present research is to demonstrate by analysis the potential for and feasibility of applying active feedback control systems for preventing, simultaneously: (1) divergence and a high frequency bending/torsion flutter mode (in close proximity) of a cantilever forward swept wing; and (2) the rigid body pitch/wing bending instability and flutter (in close proximity) associated with the wing free in pitch or free in pitch and plunge. The goal is to increase the onset of the lowest instability speed 20 percent above the wing bending/torsion flutter speed of

10

each wing configuration.

The information reported herein describes the forward swept wing model selected for the study, and the analysis techniques and system design approach used. After the design of a control law for each wing condition is obtained, analyses are conducted at off-design conditions to evaluate the performance and sensitivity of each system. The results of these analyses are also presented. Finally, concluding remarks and some recommendations for further study are provided.

11

CHAPTER II

THEORETICAL DEVELOPMENT

The calculation of the response of an airplane in flight caused by some disturbance is generally based on the modal approach where the response is assumed to consist of a superposition of a finite number of normal modes of the unrestrained airplane including both rigid body and elastic structural modes. In reality, there are an infinite number of normal vibration modes of an aircraft structure. Only a limited number of the lower frequency modes are used in the usual divergence and flutter analyses. Also for studies to determine the degree of interaction involving the active system and the aircraft structure, only a few of the lower frequency normal vibration modes are used. Active system coupling with higher frequency modes (greater than 30 Hz) is very remote because of the inherent decrease in the system gain with frequency.

Frequency Domain Flutter Equations

In this section the governing aircraft equations of motion used for classical divergence and flutter analyses are formulated and reviewed. These equations are used during the present research when analytical

12

flutter and divergence predictions are referenced as k-method or P-k method results. These derivations are followed by the development of the governing equations required for applying the root locus techniques of determining aircraft stability.

The aeroelastic equations of motion of a flexible aircraft in the airstream are represented as

$$[M]\{\ddot{q}\} + [C]\{\dot{q}\} + [K]\{q\} = \{F\}, \tag{1}$$

where $[M]$, $[C]$ and $[K]$ are the generalized mass, damping, and stiffness matrices obtained using a set of generalized coordinates $\{q\}$ and several natural vibration mode shapes (NMODES), and $\{F\}$ represents the unsteady aerodynamic forces. For this study, the forces are obtained from the subsonic doublet lattice unsteady aerodynamic theory[17]. These forces are defined to be

$$\{F\} = -\frac{1}{2}\rho V^2 \tilde{s}\ [Q(k)]\{q\} \tag{2}$$

The elements of the generalized aerodynamic force coefficient matrix $[Q]$ are computed from

$$Q_{ij} = \int\int \frac{\Delta P_j}{\frac{1}{2}\rho V^2}\ \frac{h_i}{\tilde{s}}\ dx\ dy,\ i\ and\ j = 1, NMODES \tag{3}$$

The coefficient Q_{ij} represents the force in the ith mode due to pressure from the jth mode and is dependent on the reduced frequency k where

$$k = \frac{b\omega}{V}\ . \tag{4}$$

13

For simple harmonic motion, the generalized coordinates $\{q\}$ take the form

$$\{q\} = \{\bar{q}\}\, e^{i\omega t} \tag{5}$$

where ω is the frequency of oscillation. After substituting Equations (2) and (5) into Equation (1), the aeroelastic equations of motion become

$$\left[-\omega^2[M] + i\omega[C] + [K] + \frac{1}{2}\rho V^2 \bar{s}[Q] \right]\{\bar{q}\} = 0. \tag{6}$$

Replacing the viscous damping matrix $[\omega C]$ by an equivalent diagonal structural damping expression $[g_s K]$, the aeroelastic equations of motion become

$$\left[\omega^2[M] - \frac{1}{2}\rho \bar{s}\, \frac{\omega^2 b^2}{k^2}[Q] \right]\{\bar{q}\} = [R]\{\bar{q}\}. \tag{7}$$

With this equivalent diagonal structural damping representation, an element of the diagonal stiffness matrix $[\bar{K}]$ becomes

$$\bar{K}_{jj} = (1 + i g_{sj})\, K_{jj}$$

or

$$\bar{R}_{jj} = (1 + i g_{s_j})\, \omega_j^2\, M_{jj} \tag{8}$$

where ω_j is the natural frequency of the jth mode, M_{jj} is the jth element of the diagonal mass matrix $[M]$, and g_{sj} represents the structural damping in each of the modes.

14

Since conventional aerodynamic theories are valid for only undamped oscillations, an unknown damping term, g, is introduced into Equation (8) to force simple harmonic motion. As a result, a stiffness element now becomes

$$\hat{K}_{jj} = (1 + ig + ig_{s_j})\, K_{jj}. \tag{9}$$

For small damping values ($gg_{sj} \ll 1$), the stiffness is approximated by

$$\hat{K}_{jj} = (1 + ig)\, \hat{K}_{jj}. \tag{10}$$

With the unknown damping term included, the aeroelastic equations become

$$[R]^{-1}\left[\,[M] - \frac{1}{2}\,\frac{\rho b^2 s}{k^2}\,[Q]\,\right]\{\bar{q}\} = \lambda\{\bar{q}\}. \tag{11}$$

Equation (11) represents an eigenvalue problem with eigenvalues, $\lambda = \dfrac{1 + ig}{\omega^2}$ and eigenvectors, $\{\bar{q}\}$.

One of the most common methods of solving Equation (11) when the aerodynamics depend on reduced frequency, is referred to as the k-method. For each reduced frequency chosen, a set of aerodynamic force coefficients [Q] are calculated and the eigenvalue problem is solved. The damping calculated from the eigenvalue represents the damping that must be added to and taken away from the system to force simple harmonic motion. When the damping is predicted to be zero, a

15

solution is obtained.

For the k-method, the trends of damping versus velocity are not accurate away from a g of zero. If subcritical or supercritical damping trends are necessary in a design, other solution techniques must be considered. One such method uses a transient aerodynamic representation in which simple harmonic motion need not be considered. Another technique which provides more accurate damping trends is called the P-k method.

The P-k method assumes that the generalized coordinates are damped harmonic functions represented as

$$\{q\} = \{\tilde{q}\}e^{\Omega t} \qquad \text{where} \tag{12}$$

$$\Omega = \tau + i\omega = \frac{Vk}{b}(\gamma + i) = \frac{V}{b}P. \tag{13}$$

Again, with the use of the equivalent diagonal structural damping representation, the aeroelastic equations of motion become

$$\left[(\frac{V}{b})^2 p^2 [M] + [\bar{k}] + \frac{1}{2}\rho V^2 \tilde{s}[Q] \right] \{\tilde{q}\} = 0. \tag{14}$$

The characteristic equation is obtained by setting the determinent of the coefficient matrix of Equation (14) equal to zero. For a specific velocity and reduced frequency, the eigenvalue, P, is obtained from the characteristic equation using conventional techniques of matrix polynomial factorization. From the eigenvalues,

16

the frequency, (ω) and damping coefficient (γ) are determined.

For both the k-method and the P-k method, flutter speed is determined when the damping of a mode becomes zero. The static divergence speed is determined when the frequency and damping of a mode become zero simultaneously.

Laplace Domain Flutter Equations

It is quite often important to consider time domain specifications such as damping ratio, overshoot, settling time, etc., in the study of linear systems. By deriving the differential equations of the system and determining the time solutions, the designer can obtain the system's performance characteristics. However, this approach becomes extremely difficult for problems other than simple systems. Also, if the solution of the differential equation does not satisfy the design specifications, it is not easy to determine what variables in the equation need to be changed to obtain the required performance. One of the more classical approaches for evaluating the time related stability characteristics of an aircraft involves the use of the root locus criterion. The root locus criterion allows the designer to predict the performance of a system without actually solving the differential equation of motion. This technique is a graphical method for

17

determining the roots of the characteristic equation
(Laplace transform of the equations of motion).

To develop the problem into a form suitable for
analysis employing the root locus procedure, it is
necessary to start with the flexible aircraft equations
of motion as provided in Equation (1). For zero initial
conditions, the Laplace transform of Equation (1) takes
the form

$$\left[[M]s^2 + [C]s + [K] + \frac{1}{2} \rho V^2 \tilde{s} \ [Q(s)] \right] \{q(s)\} = 0. \tag{15}$$

The characteristic equation is obtained by setting the
determinant of the coefficient matrix in Equation (15)
equal to zero. The roots of the resulting polynomial
may be plotted in the complex plane as the velocity
varies. Such a plot is referred to as a velocity root
locus plot. Determining the roots requires that $[Q(s)]$
be known.

Pade' Approximations to the Unsteady Forces

To obtain the unsteady aerodynamic forces in a
polynomial representation of the Laplace variable for
use with the root locus techniques, a Pade'
approximant[18] of the aerodynamics is considered. A
Pade' approximant was proposed by Vepa[19] as an
aerodynamic force coefficient fitting function. Vepa
recommended that the Pade' approximant for the

18

generalized forces should have a numerator polynomial of order one higher than the denominator polynomial for subsonic flow. In this study, a Pade' approximant with a numerator polynomial of order 3 provides a good approximation to the generalized forces for the low subsonic speed range investigated.

To obtain the Pade' approximants, a least squares fitting scheme is employed. This is accomplished by minimizing a quadratic function J defined as

$$J = (Z - \hat{Z})^T (Z - \hat{Z}) \tag{16}$$

where Z is the calculated value of $Q_{ij}(k)$ and $\hat{Z}$ is the estimated value of Z. For a specific generalized force coefficient and for a set of ι reduced frequencies, an aerodynamic force vector of 2ι terms is formed as,

$$Z = \left\{ \begin{array}{c} \text{Real } (Q_{ij}(K_1)) \\ \vdots \\ \text{Real } (Q_{ij}(K_\iota)) \\ \hline \text{IMAG } (Q_{ij}(K_1)) \\ \vdots \\ \text{IMAG } (Q_{ij}(K_\iota)) \end{array} \right\} \tag{17}$$

The objective is to obtain the aerodynamic force coefficients in the Pade' Polynomial form of

$$Q_{ij}(\bar{S}) = \left(\frac{N_0 + N_1 \bar{S} + N_2 \bar{S}^2 + N_3 \bar{S}^3}{1 + D_1 \bar{S} + D_2 S^2} \right)_{ij} \tag{18}$$

where $\bar{S} = \frac{bS}{V}$. $\tag{19}$

19

The curve fitting is completed along the imaginary axis with respect to k, since here $\bar{S} = ki$. The transformation from k to $\bar{S}$ and finally to S is accomplished later. The calculated value of $Q_{ij}(k)$ for the nth reduced frequency takes the form

$$\hat{Z} = Q_{ij}(k_n) = \left(\frac{N_0 + N_1 k_n i - N_2 k_n^2 - N_3 k_n^3 i}{1 + D_1 k_n i - D_2 k_n^2} \right)_{ij} \qquad (20)$$

Equation (20) is rearranged to appear as

$$Q_{ij}(k_n) = [H_n] \{\hat{x}\}, \qquad (21)$$

where the nth submatrix becomes

$$[H_n] = \begin{bmatrix} 1 & 0 & -k_n^2 & 0 & k_n \text{IMAG} (Q_{ij}(k_n)) & k_n^2 \text{REAL} (Q_{ij}(k_n)) \\ 0 & k_n & 0 & -k_n^3 & -k_n \text{REAL} (Q_{ij}(k_n)) & k_n^2 \text{IMAG} (Q_{ij}(k_n)) \end{bmatrix} \qquad (22)$$

and $\{\hat{x}\}^T = \lfloor N_0 \ N_1 \ N_2 \ N_3 \ D_1 \ D_2 \rfloor$ (23)

Minimizing J by taking it's derivative with respect to $\{\hat{x}\}$, the polynomial coefficients are found from

$$\{\hat{x}\} = [H^T H]^{-1} [H]^T \{z\}. \qquad (24)$$

The coefficients N_i and D_i are obtained in two separate steps. Unique numerator and denominator polynomials are obtained using a least square fitting process for each of the aerodynamic force coefficient elements over the reduced frequency range of interest. To reduce the number of roots associated with the

aerodynamic fitting procedure, all the denominator polynomials are averaged together to obtain one common denominator. During the second step, the least square process is repeated with the denominator polynomials constrained to the averaged values obtained during the previous step.

Using Equations (18) and (19), a typical aerodynamic force coefficient is represented as

$$Q(S)_{ij} = \left(\frac{N_0 + N_1 \frac{b}{V}S + N_2 (\frac{b}{V})^2 S^2 + N_3 (\frac{b}{V})^3 S^3}{1 + \bar{D}_1 \frac{b}{V} S + \bar{D}_2 (\frac{b}{V})^2 S^2} \right)_{ij} \qquad (25)$$

in terms of the Laplace variable S. The generalized force matrix becomes

$$[Q(S)] = \frac{[C_0]V^3 + [C_1]V^2 b\ S + [C_2]Vb^2 S^2 + [C_3]b^3 S^3}{V^3 + \bar{D}_1\ bV^2 S + \bar{D}_2 Vb^2 S^2} \qquad (26)$$

where $[C_0]$, $[C_1]$, $[C_2]$ and $[C_3]$ are matrices with elements N_{0ij}, N_{1ij}, N_{2ij} and N_{3ij} respectively.

Aeroelastic Equations with Active Controls

The aeroelastic equations of motion of a flexible aircraft with control surfaces are described as

$$[M]\{\ddot{h}\} + [C]\{\dot{h}\} + [K]\{h\} + \frac{1}{2}\rho V^2 \bar{S}\ [Q]\{h\} + [M_C]\{\ddot{q}_C\} + \frac{1}{2}\rho V^2 \bar{S}\ [Q_C]\{q_C\} = 0 \qquad (27)$$

where $[M_C]$ and $[Q_C]$ are matrices of order NMODES x M (M equals the number of control surfaces). For i

21

control surfaces,

$$\{q_c\} = \left\{ \begin{array}{c} \delta_1 \\ \delta_2 \\ \vdots \\ \delta_i \end{array} \right\} \qquad (28)$$

The control displacements, δ_i, are defined as

$$\delta_i = T_i(S) \ \lfloor \bar{h}_i \rfloor \ \{q\}. \qquad (29)$$

$T_i(S)$ represents the transfer functions in the Laplace variable in each of the feedback loops (gain, sensor dynamics, actuator dynamics, and the compensation), and $\lfloor h_i \rfloor$ are defined as the modal participation coefficients which relate the degree each of the rigid body or elastic modes participate in the wing motion at a particular location on the structure. For these analyses, sensor and actuator dynamics were neglected. Although the control of divergence and the body freedom flutter instability should be somewhat insensitive to actuator and sensor dynamics because of the low frequencies involved, the control of higher frequency wing flutter will be influenced by the addition of these components. However, previous studies that have included the actuator and sensor characteristics in the analysis have shown that adequate compensation can be easily developed for significantly improving the flutter speeds of advanced vehicles.

Substitution of Equation (29) into Equation (28) and realizing that $T_i(S)$ is a ratio of two polynomials in the Laplace variable S, gives

22

$$\{q_C\} = \begin{bmatrix} \dfrac{T_{1N}}{T_{1D}} & \vdots & 0 \\ \cdots & + & \cdots \\ 0 & \vdots & \dfrac{T_{2N}}{T_{2D}} \end{bmatrix} \begin{bmatrix} \bar{h}_1 \\ \cdots \\ \bar{h}_2 \end{bmatrix} \{q\},\tag{30}$$

and $\quad \{q_C\} = \dfrac{[T][\bar{h}]\{q\}}{T_D}$

where $\quad T = \begin{bmatrix} T_{1N}T_{2D} & \vdots & 0 \\ \cdots & + & \cdots \\ 0 & \vdots & T_{2N}T_{1D} \end{bmatrix}$ $\tag{31}$

and $\quad T_D = T_{1D}T_{2D}.$ $\tag{32}$

By obtaining Pade' approximants for the control surface aerodynamics with the same averaged denominator coefficients as were obtained for the wing, the Laplace transform of Equation (27) with zero initial conditions becomes

$$\Big[[M]s^2 + [C]s + [K] + \tfrac{1}{2}\rho V^2 \tilde{s}\, [Q] +$$
$$([M_C]s^2 + \tfrac{1}{2}\rho V^2 \tilde{s}\, [Q_C]) \dfrac{[T][\bar{h}]}{T_D} \Big]\{q\} = 0 \tag{33}$$

or $T_D \Big[[A_4]s^4 + [A_3]s^3 + [A_2]s^2 + [A_1]s + [A_0] \Big]\{q\} +$
$$\Big[(V^2 + \bar{D}_1 bVs + \bar{D}_2 b^2 s^2)\, s^2 [M_C] + \tfrac{1}{2}\rho \tilde{s}\, ([C_{0C}]V^4 + [C_{1C}]V^3 bs$$
$$+ [C_{2C}]V^2 b^2 s^2 + [C_{3C}]Vb^3 s^3) \Big] [T][\bar{h}]\{q\} = 0 \tag{34}$$

where $[A_i]$, $i = 0,4$ are defined as

23

$$[A_0] = V^2[K] + \frac{1}{2}\rho\tilde{s}V^4 [C_0],$$

$$[A_1] = V^2[C] + \bar{D}_1 bV[K] + \frac{1}{2}\rho\tilde{s} V^3 b [C_1],$$

$$[A_2] = V^2[M] + \bar{D}_1 bV[C] + \bar{D}_2 b^2[K] + \frac{1}{2}\rho\tilde{s} V^2 b^2[C_2], \qquad (35)$$

$$[A_3] = \bar{D}_1 bV [M] + \bar{D}_2 b^2 [C] + \frac{1}{2}\rho\tilde{s} Vb^3 [C_3],$$

and $[A_4] = \bar{D}_2 b^2 [M]$.

With the feedback compensation and sensor types known, Equation (34) can be represented as

$$[F_n]S^n + [F_{n-1}]S^{n-1} + \cdots + [F_1]S + [F_0] = 0. \qquad (36)$$

Solution of Governing Equations

Equation (36) is a polynomial equation with constant matrix coefficients. These coefficients consist of not only the structural, aerodynamic and planform properties of the aircraft, but also velocity and the control system compensation (gain and phase). For these studies, the velocity and gain can be varied independently to determine velocity and gain root locus plots. For all control system gains set to zero, Equation (36) reduces to a fourth order polynomial with the coefficient matrices defined in Equation (35). An analysis for these conditions will result in the passive (unaugmented) solution of the equations of motion. To obtain the roots of Equation (36), the procedure is to transform the equation into an eigenvalue problem. This is accomplished by letting

$$\dot{\tilde{q}} = S\tilde{q}$$

$$\tilde{q}_1 = \tilde{q}$$

$$\tilde{q}_2 = \dot{\tilde{q}}_1$$

$$\tilde{q}_3 = \dot{\tilde{q}}_2 = \ddot{\tilde{q}}_1$$

(37)

and so on.

Multiplying Equation (36) by $\tilde{q}$ and using Equations (37), the governing equations described in state space form become

$$\dot{\tilde{q}}_1 = \tilde{q}_2$$

$$\dot{\tilde{q}}_2 = \tilde{q}_3$$

$$\dot{\tilde{q}}_3 = \tilde{q}_4$$

(38)

$$. \quad . \quad . \quad . \quad .$$
$$. \quad . \quad . \quad . \quad .$$

$$\dot{\tilde{q}}_n = -F_n^{-1} F_0 \tilde{q}_1 - F_n^{-1} F_1 \tilde{q}_2 - F_n^{-1} F_2 \tilde{q}_3 - \cdot \cdot \cdot - F_n^{-1} F_{n-1} \tilde{q}_n$$

or $\{\dot{\tilde{q}}\} = [A]\{\tilde{q}\}$

(39)

where

$$A = \begin{bmatrix} 0 & I & 0 & . & 0 \\ 0 & 0 & I & \vdots & 0 \\ \vdots & \vdots & \vdots & \vdots & \vdots \\ 0 & 0 & 0 & \vdots & I \\ -F_n^{-1}F_0 & -F_n^{-1}F_1 & -F_n^{-1}F_2 & . & -F_n^{-1}F_{n-1} \end{bmatrix}$$

and $[I]$ is the identity matrix. With $\dot{\tilde{q}} = S\tilde{q}$, Equation (39) becomes

$$S[I]\{\tilde{q}\} = [A]\{\tilde{q}\}$$

or $([A] - S[I])\{\tilde{q}\} = 0$

(40)

25

which is recognized as the standard eigenvalue problem.

To be stable, each root of the characteristic equation must lie in the left half of the complex plane. Roots which lie on the imaginary axis of the complex plane are commonly referred to as being neutrally stable. Since the zero airspeed structural damping is assumed to be zero for the elastic modes used in the analysis, the roots associated with these modes originate from the imaginary axis at their respective natural frequencies.

CHAPTER III

CONFIGURATION DEFINITION

The primary forward swept wing aeroelastic characteristics required for this investigation include a static divergence instability speed in close proximity to the higher frequency bending/torsion flutter speed typical to what will occur if a critical external store configuration is carried. With these properties it will be necessary to develop a system with the capability of suppressing two aeroelastic instabilities simultaneously to obtain a reasonable improvement in airspeed. Also, the interactions of several feedback loops operating independently to control the behavior of various elastic modes is of interest. To acquire these characteristics, the configuration and properties of a wind tunnel model previously tested to investigate divergence[7] and body freedom flutter[12] are selected as the basis for this program. This approach also offers the advantage of possibly testing the model in a modified form at some future time to verify the findings of this analytical investigation.

Since bending/torsion flutter speeds increase significantly with forward sweep angles, a configuration with low forward sweep will serve as a baseline for

obtaining the characteristics desired for this study. As a result, the forward swept wing with the aluminum substructure is selected. This model consists of an aluminum plate that provides the load carrying capability of the wing and airfoil shaped polyurethane foam sleeve sections which surround the plate. The wing can be swept forward at several incremental angles.

After divergence testing[7], the wind tunnel model was modified by including a fuselage bar that was free in rigid pitch. The wing could then be positioned at different locations near the aft end of the fuselage bar to investigate the effects of static margin. The pitch axis of the fuselage bar was always at the system center of gravity, and the wing was always mounted aft of this point to provide weathercock stability.

For this study the reference axis is swept forward -15 degrees; this angle represents a leading edge sweep angle of about -9 degrees. Figure 2 presents a schematic of the wind tunnel model showing key details, dimensions and the relative sizes of the components.

Basic Model Calculations

A finite element[20] representation of the wind tunnel model is developed to perform vibration and conventional flutter analyses[21] for correlation with ground vibration[22] and wind tunnel test data.[7,12].

40.00

16.96

7.5

1.30

PITCH AXIS

15°

REFERENCE AXIS

15% CHORD

65% CHORD

32.16

STRUCTURAL PLATE
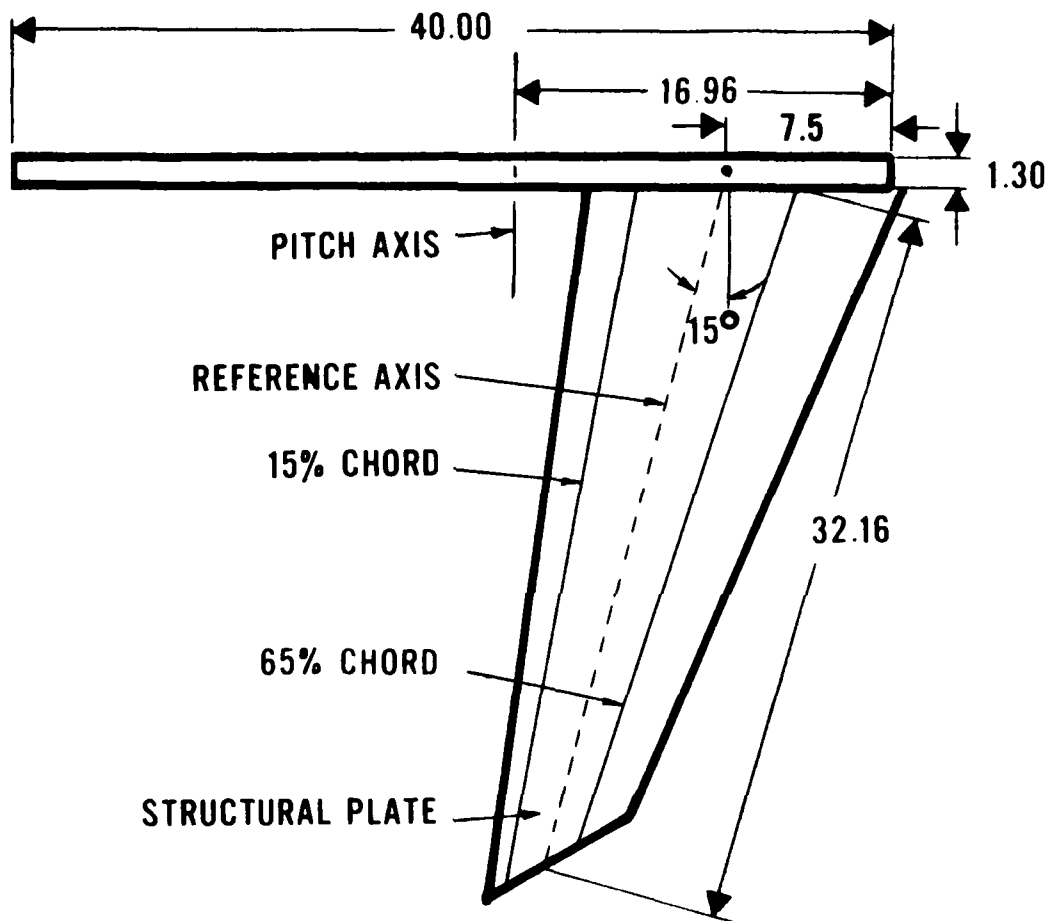
ALL DIMENSIONS IN INCHES

Figure 2 Planform of Forward Swept Wing Model

These analyses also assist in determining the modifications needed to the wind tunnel model to obtain the desired aeroelastic characteristics.

All sectional masses and stiffnesses used in the analysis were experimentally determined[7] to minimize the error in correlation with test data. For all cantilever analyses, the fuselage bar is restrained in such a manner that no motion is permitted along the bar or wing root. When the rigid body pitch mode is included in the analysis, the fuselage bar is permitted to pitch about the center of mass of the system. The modes of interest for this study include the first two bending modes and the first torsion mode. Higher frequency modes are eliminated from the analysis because later flutter analyses show that they have essentially no effect on the instabilities of interest (see Table A-5 in Appendix A).

A vibration analysis using beam elements and only the plate masses and stiffnesses (no aerodynamic sleeves) is initially conducted. The analysis is performed with the plate cantilevered and with the fuselage free to pitch. Frequencies and mode shapes are also calculated with the sleeve masses and some additional stiffness included in the analysis. Although the sleeves are discrete sections separated by foam rubber, stiffness tests had shown a slight increase in

the model bending and torsional stiffnesses when the
sleeves were attached to the plate. The calculated
frequencies for both the plate and wing model are
provided in Table 1 along with experimental results[22]
for comparison. The calculated cantilever results
agree very well with the test data. The largest error
encountered is obtained in the prediction of the wing
2nd bending frequency which is found to be about one
percent lower. There are some larger differences
between the calculated and the test results when the
rigid body pitch degree of freedom is added. The
largest error occurs in the first mode where the
difference between the calculated and experimental
frequency is about six percent. Appendix A provides
additional details concerning the finite element
representation of the wind tunnel model and also
includes the mode shapes for the first three modes of
the wind tunnel model.

All flutter and divergence analyses are conducted
using classical k-methods[21] and a subsonic doublet
lattice unsteady aerodynamic theory[17]. The P-k method
is considered during the study, but aerodynamic
interpolation problems attributed to the body freedom
flutter condition result in poor predictions. More
details on these problems are provided in Appendix B.
The aerodynamic paneling arrangement employed for the

Table 1 Comparisons of Calculated Vibration Frequencies, and Divergence and Flutter Characteristics with Experiment

| CONFIGURATION | VIBRATION | | | | | | DIV/FLUTTER CHARACTERISTICS | | | |
| | 1st BENDING | | 2nd BENDING | | 1st TORSION | | CALCULATED | | EXPERIMENT | |
	CALC	EXP	CALC	EXP	CALC	EXP	V(ft/sec)	ω(Hz)	V(ft/sec)	ω(Hz)
CANTILEVER PLATE	4.3	4.3	22.3	22.4	58.1	58.1	-	-	-	-
FREE PLATE	4.2	4.3	21.6	22.2	56.1	56.3	-	-	-	-
CANTILEVER WING	3.2	3.2	16.2	16.0	36.7	36.7	119 / 236	0 / 21.8	128 / NM	0 / NM
FREE WING	3.1	3.3	15.7	16.3	35.7	37.7	90 / 227	1.4 / 20.8	86 / NM	2.0 / NM
MOD. CANT WING	2.4	-	12.6	-	23.6	-	119 / 155	0 / 16.9	- / -	- / -
MOD. FREE WING	2.3	-	12.5	-	23.1	-	53 / 156	1.2 / 16.0	- / -	- / -

flutter analysis is shown in Figure 3. This paneling consists of a fuselage with five interference panels (not shown) and a slender body, and a wing with six aerodynamic panels subdivided into 104 boxes. Two of the outboard panels represent typical leading edge and trailing edge control surfaces that are investigated for use in the control system analyses. These surfaces are positioned near the wing 3/4 span and have hinge lines parallel to the respective wing edges.

Comparison of wind tunnel divergence and flutter instability characteristics with the analytical predictions are also found in Table 1. For the cantilever model, the divergence speed is predicted to occur at 119 ft/sec while the instability is estimated from test data[7] to occur at 128 ft/sec. This shows the analysis to be about 8 percent conservative. When the model is free in pitch, the body freedom instability is predicted to occur at 90 ft/sec at 1.4 Hz. This is slightly higher than found during the wind tunnel test[12] (86 ft/sec) making the analysis about 4 percent unconservative. For both boundary conditions the higher frequency bending/torsion flutter mode is predicted to be significantly higher than the low speed instabilities.

To accomplish the objectives of this study, it is desirable to obtain a bending/torsion flutter speed

33
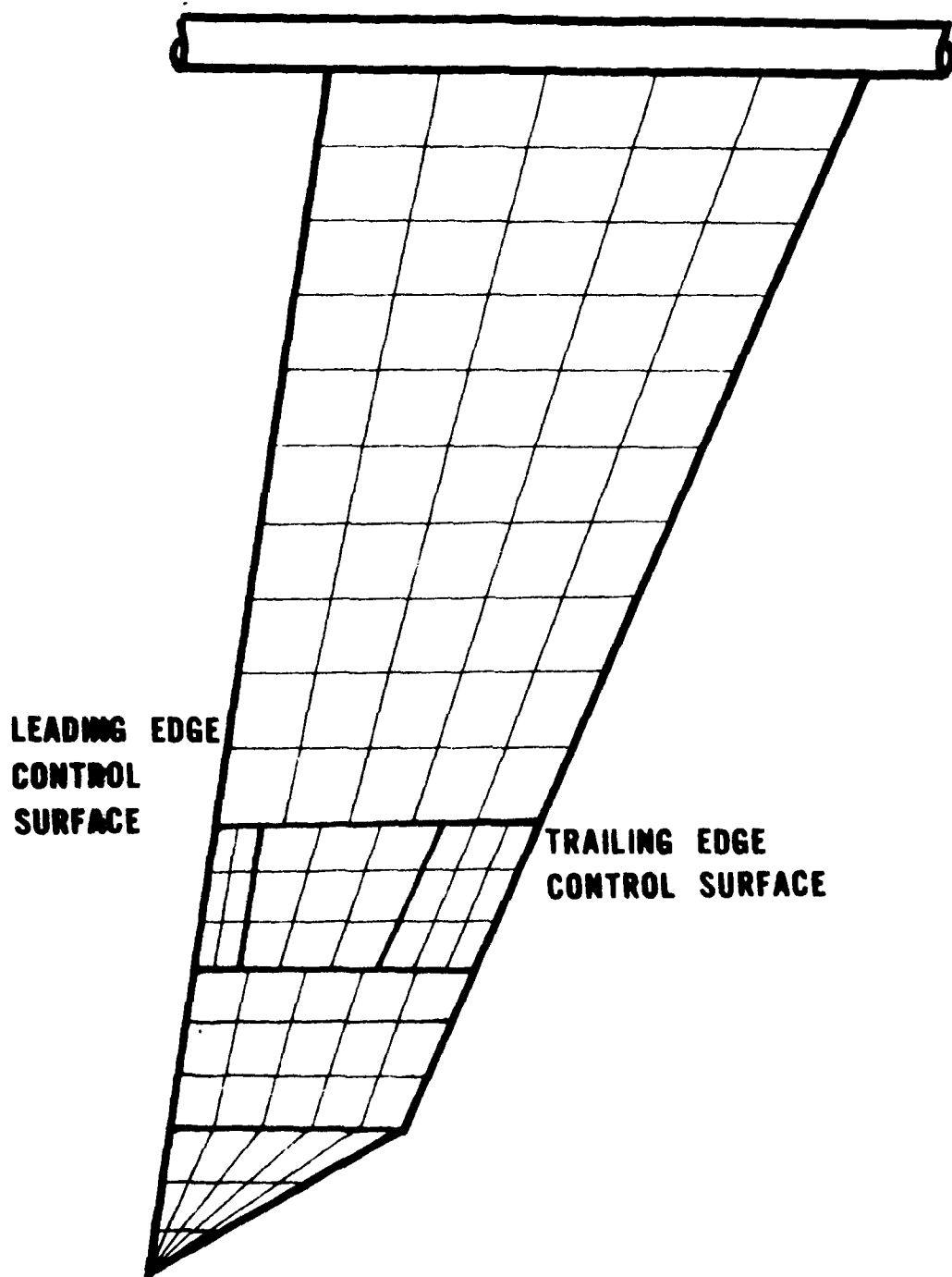
Figure 3 Aerodynamic Panel Representation of Wing with Leading and
Trailing Fdge Control Surfaces

about thirty to forty percent above divergence. These characteristics will more realistically allow an investigation of the interaction of multiple systems controlling several rigid and elastic modes. The changes necessary to the wind tunnel model and the final vibration and flutter analysis results are discussed next.

Modified Model Calculations

To obtain the desired divergence and flutter characteristics, one pound of weight is distributed along the trailing edge of the wing in the outboard six sections. Table 1 presents the calculated vibration frequencies for the first three elastic modes, and the predicted divergence and flutter results for the modified wing configuration (cantilevered and model free in pitch). Mode shapes for the first three elastic modes of the modified model cantilevered, free in pitch and free in pitch and plunge are presented in Figures 4, 5, and 6 respectively.

As expected, the weights have no effect on the divergence speed of the cantilever wing. However, the weights do have a significant effect on the body freedom instability and on the higher frequency flutter mode. The decrease in the body freedom instability speed is primarily attributed to the drop in the 1st wing bending frequency that results from the new wing mass

35

FREQUENCY, HZ
——————— 1B   2.4 **MODE** #1
- - - - - 2B   12.6 **MODE** #2
—··— 1T   23.6 **MODE** #3
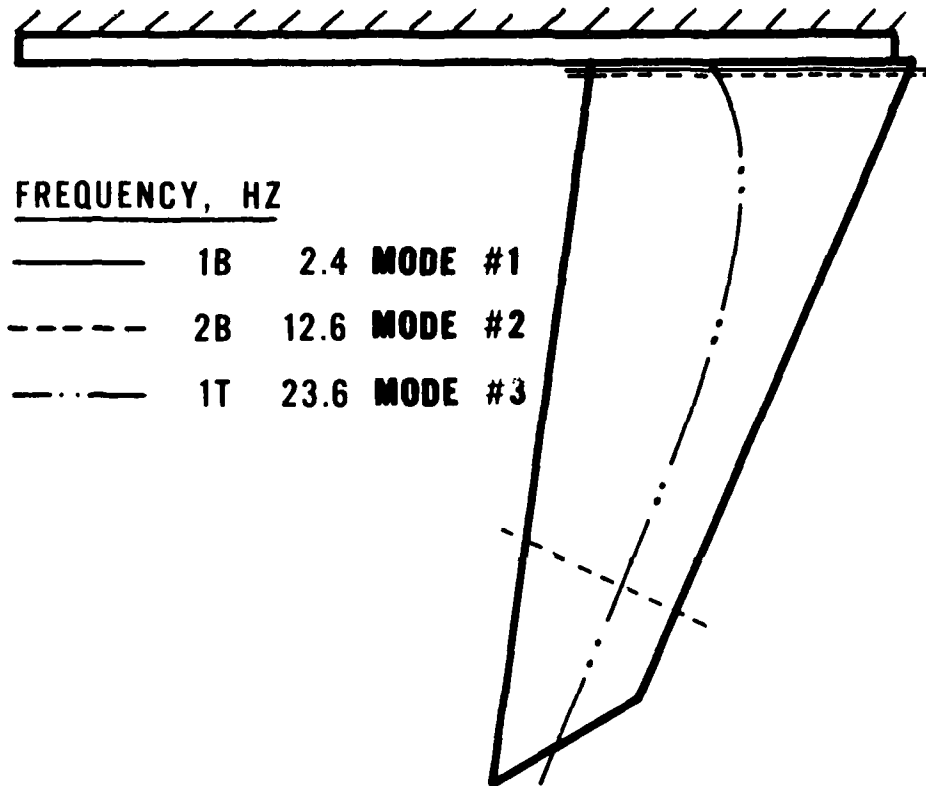
Figure 4   Calculated Frequencies and Node Lines of Modified
Cantilever Model

36

FREQUENCY, HZ

————	1B	2.3	**MODE**	**#2**
——— - --	2B	12.5	**MODE**	**#3**
—— ·· ——	1T	23.1	**MODE**	**#4**

MODE #1 - RIGID BODY PITCH
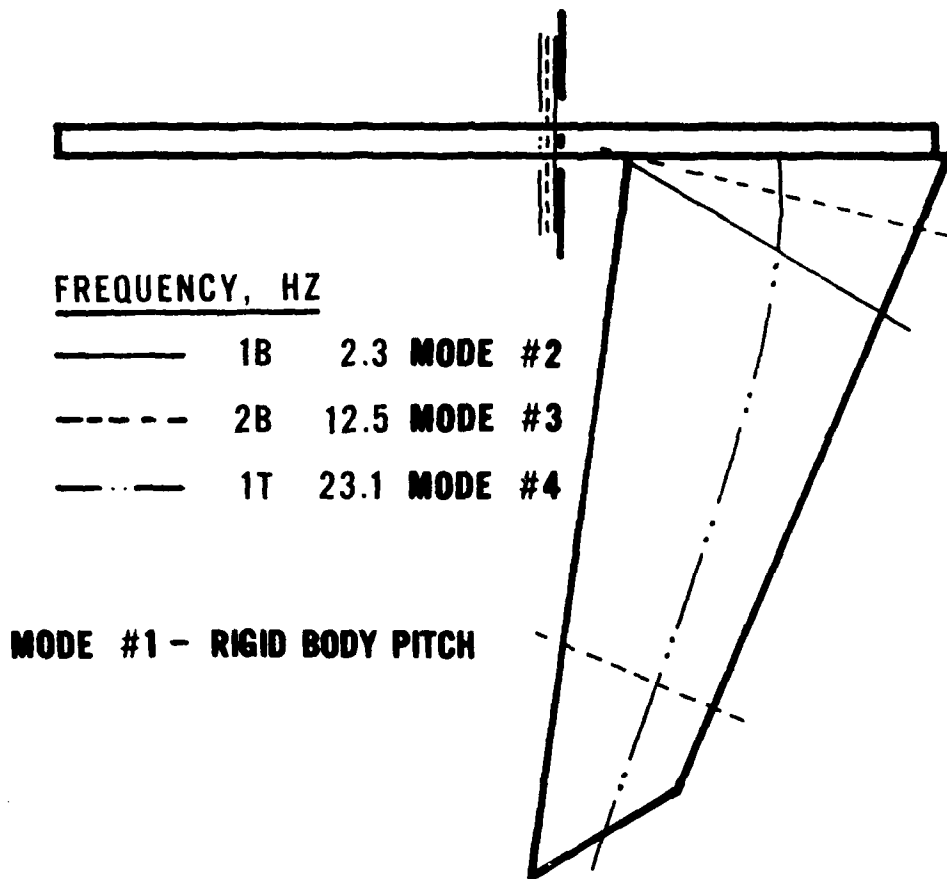
Figure 5 Calculated Frequencies and Node Lines of Modified
Model Free in Pitch

FREQUENCY, HZ

———— 1B 2.6 **MODE #3**

— — — 2B 13.1 **MODE #4**

— ·· — 1T 23.1 **MODE #5**

MODE #1 - RIGID BODY PLUNGE

MODE #2 - RIGID BODY PITCH
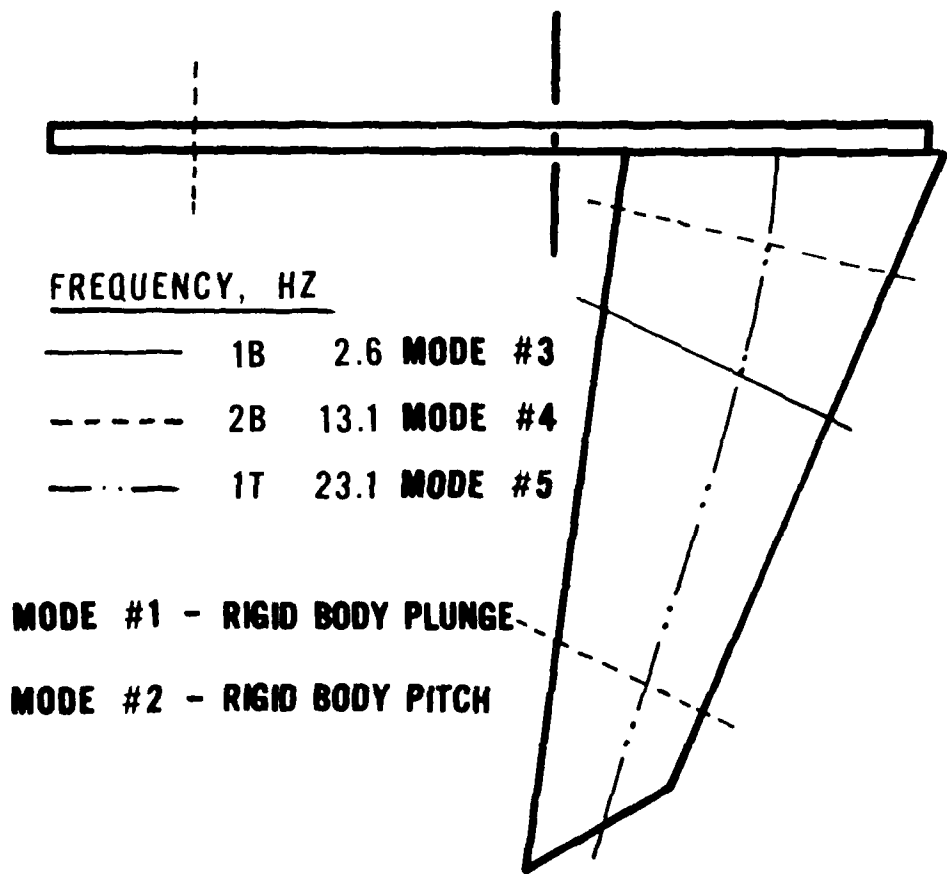
Figure 6 Calculated Frequencies and Node Lines of Modified
Model Free in Pitch and Plunge

distribution. The lower wing bending mode frequency produces an earlier coalescence with the aircraft short period mode resulting in the low speed instability. Also, the additional trailing edge weights cause a significant rise in the wing pitch inertia resulting in the drop in the wing torsion frequency. By comparing the natural frequencies of the various modes for the basic and modified wings (Table 1), the frequency separation between the wing 2nd bending mode and the torsion mode is much closer for the modified wing. This causes the two higher frequency wing modes to coalesce earlier (at a lower speed) resulting in the significant drop in flutter frequency and speed. Mass coupling also contributes to the lower flutter speeds for both modes of instability. Figures A-6 and A-7 in Appendix A provide velocity versus damping and velocity versus frequency plots for the cantilever and free-to-pitch conditions showing the differences in behavior between the basic and modified models.

The modification in the mass of the model results in a bending/torsion flutter speed that is 36 percent above the divergence speed of the cantilever wing. The next section describes the procedures used to design an active feedback system capable of obtaining an instability-free flight envelope up to 20 percent above the bending/torsion flutter speed of the modified model.

CHAPTER IV

ACTIVE SYSTEM DESIGN

The design approach used in the development of the feedback compensation of the system is to obtain gain loci for several sensor types and locations with different control surface inputs at an airspeed 20 percent above the bending/torsion flutter speed. This is accomplished for each of the model boundary conditions (cantilevered, the model free in pitch, and the model free in pitch and plunge). These data provide information needed to determine which of the sensor/control surface combinations result in the best suppression capability for preventing the aeroelastic instabilities of each wing configuration. The various active system logics that provide model aeroelastic stability at the design airspeed are then evaluated at off-design conditions to assure stability over the entire velocity range of interest.

The results of these studies indicate that a leading edge surface commanded by displacement of the wing resulting from only the elastic modes provides a reasonable control system design for preventing divergence of the cantilever wing or the body freedom flutter instability associated with the free model.

40

Displacement at the wing sensor resulting from rigid model pitch and plunge are subtracted from the feedback signal to obtain only a response due to the elastic modes. The displacement sensor is positioned near the intersection of the wing 2nd bending node line and the wing 1st torsion node line. This location provides the best position for feeding back the bending motion of the 1st elastic mode (critical mode for divergence or body freedom flutter) with minimum inputs from the other important elastic modes.

Displacement feedback is a difficult state to measure directly; however, integration of an acceleration signal can provide the needed response. This technique of obtaining a displacement feedback results in significant changes in gain (20db per frequency decade per integration) and phase characteristics (90 phase lag per integration). These changes will undoubtedly need to be accounted for in the final control law design if the double integration technique is used. Integration also offers the advantage of acting as a low pass filter and can be used to eliminate high frequency non-flutter responses (control system induced structural instabilities).

The gain loci analyses also indicate that a trailing edge system commanded by angular acceleration

41

of the wing tip perpendicular to the elastic axis provides an acceptable input for controlling the bending/torsion flutter mode. Based on mode shape data, the bending modes relative to the elastic axis have very little twist. Feeding back wing tip angular acceleration assures maximum input from the torsion mode (maximum twist at the tip) with minimum response from the bending modes.

The sensors used for measuring rigid pitch (angle of attack) and plunge (vertical translation) are located at the model center of gravity on the fuselage bar (pitch axis). For the analyses performed, the best overall suppression capability consists of the leading edge and trailing edge control surfaces positioned in the same streamwise location on the wing at about 75 percent span.

Cantilever Wing

The reduced frequency dependent unsteady aerodynamic force coefficients are represented in the Laplace domain using Pade' approximants. As described earlier, these functions consist of a ratio of two polynomials; the numerator is a 3rd order polynomial, and the denominator, a 2nd order (two lag terms). This combination is found to provide a good fit of the force coefficients over the velocity and frequency ranges of interest. Instead of presenting many tables to

42

illustrate comparisons of the unsteady forces calculated from the doublet lattice and those obtained after fitting the doublet lattice aerodynamics with Pade' polynomials, V-g and V-ω plots are presented. This provides an evaluation of the gross overall fit of the aerodynamic forces. Figure 7 presents the V-g and V-ω plots for the cantilever wing found using the doublet lattice areodynamics (k-flutter method), and using the root locus procedures which employ the Pade' polynomials. Only the first three elastic modes are presented. Correlation between the solid symbols (k-method) and the solid lines (root locus) is very good particularly relative to the frequency plot. The differences in damping values in the 1st bending mode are attributed to the static divergence characteristics as observed on a root locus. Since correlation of the damping and frequency data is satisfactory, it is concluded that the Pade' polynomials provide an accurate fit of the unsteady aerodynamic forces for the cantilever wing over the reduced frequency range of interest.

Figure 8 presents a velocity root locus plot for the cantilever wing with all feedback gains set to zero (passive solution). The passive divergence speed (V_{DP}) is predicted to occur at 115 ft/sec and the passive bending/torsion flutter speed (V_{f_p}) is predicted to
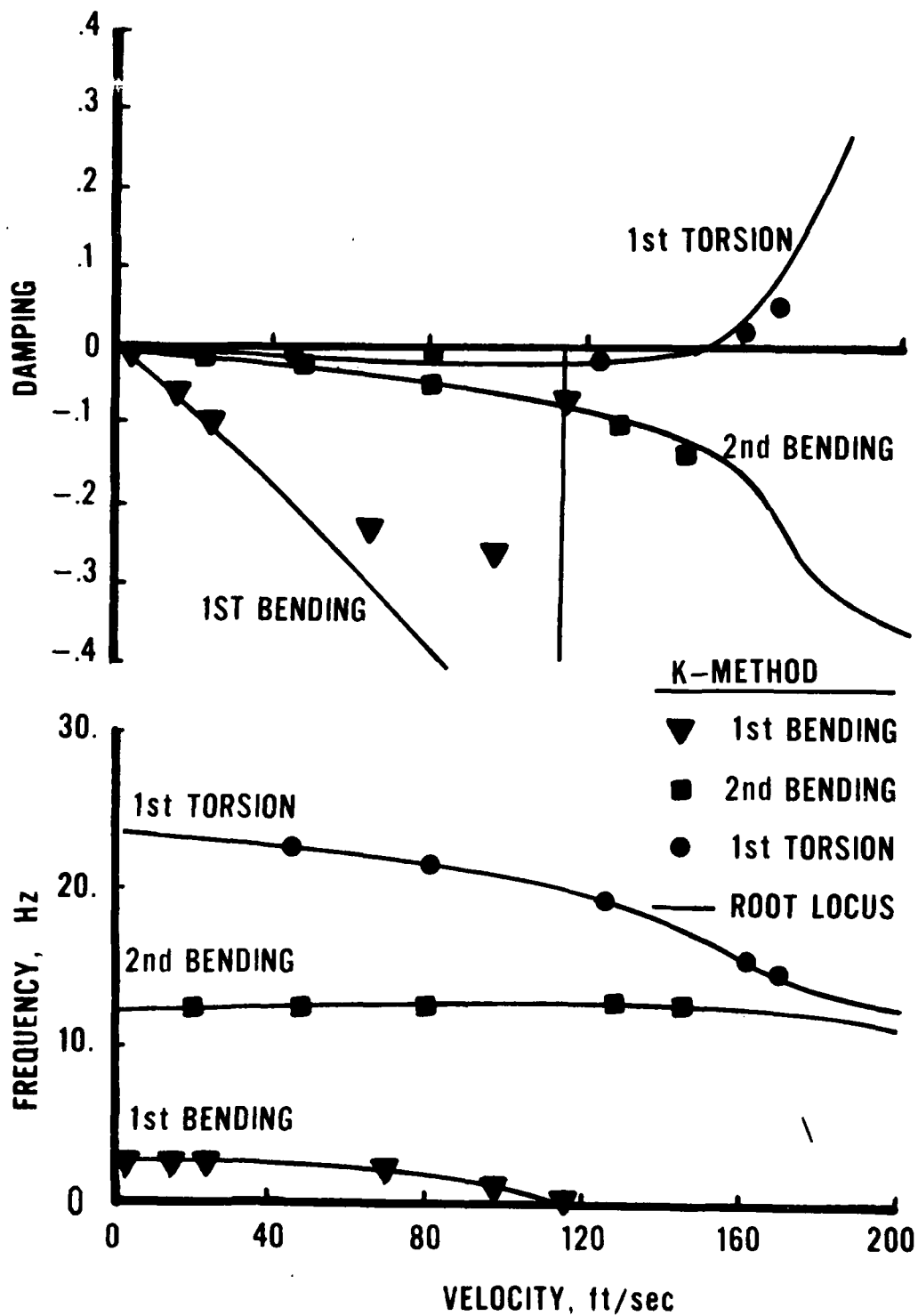
Figure 7   Comparison of V-g and V-ω Plots Using k-Method and Root
Locus, Cantilever Wing (Passive Results)

44
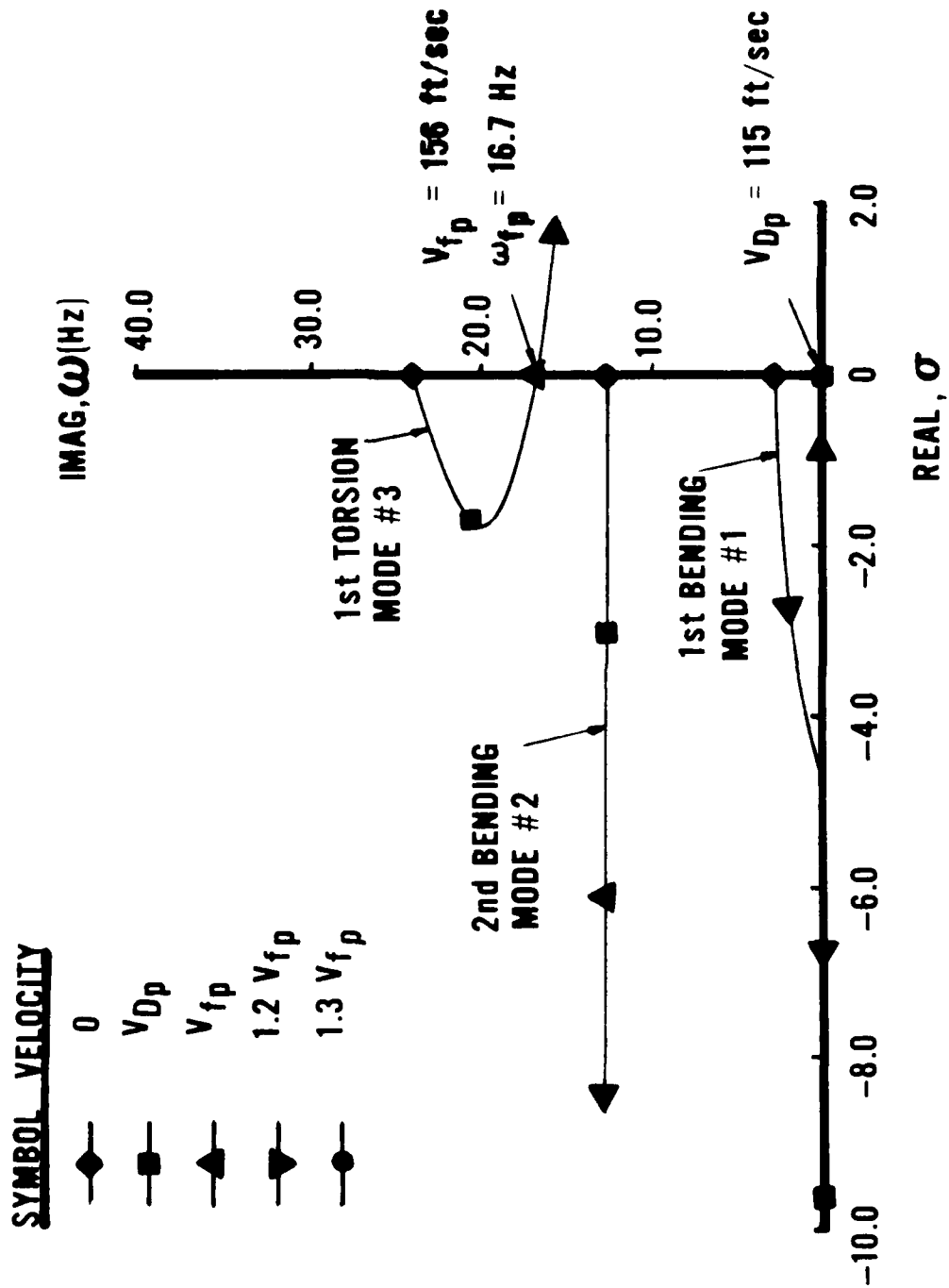
Figure 8 Root Locus Plot for the Cantilever Wing, Passive Solution

45

occur at 156 ft/sec at a passive flutter frequency (ω_{fp}) of 16.7 Hz using Pade' polynomial fits of the aerodynamic force coefficients. Classical flutter methods predict a divergence speed of 119 ft/sec and a bending/torsion flutter speed of 155 ft/sec at 16.9 Hz (see Table A-5 in Appendix A for the k-method results). On a root locus plot, static divergence occurs when the roots associated with an elastic mode move to the negative real axis (frequency dropping to zero) with increasing airspeed and divide into two real roots with one of the roots passing through the origin. When the root reaches the origin, the wing has statically diverged. The 1st bending mode in Figure 8 illustrates these characteristics. Flutter occurs when two modes (normally a bending and a torsion mode) coalesce causing a coupled neutrally stable oscillation. The 1st torsion mode and the 2nd bending mode shown in Figure 8 illustrate these coalescing characteristics.

Figures 9 through 13 present wing displacement and twist gain loci of the cantilever wing resulting from either trailing edge or leading edge control surface excitations at a design speed 20 percent above the passive bending/torsion flutter speed (1.2 V_{fp}). The poles of the system represent the location of the roots of the elastic modes with the gains set to zero at the design velocity. At this speed, two of the poles are
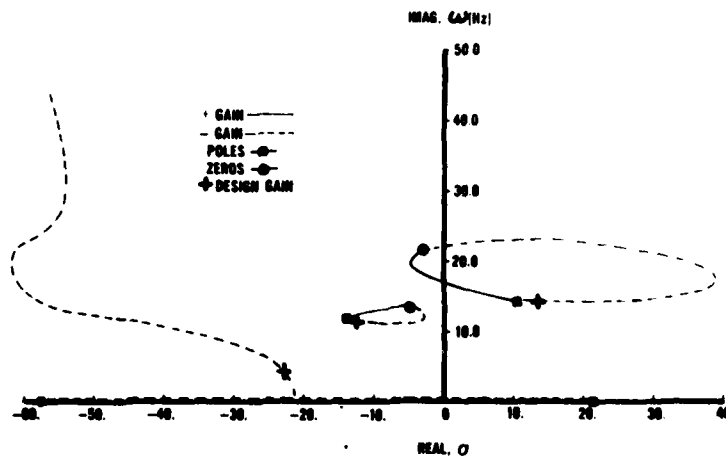
46

Figure 9   h Versus δ_{TE} Gain, Cantilever Wing, $V = 1.2\ V_{f_p}$

Figure 10   h Versus δ_{LE} Gain, Cantilever Wing, $V = 1.2\ V_{f_p}$

47
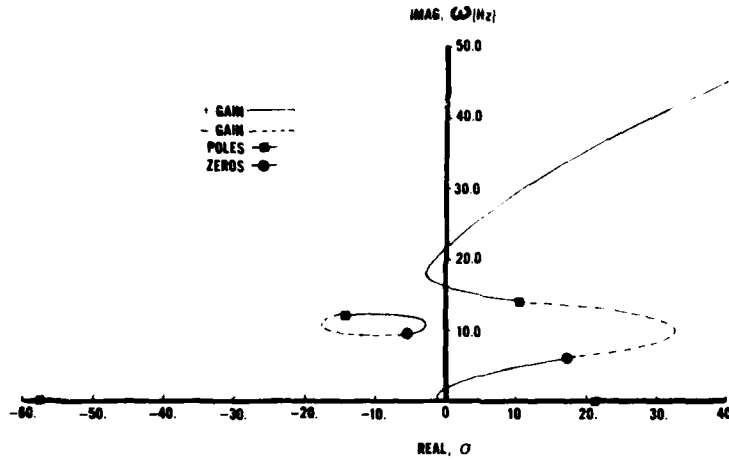
Figure 11 α Versus δ_{TE} Gain, Cantilever Wing, $V = 1.2\ V_{f_p}$

Figure 12 α Versus δ_{LE} Gain, Cantilever Wing, $V = 1.2\ V_{f_p}$

48

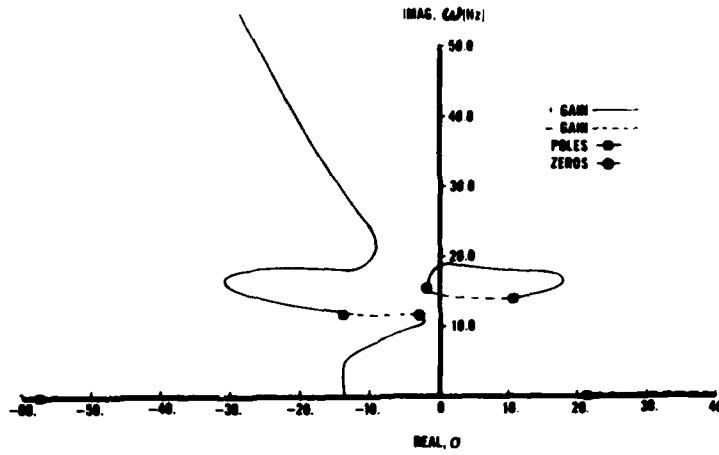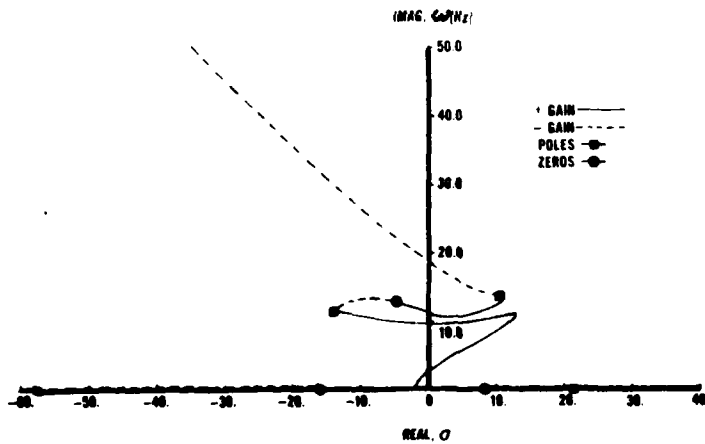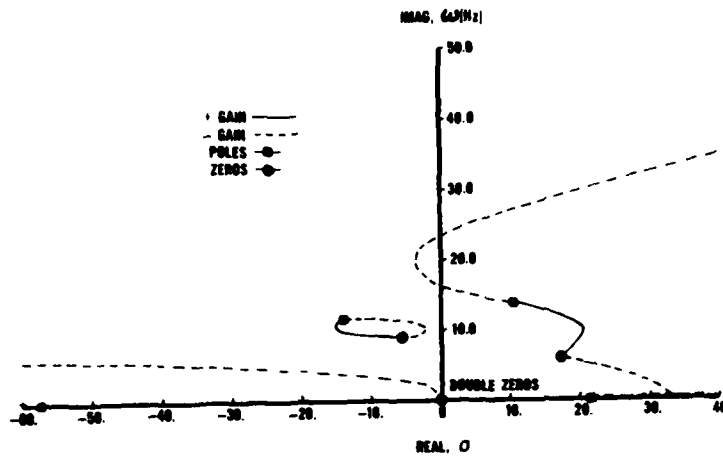Figure 13 α Versus δ_{TE} Gain, Cantilever Wing, V = 1.2 V_{f_p}
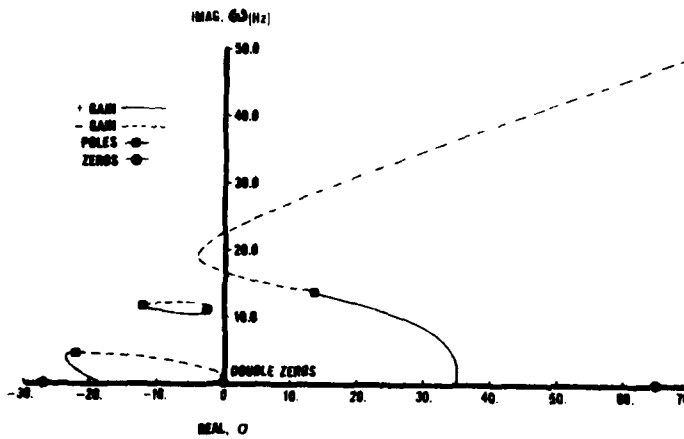
Figure 14 α Versus δ_{TE} Gain with K_{LE} = -5.20, Cantilever Wing, V = 1.2 V_{f_p}

49

unstable. The first bending mode appears as two roots on the real axis, one of which is in the right half plane (static divergence). The other unstable mode is the 1st torsion mode which is shown as one of the roots of a complex pair at about 13.9 Hz. The 2nd bending mode located at about 11.9 Hz is stable at this airspeed. Since the roots represent the passive solution of the equations of motion at the design airspeed, the location of the poles are identical for Figures 9 through 13. The solid circles on the charts represent the zeros of the control law (location of the root at infinite gain). The solid lines represent the path taken by the roots when gain is increased from zero to positive infinity. Dash lines represent the path taken by the roots when the gain is decreased from zero to negative infinity.

Figure 9 provides the root locus for the transfer function h/δ_{TE}. The plot shows that positive gain will cause both of the roots associated with the unstable elastic modes to move to the left half plane becoming stable at this airspeed. However, a velocity root locus using several values of positive gain, equal to or higher than that required to stabilize the two modes at 1.2 V_{fp}, shows low speed instabilities in both the 2nd bending and 1st torsion modes. Negative gain, although beneficial for controlling torsion, drives the unstable

real root deeper into the right half plane. Therefore, the trailing edge surface does not appear to be a suitable surface for preventing divergence much less both instabilities simultaneously. Figure 10 provides the root locus for a transfer function that relates displacement to leading edge excitation (h/δ_{LE}). This plot shows that negative gain brings the unstable real root back to the left side quite rapidly but high negative gains are required to stabilize the 1st torsion mode. It is found, however, that the high negative gains tend to destabilize other modes at off-design conditions similar to what was found for the transfer function h/δ_{TE}. For this case high gains destabilize the 2nd bending mode at velocities lower than the design velocity. For this control surface/sensor combination, only negative gain requires further consideration as a potential feedback signal for controlling divergence. This is a result of having a real pole in the right half plane causing the model to be unstable for all positive gains.

Figures 11 and 12 present wing twist transfer functions resulting from trailing edge and leading edge excitations, respectively. With trailing edge excitation, positive gain in a small range can stabilize both aeroelastic instabilities of the model at the design airspeed. With increasing positive gains the

51

real roots meet in the left hand plane forming a stable complex pair of roots. For higher gains, the complex pair migrate back into the right half plane, becoming a dynamic instability. For gains in this small positive range, the model is again predicted to be unstable at lower airspeeds in the 2nd bending mode. With leading edge excitation (Figure 12) neither positive nor negative gain can stabilize both of the unstable modes at the design airspeed because of the pole/zero combination on the real axis in the right half plane.

As a result of the data base established for active flutter suppression, angular acceleration is considered as a possible signal for controlling the bending/torsion flutter mode. Figure 13 provides the gain locus of angular acceleration versus trailing edge excitation. These data show that negative feedback is best for stabilizing the 1st torsion mode (flutter mode) but does little to stabilize the divergence mode on the real axis.

After detailed evaluation of the previous information and other combinations of sensors and control surfaces, and taking into account the high gain effects on other modes at lower velocities when a single surface is used, it is concluded that a two-surface system is required. The design logic is to use the leading edge surface primarily for controlling

52

divergence using the displacement feedback, and to use the trailing edge surface with angular acceleration feedback to control the higher frequency bending/torsion flutter mode. The frequency separation of the two modes of instability of this configuration add to this conclusion since each control surface and associated compensation can be designed for a different frequency range.

Referring to Figure 10, negative gain on the displacement signal to the leading edge surface is selected such that the 1st bending mode is stable at 1.2 V_{fp} and has gain margins of at least $\pm$ 6db at V_{fp}. The gain is found to be -5.2 deg/in. This gain value is marked as the design gain on the loci of Figure 10.

With the leading edge loop closed, the second loop using the trailing edge control surface and angular acceleration feedback is designed to stabilize the torsion mode of 1.2 V_{fp} with gain margins of at least $\pm$ 6db at V_{fp}. Figure 14 provides a gain root locus for angular acceleration feedback and trailing edge excitation with the leading edge loop closed. This plot shows that two of the poles of the system, the 1st bending and 2nd bending, are stable at 1.2 V_{fp} as expected since the leading edge loop is closed. The torsion mode, however, still remains unstable for zero gain on the trailing edge system. Only negative

feedback in a small range is successful in stabilizing the torsion mode. A trailing edge gain of $-.025$ deg/deg/sec^2 is required to stabilize the torsion mode at 1.2 V_{fp} and to provide the desired gain margins at V_{fp}.

To obtain maximum phase margins, a phase lag network of the form $\frac{1 - \tau S}{1 + \tau S}$ is included in the feedback

compensation of the trailing edge system. This type of network has been used extensively in operational analog simulations to verify control system phase margins. It is ideal for this use because large phase angles are possible with no gain changes. Such an element can easily be obtained in terms of operational amplifiers and potentiometers when hardware is required. Other techniques of including phase angle changes on the feedback system have also been used quite successfully in previous active flutter suppression analyses and tests. For this control logic the phase lag function $\frac{1 - .04223S}{1 + .04223S}$ provides the best phase characteristics for the cantilever wing. This system provides 155 degrees of phase lag at a reference frequency of 17 Hz.

Figure 15 shows the gain loci with the leading edge loop closed and the phase lag network included in the trailing edge loop compensation. The addition of the

54
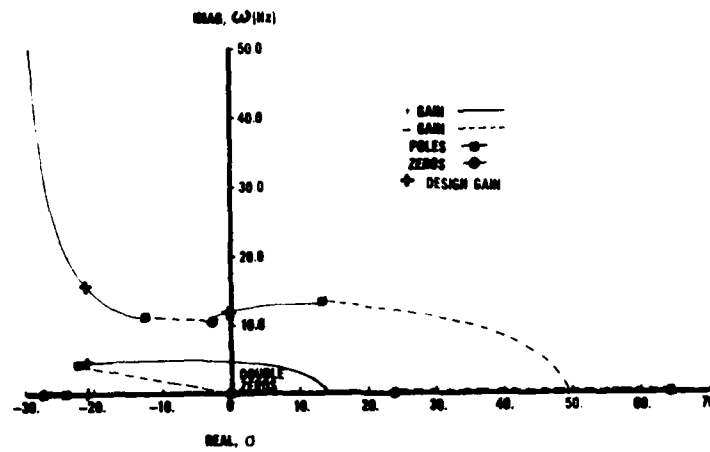
Figure 15 $\dot{\alpha}$ Versus δ_{TE} Gain with $K_{LE} = -5.20$ and $\phi_{TE} = \frac{1 - .04223S}{1 + .04223S}$, Cantilever Wing. $V = 1.2 \, V_{f_p}$

phase lag network results in a potentially unstable zero. However, the gain needed to drive the system unstable is found to be extremely high. The sign of the gain is now positive as a result of the 155 degree phase lag in the system at a frequency near the flutter frequency (155 degree phase lag is equivalent to a change in sign on the gain with 25 degrees lead). The trailing edge design gain (.025 deg/deg/sec^2) is marked on the loci of Figure 15 for reference. For the two-surface control law the gain margins are calculated to be -6.19 db and 18.74 db on the leading edge loop, and minus infinity and 12.04 db on the trailing edge. The phase margins associated with the trailing edge loop are found to be -70 degrees and 25 degrees. The performance of this two-surface feedback system at *off-design* conditions is discussed in detail in the next chapter following the analysis of other model boundary conditions.

Model Free in Pitch

To verify that the Pade' polynomials provide a good fit of the unsteady aerodynamic force coefficients when the model is free in pitch, V-g and V-ω plots are again presented. The V-g and V-ω plots shown in Figure 16 are determined using both a classical k-flutter prediction method and the root locus procedures that employ the Pade' polynomial representation of the

56
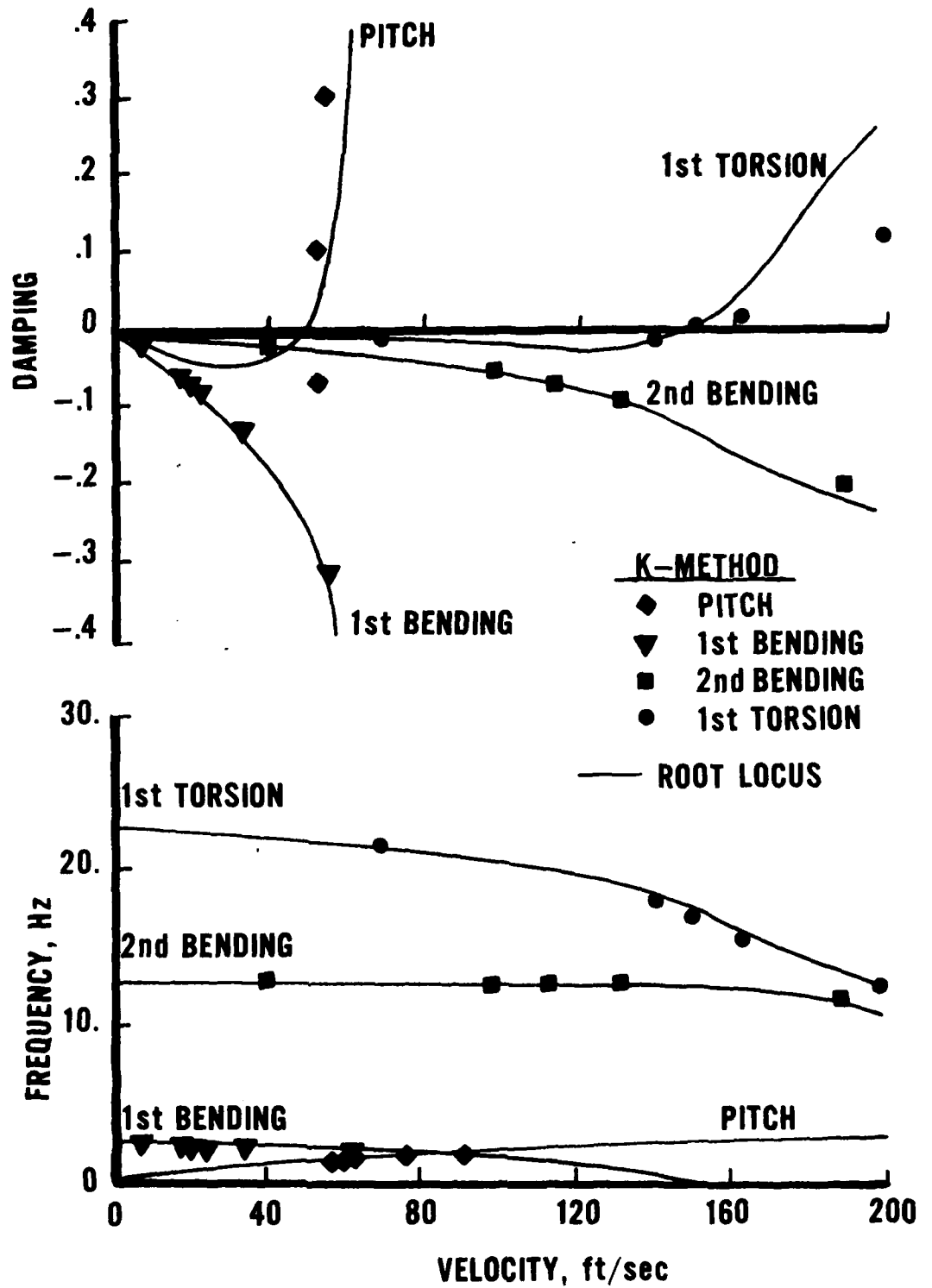
Figure 16   Comparison of V-g and V-ω Plots Using k-Method and Root
            Locus, Model Free in Pitch (Passive Results)

57

generalized forces. Comparisons of damping and frequency with airspeed between the two techniques is excellent indicating that the polynomials accurately represent the unsteady aerodynamics in the reduced frequency range of interest.

Figure 17 presents the velocity root locus plot for the model free in pitch with all systems off (passive solution). The body freedom flutter instability is predicted to occur at 52 ft/sec at 1.2 Hz using the aerodynamics approximated by Pade' polynomials. The mode of instability for this analysis is the rigid pitch mode. This analysis also predicts the higher frequency bending/torsion instability to occur at 151 ft/sec at 16.5 Hz. Classical flutter analysis techniques predict a body freedom instability at 53 ft/sec at 1.2 Hz. Bending/torsion flutter is determined to occur at 156 ft/sec at 16.0 Hz. Correlation of the passive flutter data is quite good also giving an indication that the aerodynamics are accurately represented by the Pade' polynomials.

Figures 18 through 22 present gain root loci with the model free in pitch for displacement and wing twist feedback signals. The five poles represent the rigid pitch mode and the three elastic modes for the unaugmented model at 1.2 V_{fp2}. The poles on the negative real axis represent the 1st bending mode. The
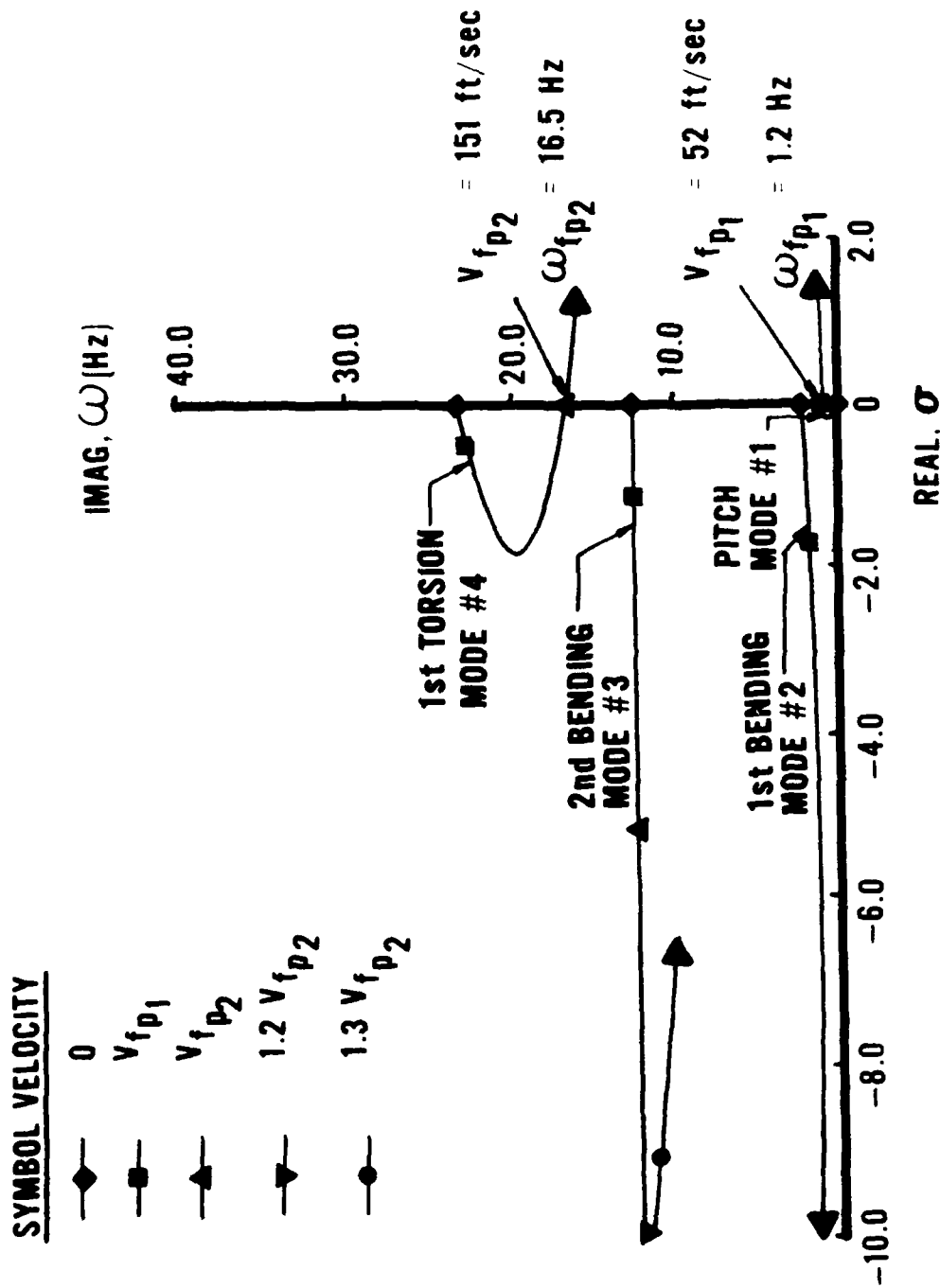
Figure 17 Root Locus Plot for the Model Free in Pitch, Passive Solution
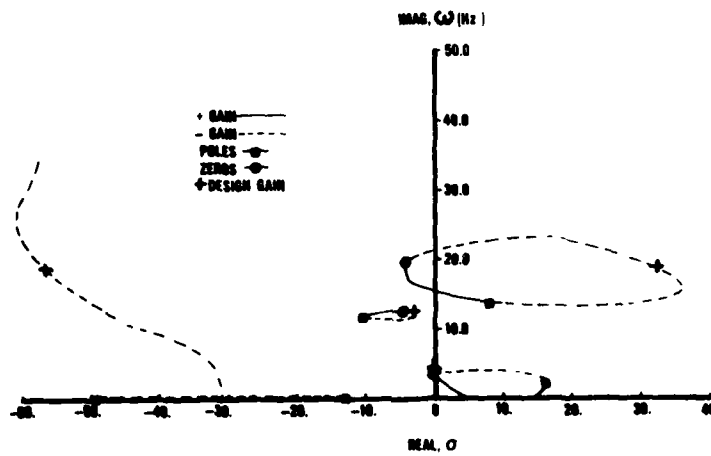
59

Figure 18   h Versus δ_{TE} Gain, Model Free in Pitch, $V = 1.2\ V_{f_{p_2}}$

Figure 19   h Versus δ_{LE} Gain, Model Free in Pitch, $V = 1.2\ V_{f_{p_2}}$

60
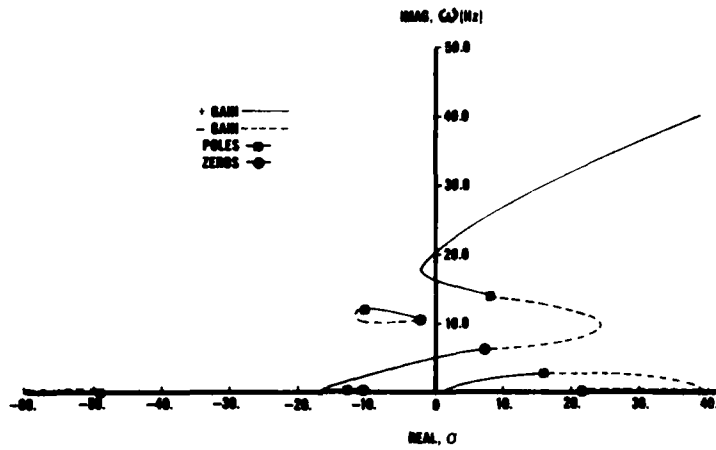
Figure 20   α Versus δ_{TE} Gain, Model Free in Pitch, $V = 1.2\ V_{f_{p_2}}$
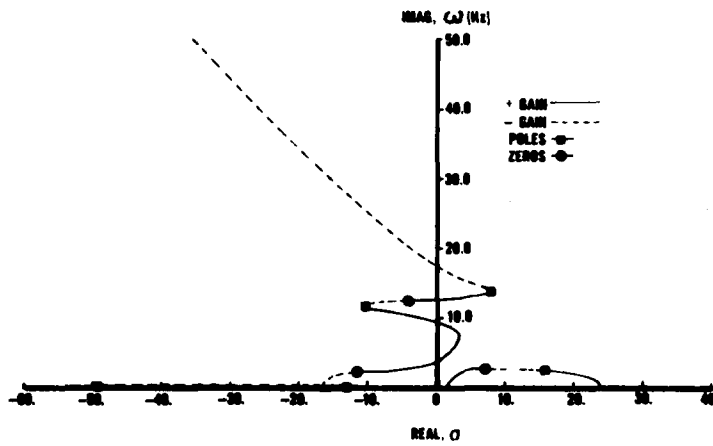
Figure 21   α Versus δ_{LE} Gain, Model Free in Pitch, $V = 1.2\ V_{f_p}$
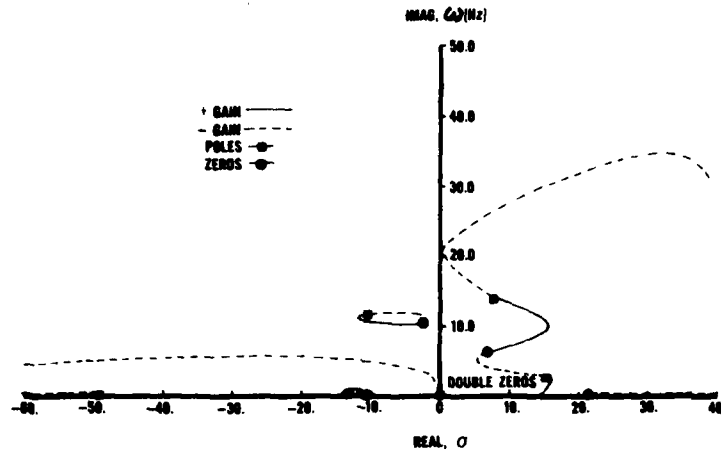
Figure 22 ᾱ Versus δ_{TE} Gain, Model Free in Pitch, $V = 1.2 \, V_{f_{p_2}}$
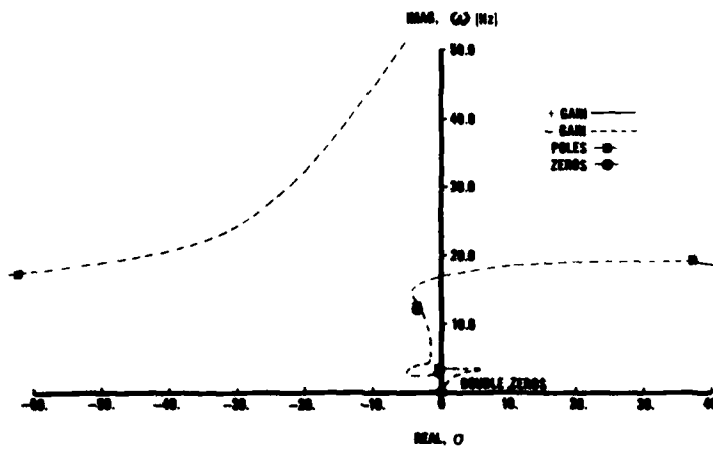
Figure 23 ᾱ Versus δ_{TE} Gain with $K_{LE} = -122.0$, Model Free in Pitch, $V = 1.2 \, V_{f_{p_2}}$

two unstable modes represent the rigid pitch mode at 2.5 Hz and the 1st torsion mode at 13.7 Hz. The stable 2nd bending mode is located at 11.9 Hz. Calculations using displacement feedback with either control surface (see Figures 18 and 19) indicate the possibility of preventing both instabilities simultaneously with a single surface (positive feedback for h/δ_{TE} and negative feedback for h/δ_{LE}). However, analyses at off-design conditions, that is at velocities lower than $1.2\ V_{fp2}$, predict instabilities in other elastic modes as a result of the high gain conditions. When twist of the wing tip (Figures 20 and 21) and angular acceleration (Figure 22) are fed back, analysis finds that no single sensor/control surface combination is capable of preventing both instabilities at the design condition. In fact, these sensor/control surface combinations result in an unstable model for all positive and nega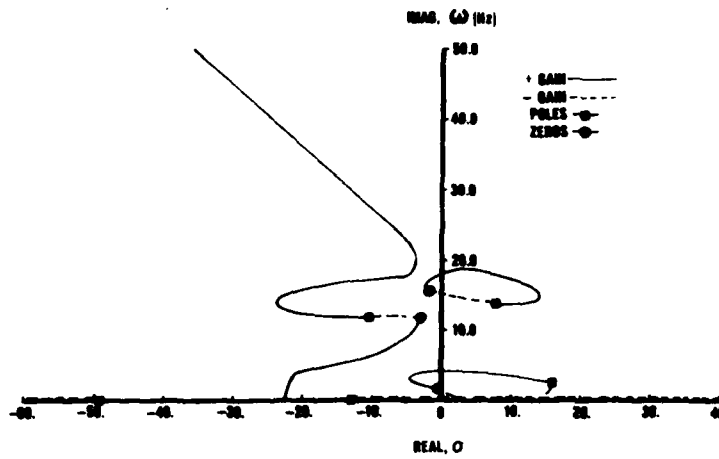tive gains. These signals have no ability for suppressing body freedom flutter. This is attributed to the low frequency zeros in the right half plane.

Previous calculations for the cantilever wing have indicated that two active surfaces are required to prevent the two instabilities simultaneously. As a result negative gain on the leading edge surface with displacement feedback provides the best input for controlling the body freedom flutter instability. This

63

system requires a gain of -122 deg/in to raise the body freedom instability speed up to V_{fp2}, and to provide gain margins of at least ± 6db at V_{fp2}.

To control bending/torsion flutter, the trailing edge surface with angular acceleration feedback is used. Figure 23 provides a root locus of the trailing edge loop with the leading edge loop closed (K_{LE} = -122 deg/in). This figure indicates that negative feedback will stabilize the 1st torsion mode. It also shows that this negative feedback will destabilize the pitch mode over a large range of gains. Figure 24 shows gain loci with a phase lag network included in the trailing edge system compensation. This network, defined to be $\frac{1 - .1531S}{1 + .1531S}$, eliminates the instability in the pitch mode and provides the best phase margins for this configuration and this control logic. Since the phase lag network provides 173 degrees at 17 Hz, the feedback gain for a stable system is now positive as previously described for the cantilever wing. The feedback gain n the trailing edge loop is determined to be .026 deg/deg/sec^2. The combined two-surface control system provides the required speed improvement of 1.2 V_{fp2}. The gain margins on the leading edge system at V_{fp2} are found to be -6.00 db and positive infinity, and on the trailing edge system, -12.74 db and 11.96 db. The phase
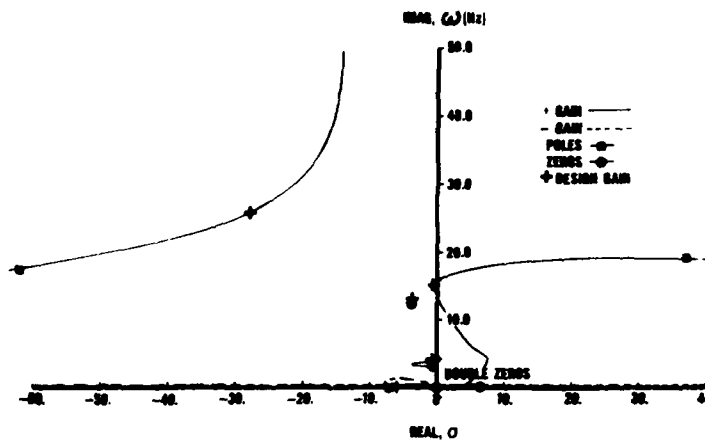
Figure 24 α Versus δ_{TE} Gain with $K_{LE} = -122.0$ and $\phi_{TE} = \frac{1 - .1531S}{1 + .1531S}$, Model Free in Pitch, $V = 1.2\ V_{f_{p_2}}$

65

margins on the trailing edge system are calculated to be
-13.0 degrees and 17.0 degrees. The design gains for
each loop are marked on the loci in Figure 19 (leading
edge loop) and Figure 24 (trailing edge loop).

Model Free in Pitch and Plunge

The V-g and V-ω plots for the model free in pitch
and plunge are provided in Figure 25. The root locus
plot with all gains set to zero (passive solution) is
presented in Figure 26. For this configuration,
coupling to produce the body freedom flutter mode
causes the 1st bending mode to become unstable instead
of the rigid pitch mode as is the case when the model
is free in pitch only. The body freedom instability
speed also increases somewhat with the addition of the
rigid plunge mode. This increase in instability speed
is at least partially attributed to the effect caused by
a free-free boundary condition on the elastic modes.
Body freedom flutter is predicted to occur at 75 ft/sec
at 1.9 Hz using a classical flutter analysis method
while the use of Pade' polynomial fits of the unsteady
aerodynamic force coefficients result in a prediction of
72 ft/sec at 1.9 Hz. For the higher bending/torsion
flutter instability, the classical flutter analysis
method predicts a flutter speed of 153 ft/sec at 16.5 Hz
and by using the Pade' polynomials, the instability is
found at 152 ft/sec at 16.4 Hz. This correlation of

66
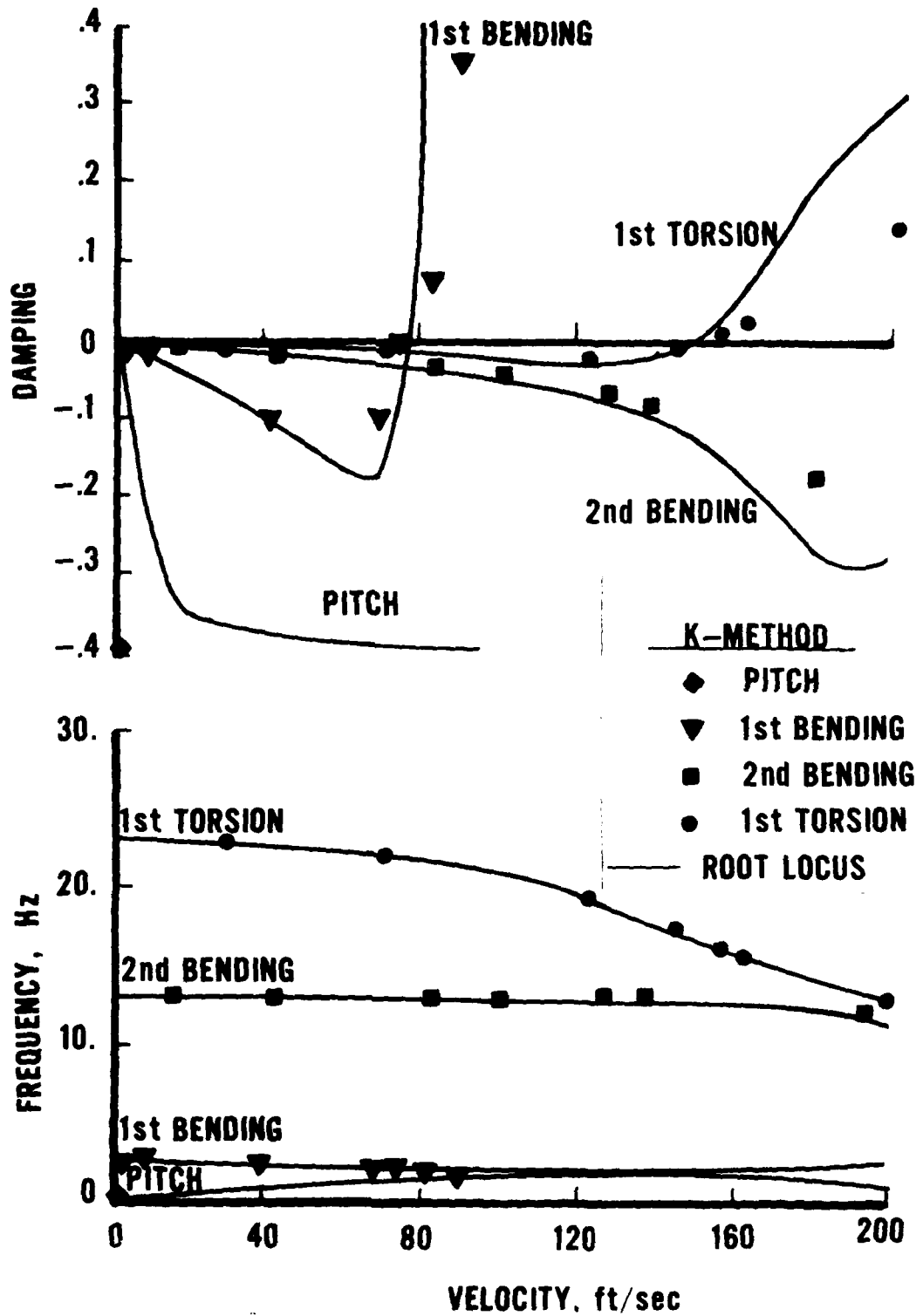
Figure 25 Comparison of V-g and V-ω Plots Using k-Method and Root Locus, Model Free in Pitch and Plunge (Passive Results)
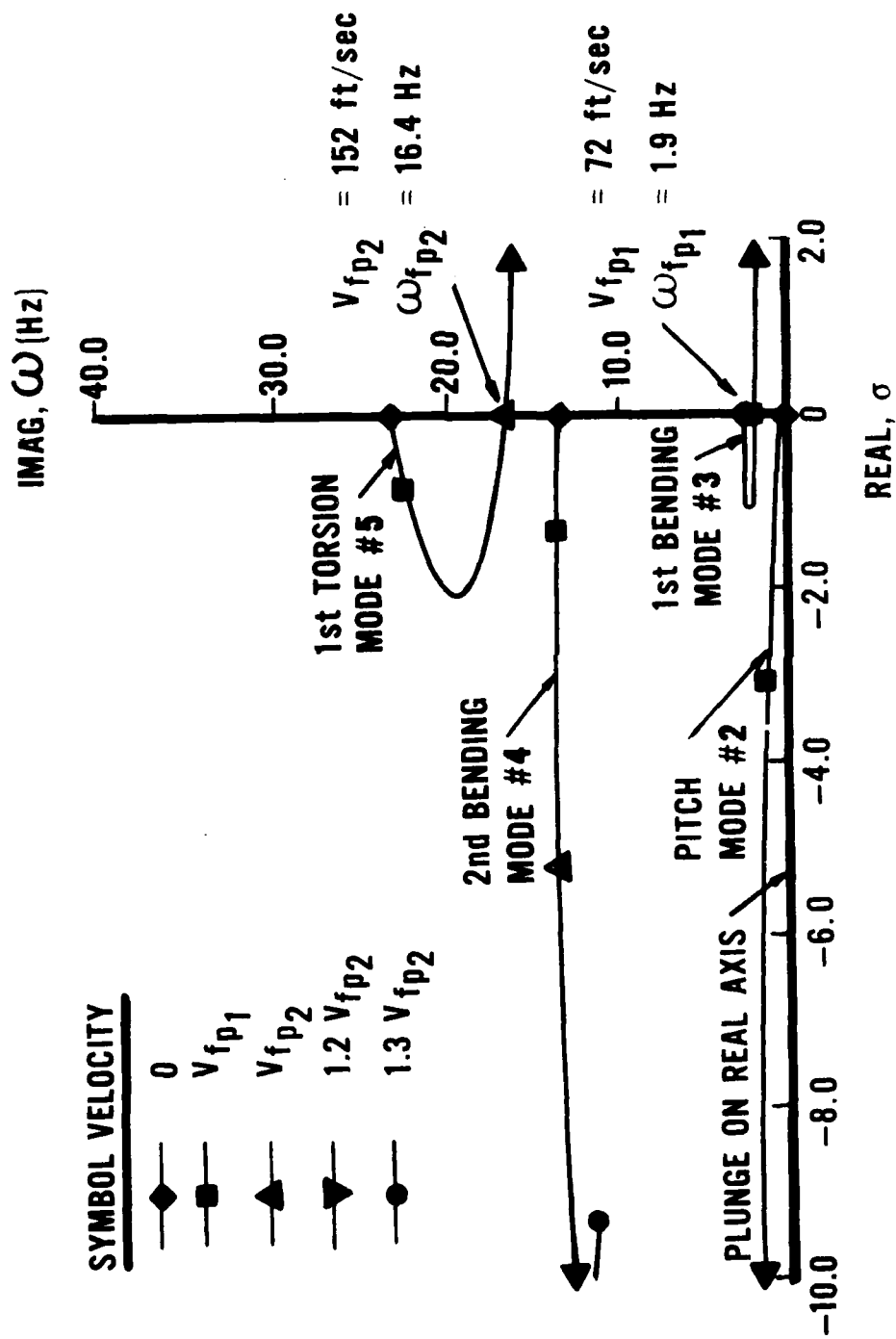
Figure 26 Root Locus Plot for the Model Free in Pitch and Plunge, Passive Solution

flutter characteristics and the comparisons on the V-g and V-ω plots of Figure 25 demonstrate the accuracy of the Pade' fit of the unsteady aerodynamics.

Figures 27 through 30 present the design data used in determining the two-surface control system gains when the model is free in both pitch and plunge. The poles shown in these figures represent the rigid pitch mode and the three elastic modes. The plunge mode lies along the real axis. For this configuration, the two unstable modes have frequencies of 2.1 Hz and 13.9 Hz at 1.2 V_{fp2}. The rigid pitch mode and the 2nd bending mode are both stable at this airspeed and have frequencies of 1.6 Hz and 12.3 Hz, respectively.

Similar conclusions can be drawn regarding displacement feedback, as for the case when the model is free in only pitch. A system using only h/δ_{TE} (Figure 27) with positive feedback or a system using only h/δ_{LE} (Figure 28) with negative feedback can suppress both modes of instability simultaneously at the design airspeed. When wing twist and the trailing edge surface are analyzed (Figure 29), it is found that no gain, negative or positive, can stabilize both modes simultaneously. This is attributed to a real zero in the right half plane. Negative wing twist feedback with the leading edge control surface (Figure 30), however, is found to be capable of suppressing both modes for

69
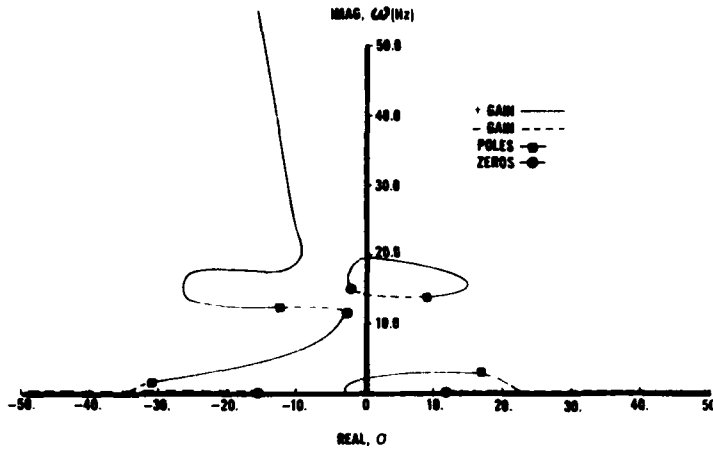
Figure 27   h Versus δ_{TE} Gain, Model Free in Pitch and Plunge,
$V = 1.2 \ V_{f_{p_2}}$
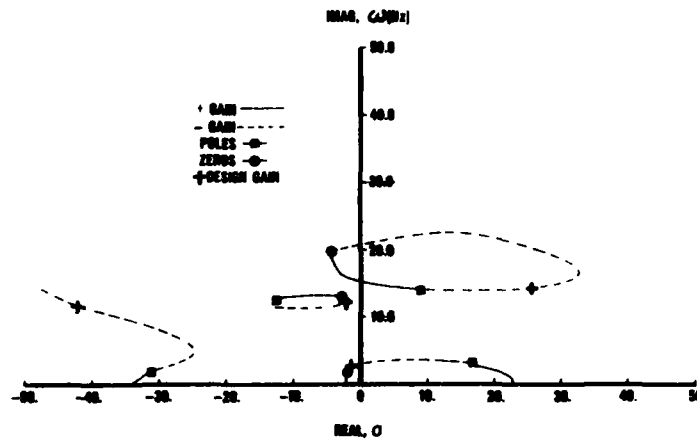
Figure 28   h Versus δ_{LE} Gain, Model Free in Pitch and Plunge,
$V = 1.2 \ V_{f_{p_2}}$
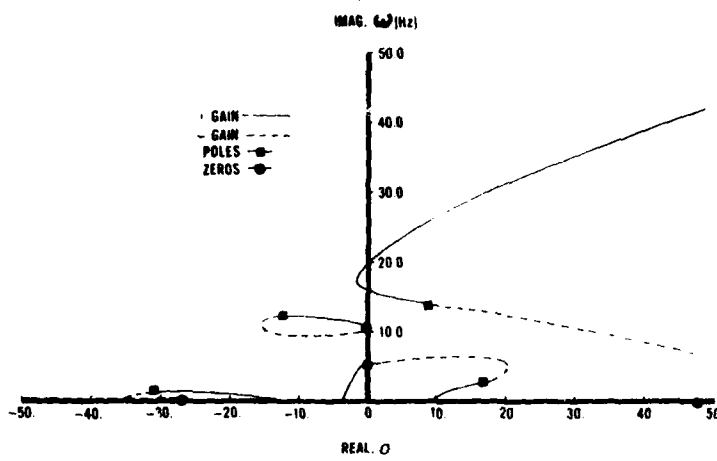
Figure 29 α Versus δ_{TE} Gain, Model Free in Pitch and Plunge,
$V = 1.2 \ V_{f_{p_2}}$

Figure 30 α Versus δ_{LE} Gain, Model Free in Pitch and Plunge,
$V = 1.2 \ V_{f_{p_2}}$

71
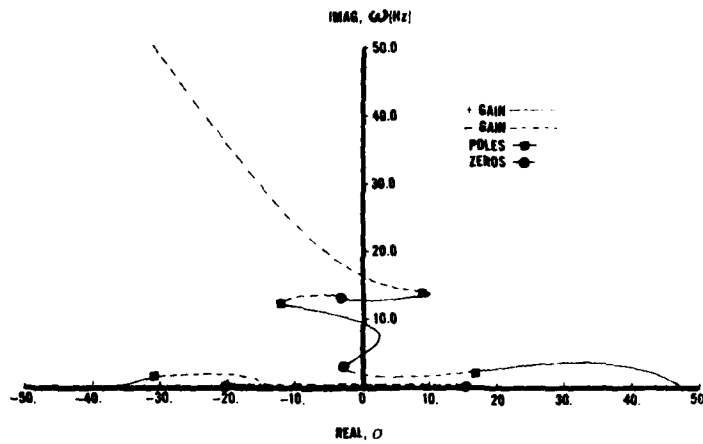
moderate gain levels. Angular acceleration feedback to a trailing edge control surface (Figure 31) is also shown to be inadequate for controlling two unstable aeroelastic modes simultaneously. Analyses at off-design conditions again indicate, however, that no system using only one surface can prevent both instabilities simultaneously over the entire velocity range of interest. Therefore, the two-surface approach defined previously is used to control the model free in pitch and plunge. A gain of -25.2 deg/in on the leading edge control surface with displacement feedback is required to improve the body freedom instability up to 1.2 V_{fp2} with gain margins of at least ± 6db at V_{fp2}. This design gain value is marked in the loci of Figure 28 for reference.

To determine a system for preventing the bending/torsion flutter mode, the leading edge system is closed and gain loci for the trailing edge system are determined (Figure 32). A trailing edge system gain of -.0203 deg/deg/sec^2 is necessary to obtain the required speed improvement and gain margins. To obtain the best phase margins for this type of design, a phase lag network of $\dfrac{1 - .2144S}{1 + .2144S}$ is used. This network provides a phase lag of 175 degrees at 17 Hz. The value of the trailing edge design gain is marked on the loci
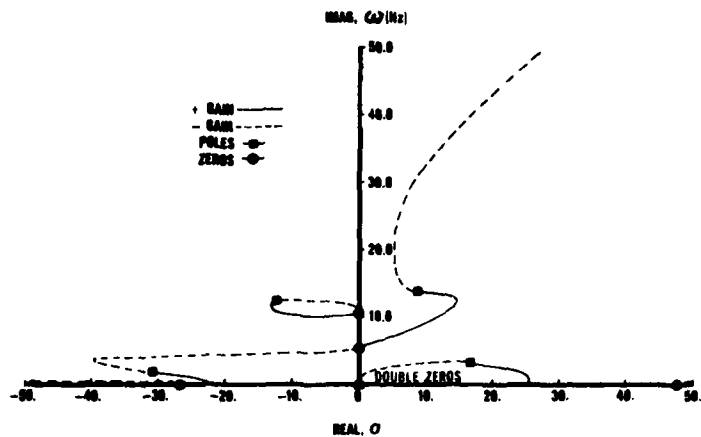
Figure 31   α Versus δ_{TE} Gain, Model Free in Pitch and Plunge,
V = 1.2 $V_{f_{p_2}}$
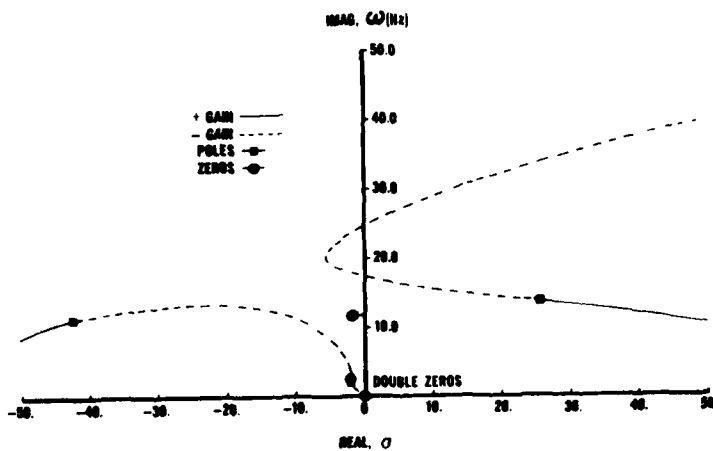
Figure 32   α Versus δ_{TE} Gain with K_{LE} = -25.2, Model Free in
Pitch and Plunge, V = 1.2 $V_{f_{p_2}}$

73

of Figure 33 for reference. The gain margins on the leading edge system are calculated to be -6.00 db and 9.36 db, while the gain margins on the trailing edge system are found to be -10.59 db and 6.19 db. The phase margins are determined to be -59 degrees and 10 degrees on the trailing edge system.

For this study, the root loci associated with various sensor and control surface combinations are obtained as gain is varied from zero to positive and negative infinity. These plots provide the guidance needed in selecting the sensors, control surfaces and compensation required to obtain satisfactory performance from the system at a design airspeed. In the next chapter, velocity root locus plots of each of these control laws will be provided. Also, velocity versus damping and velocity versus frequency plots will be determined for system evaluation. This information is important in assuring that the system does not destabilize the aircraft at off-design conditions. If the system is predicted to be unstable at off-design conditions, additional analyses will be required for redesign or some adaptive control scheme that changes the gain or phase lags with velocity, Mach number or dynamic pressure will be needed.
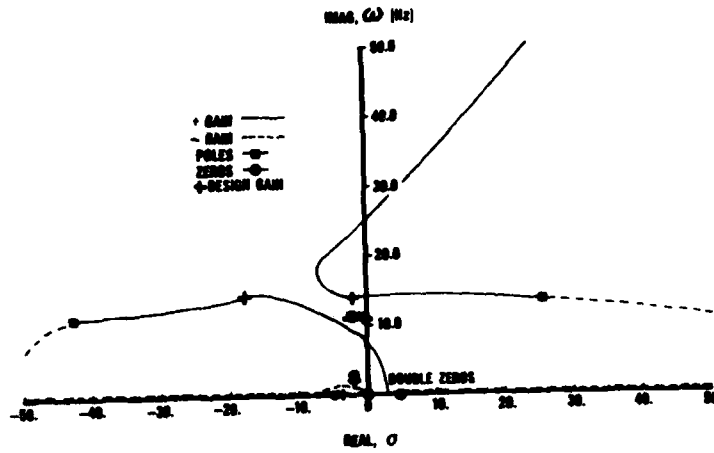
Figure 33 α Versus δ_{TE} Gain with $K_{LE} = -25.2$ and $\phi_{TE} = \dfrac{1 - .2144S}{1 + .2144S}$.
Model Free in Pitch and Plunge, $V = 1.2\ V_{f_{p_2}}$

CHAPTER V

RESULTS

The control laws designed in the previous section for each of the three wing boundary condit'ons are designed at a point velocity. The schematic shown in Figure 34 illustrates the logic of the feedback systems although the information on this chart represents only the case when the model is free in pitch. It is important now to determine the performance of the control system over the entire velocity range of interest and to compare these data with the unaugmented results (K_{LE} and K_{TE} set to zero).

Cantilever Wing

The velocity root locus for the cantilever wing two-surface control law is presented in Figure 35. This control system is shown to improve the velocity flight envelope of the cantilever model 63 percent based on the design criteria. The divergence mode is completely eliminated by the leading edge system, and the bending/torsion flutter mode is increased to the design goal with the trailing edge system. With the system operating, flutter occurs in the 2nd bending mode at a speed of 188 ft/sec instead of in the torsion mode as was the case when the system was off.

76
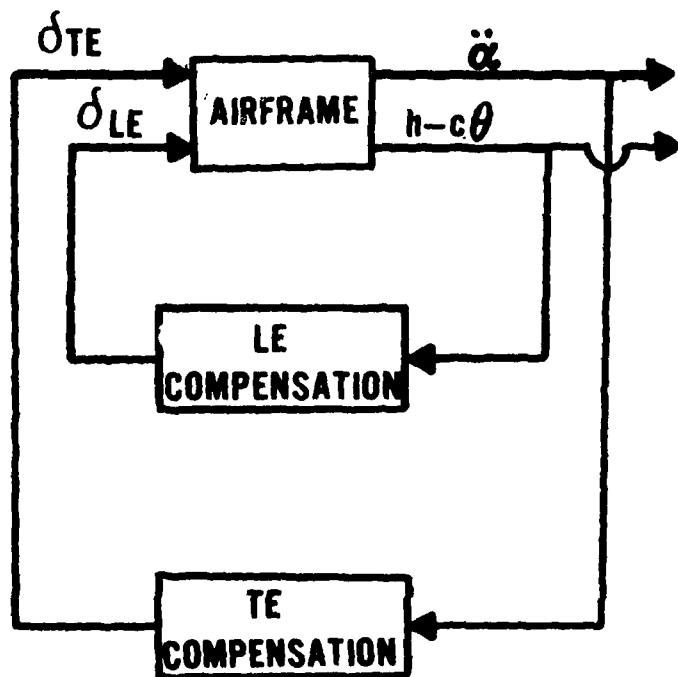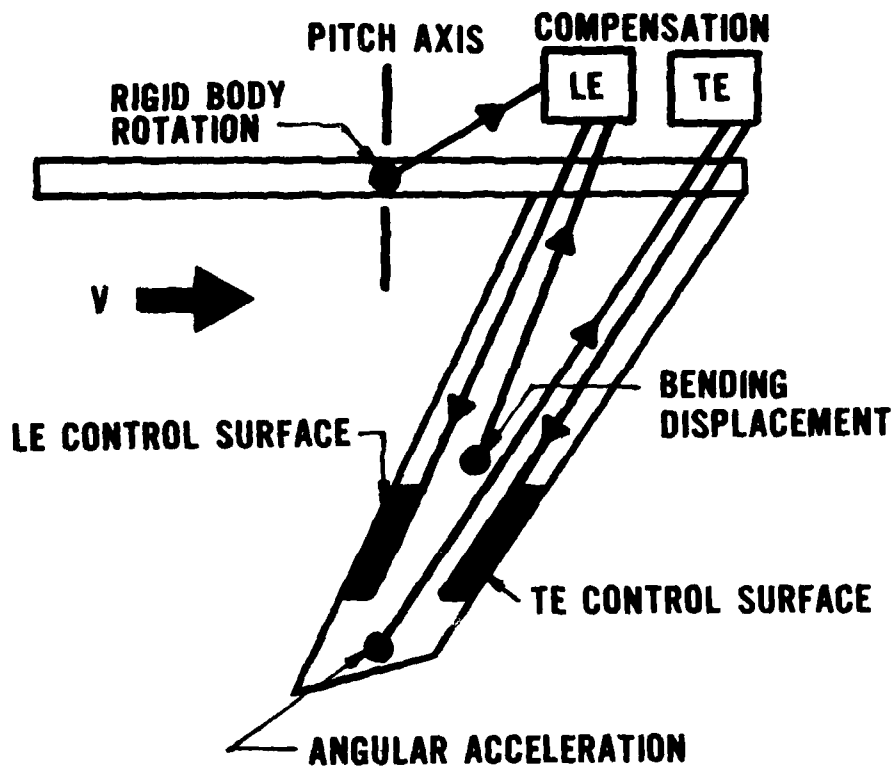
Figure 34   Schematic of Feedback System for Controlling Static
Divergence and Flutter
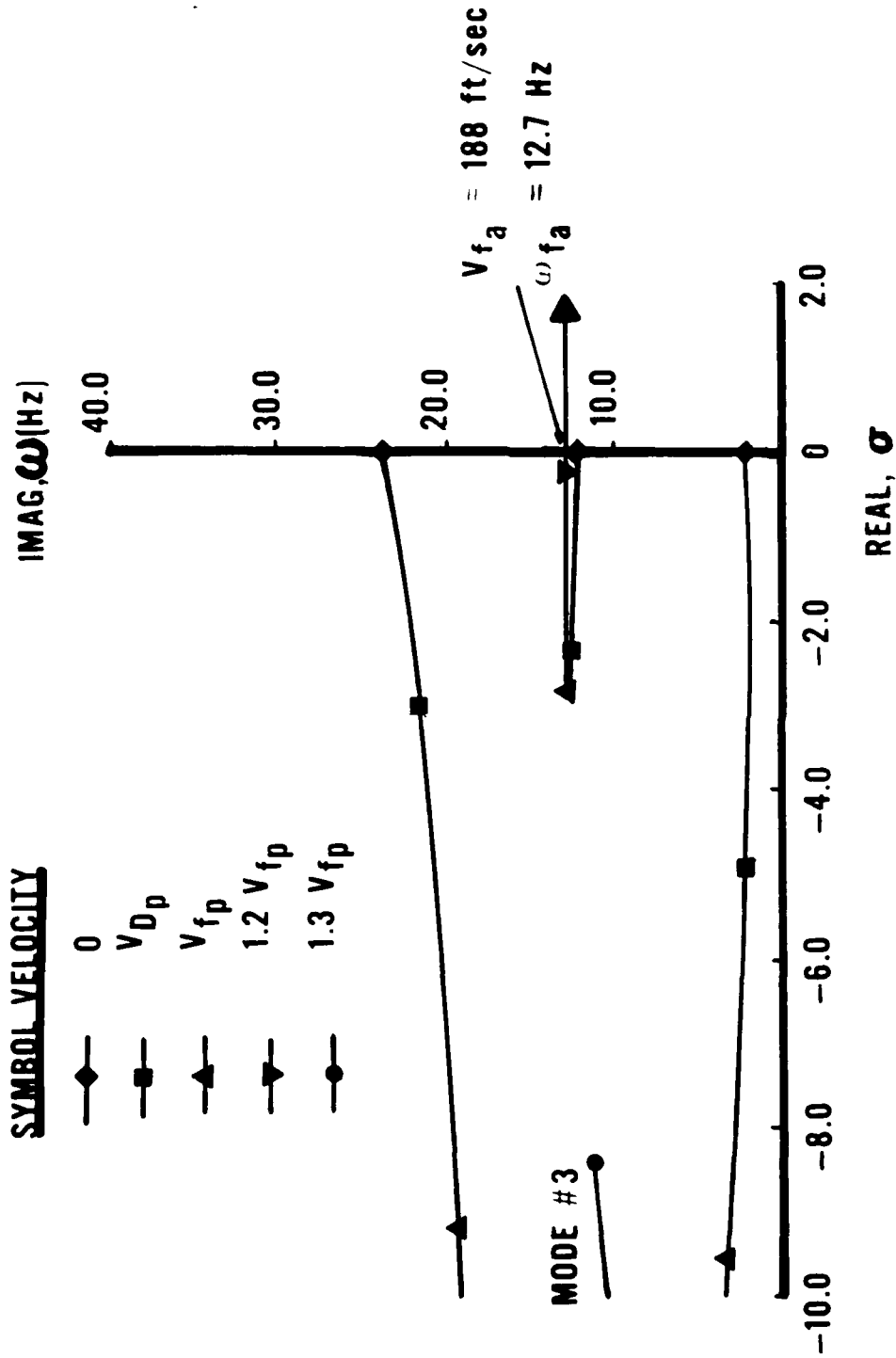
Figure 35 Root Locus for the Cantilever Wing, Nominal Two-Surface Control System ($K_{LE} = -5.2$, $K_{TE} = .025$, $\phi_{TE} = 155°$ @ 17 Hz)

Velocity versus damping and velocity versus frequency trends for the nominal two-surface system on and off are presented in Figure 36. This information is obtained from the unaugmented and augmented velocity root locus plots for the cantilever wing (Figures 8 and 35). These types of plots represent key information used by the flutter engineer to determine the aeroelastic stability of an aircraft. Typically, flutter occurs when the damping associated with some particular elastic mode becomes zero; static divergence occurs when both the damping and the frequency become zero.

Additional analyses are performed to determine the sensitivity of the control law to changes in the feedback gain of each loop or to changes in the phase lag network. The next few figures present the effects of changing one of the feedback parameters while holding the other two constant at nominal values.

A velocity root locus with leading edge gain (K_{LE}) variations ($\pm$ 6db) from nominal is presented in Figure 37. Variations in the leading edge gain are shown to have very little effect on the higher frequency bending/torsion flutter mode. Increasing, K_{LE}, however, did cause a slight drop in the flutter frequency. This effect along with the significant aerodynamic stiffening

END

DATE
FILMED

7 84

DTIC
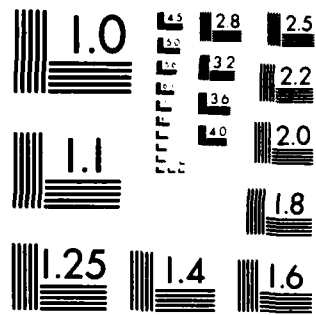
MICROCOPY RESOLUTION TEST CHART

NATIONAL BUREAU OF STANDARDS 1963 A
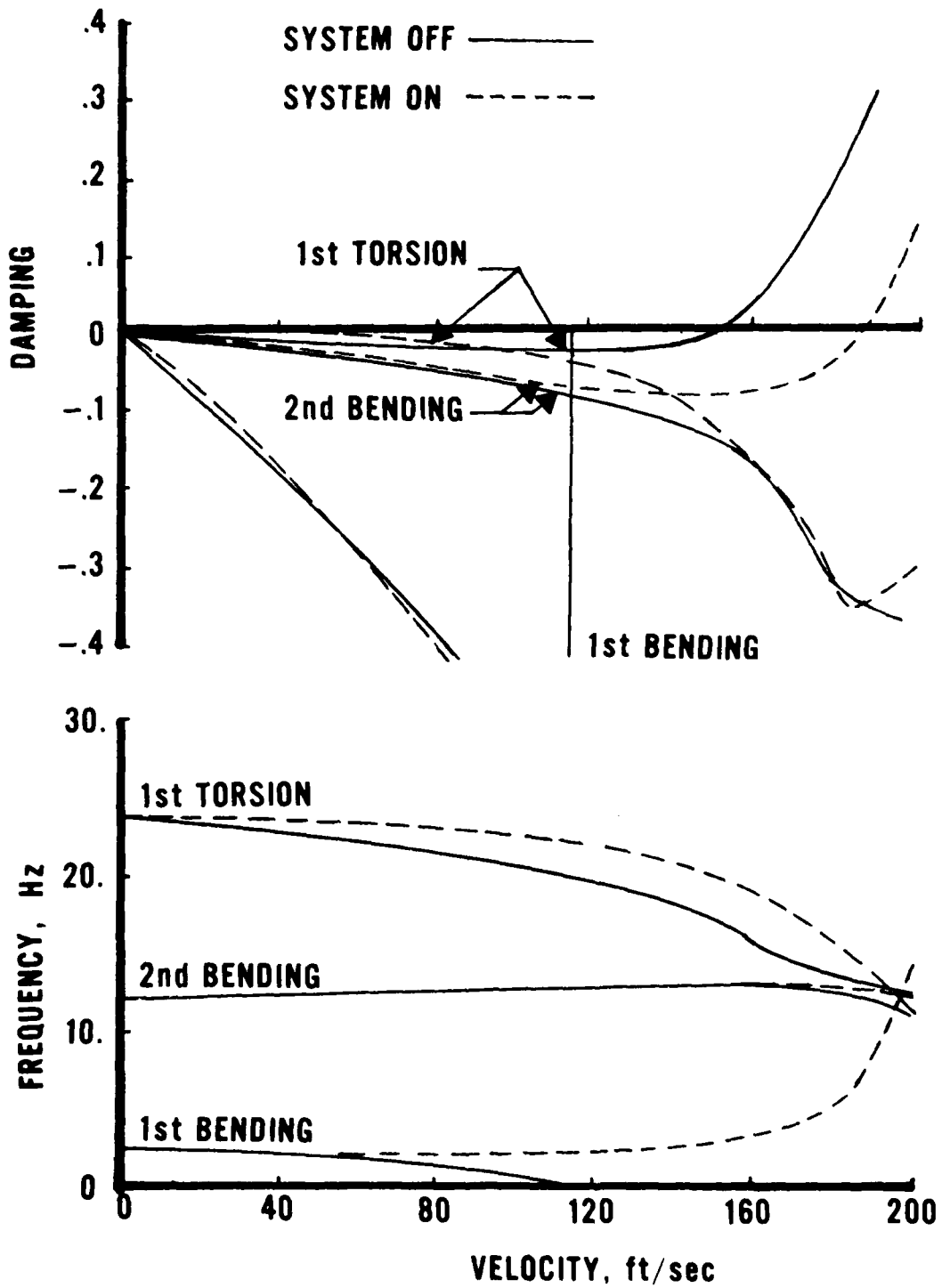
Figure 36 Comparison of V-g and V-ω Plots, Two-Surface Control System Operating and Off, Cantilever Wing

in the first bending mode ultimately results in a switch in the mode of instability for high absolute values of K_{LE}. Figure 37 shows the tendency of the 1st bending mode to swing back towards the right half plane for the larger gain values (see Figure 40 for additional insight).

The effect of trailing edge gain (K_{TE}) variations from nominal for the cantilever wing is presented in Figure 38. Once again, the gain is varied ± 6db from nominal. Trailing edge gain is shown to significantly affect both of the higher two elastic modes, but the 1st bending mode is not at all affected for this range of gain variation. This is attributed to the frequency range of the 1st bending mode and the angular acceleration signal being used by the trailing edge control law. This figure also very clearly illustrates the effect of K_{TE} on a mode of instability switching that takes place between the 2nd bending and torsion modes. As K_{TE} is increased, the instability speed resulting from the torsion mode increases while the frequency decreases. This continues until a switch occurs in the mode of instability from the torsion mode to the 2nd bending mode. Higher K_{TE} values cause the aerodynamic stiffness in the torsion mode to increase. This ultimately causes the torsion mode root locus to bend back towards the right half plane on the upper side
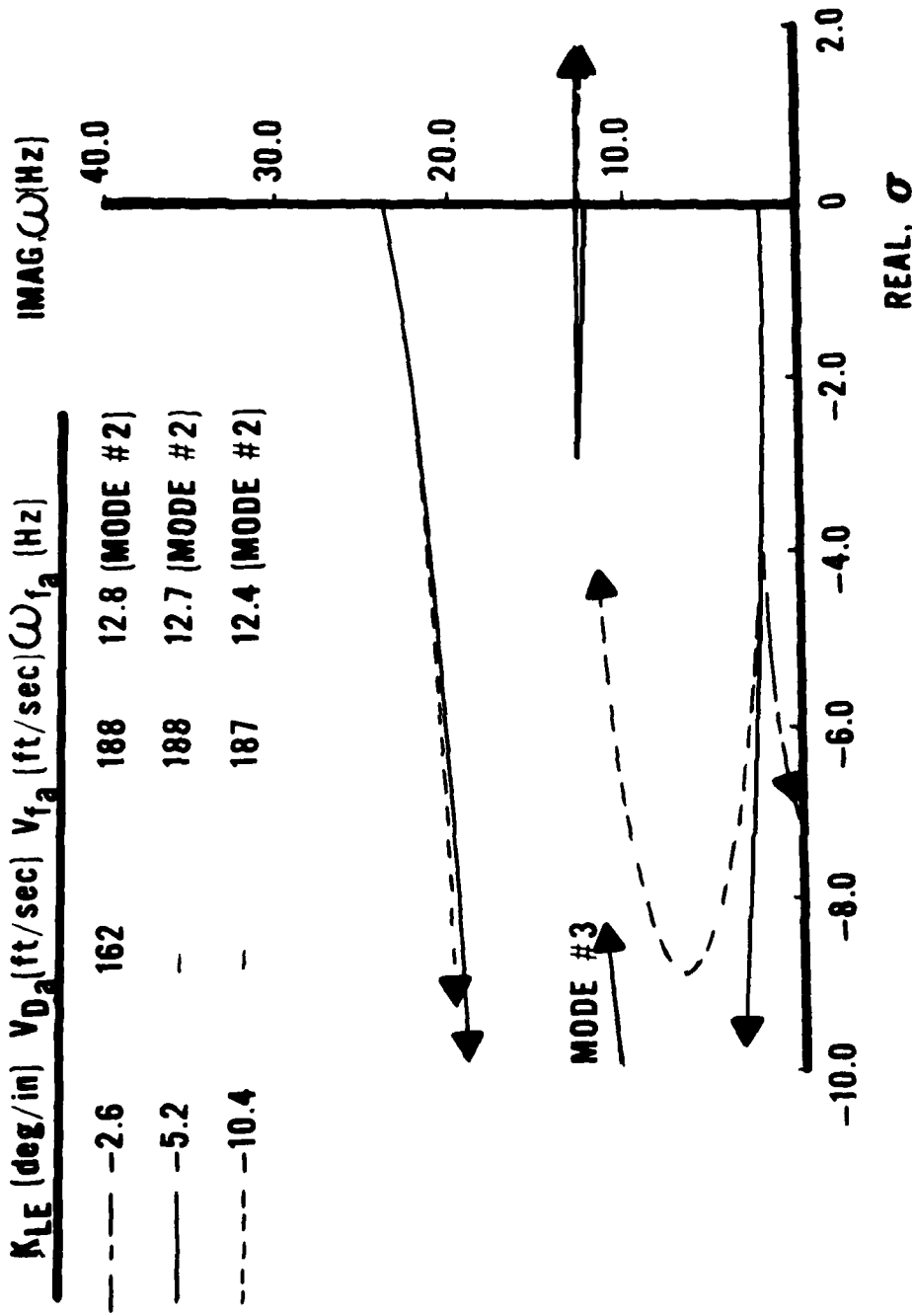
Figure 37 Effect of Leading Edge Gain Variations, Cantilever Wing (Nominal K_{TE} and ϕ_{TE})

82
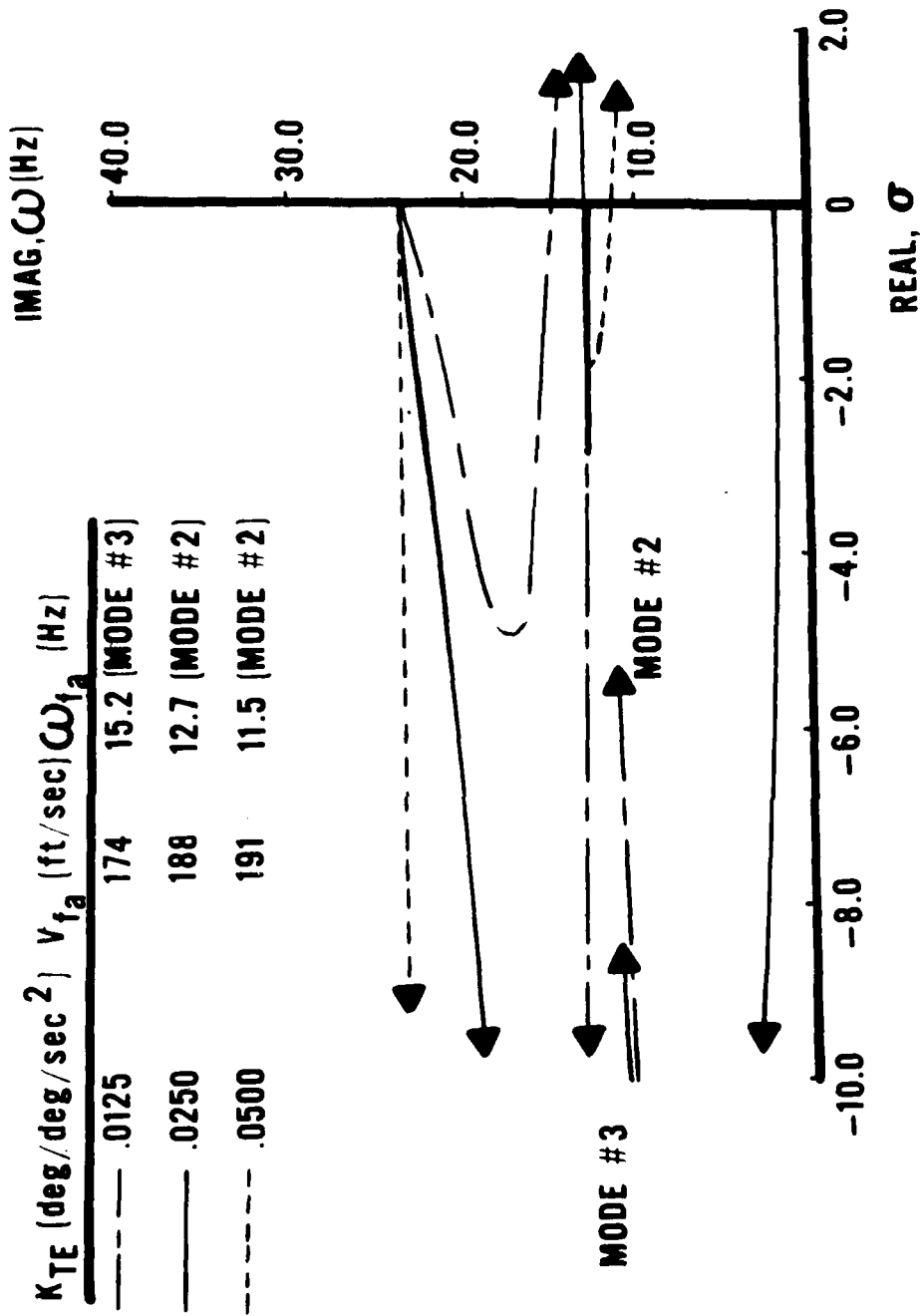
Figure 38 Effect of Trailing Edge Gain Variations, Cantilever Wing (Nominal K_{LE} and ϕ_{TE})

of the torsion natural frequency and causes a control induced instability (see Figure 41). The existence of this control induced instability is somewhat questionable since higher frequency elastic modes are not included in the analysis.

A sensitivity analysis is also conducted to evaluate the effect of changes to the phase lag network. The results of this analysis are summarized in Figure 39. For this analysis the time constant in the phase lag network is varied in an attempt to obtain $\pm$ 45 degrees changes from nominal at a reference frequency of 17 Hz. As shown in Figure 39, a -45 degree change from nominal is achievable but a +45 degree change is not. At phase lag angles slightly greater than 180 degrees, the instability speed resulting from the torsion mode drops very rapidly. In fact, the torsion root continues to migrate towards the right half plane with further increases in phase lag to a point where the root is unstable at all velocities. This analysis also indicates that trailing edge phase does not significantly affect the 1st bending mode root.

Stability boundaries for the cantilever two-surface control law are provided in Figures 40 through 42. The stability boundaries are determined with respect to each of the feedback parameters K_{LE}, K_{TE}, and ϕ_{LE}. The solid circles on the boundaries represent data taken from the

84
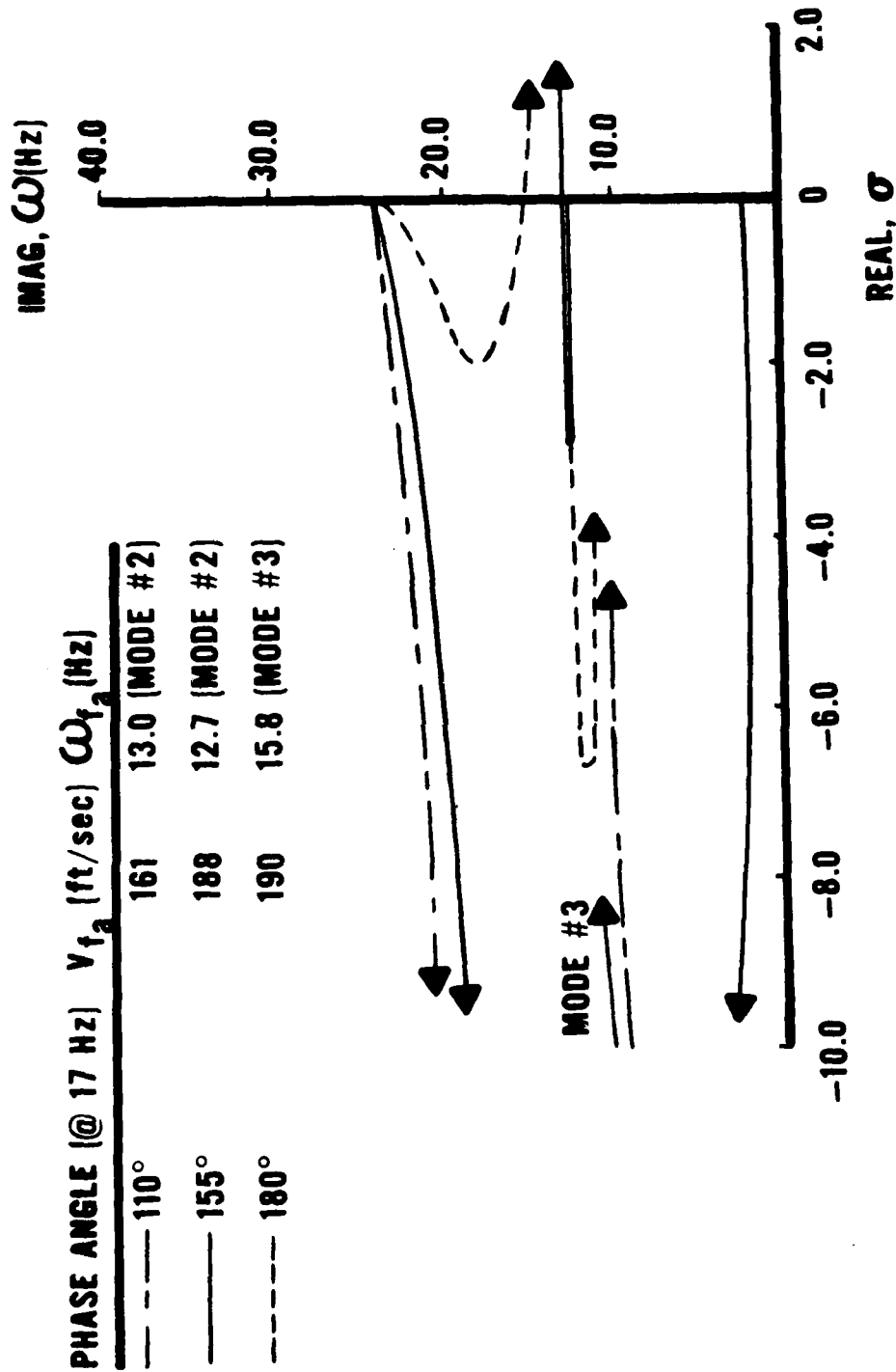
Figure 39 Effect of Trailing Edge Phase Angle Variations, Cantilever Wing (Nominal K_{LE} and K_{TE})
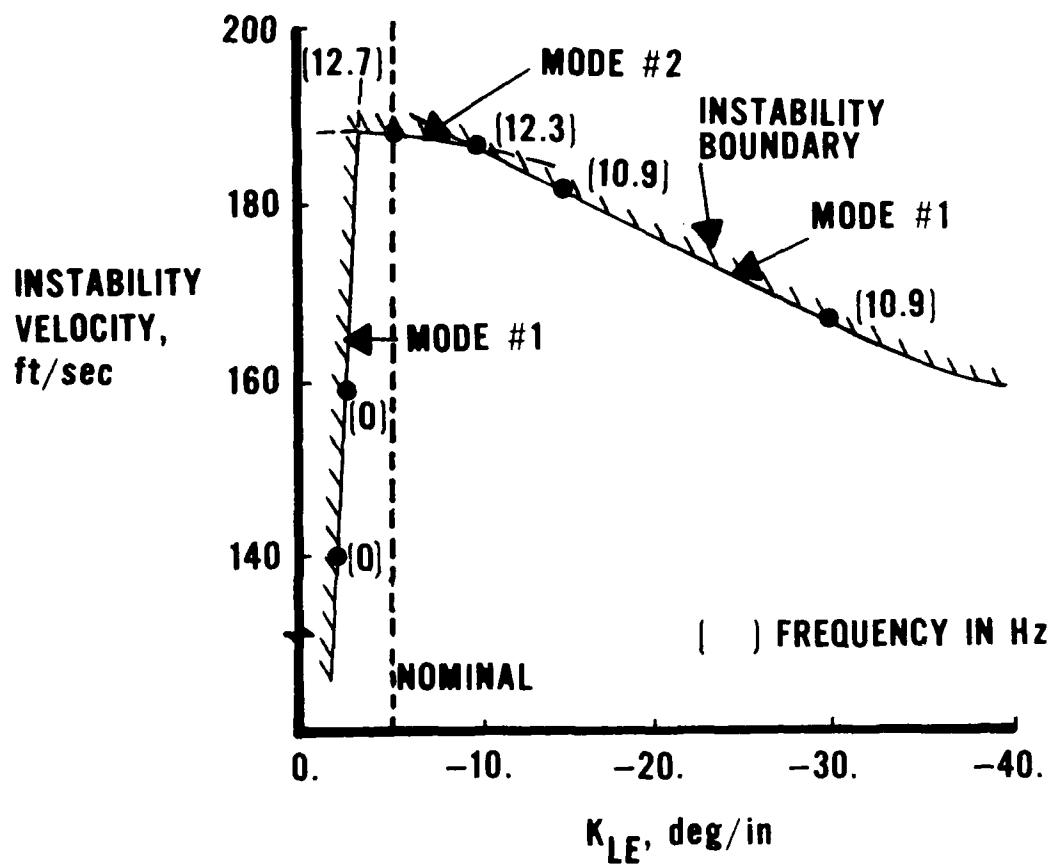
Figure 40 Stability Boundary with Variable K_{LE}, Cantilever Wing
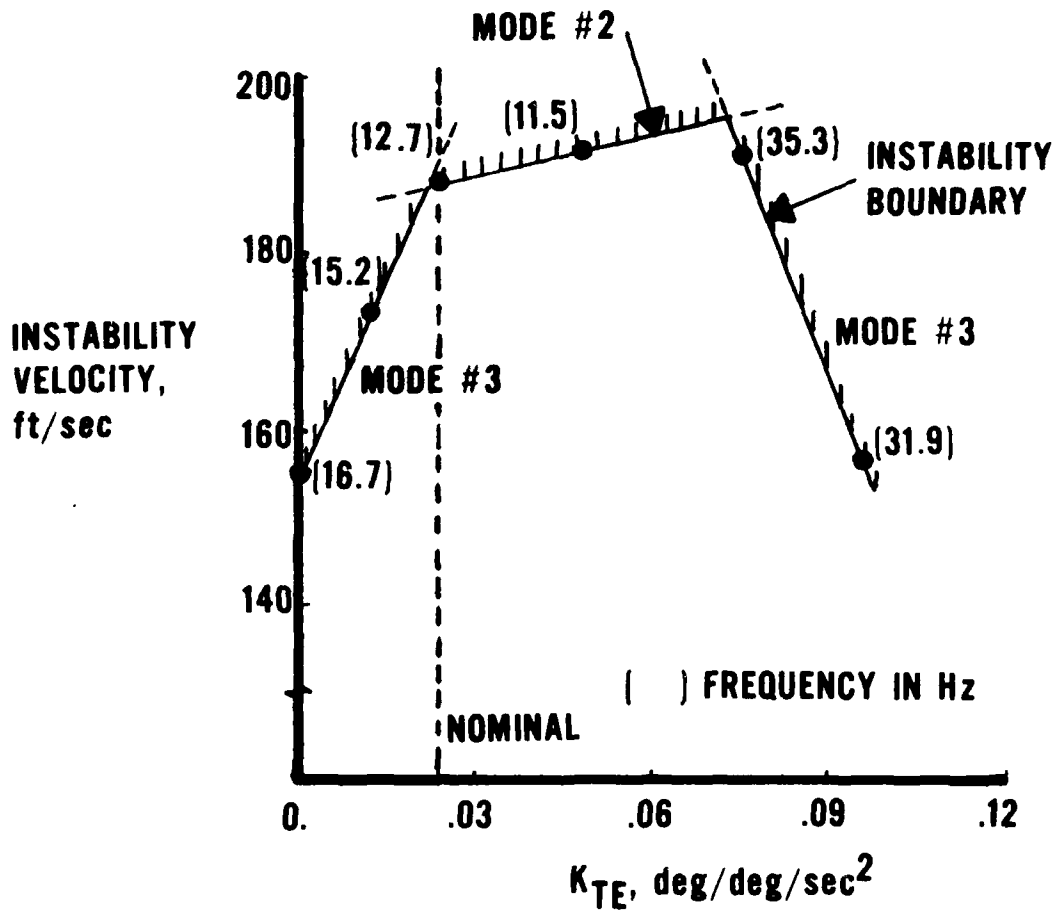
Figure 41 Stability Boundary with Variable K_{TE}, Cantilever Wing
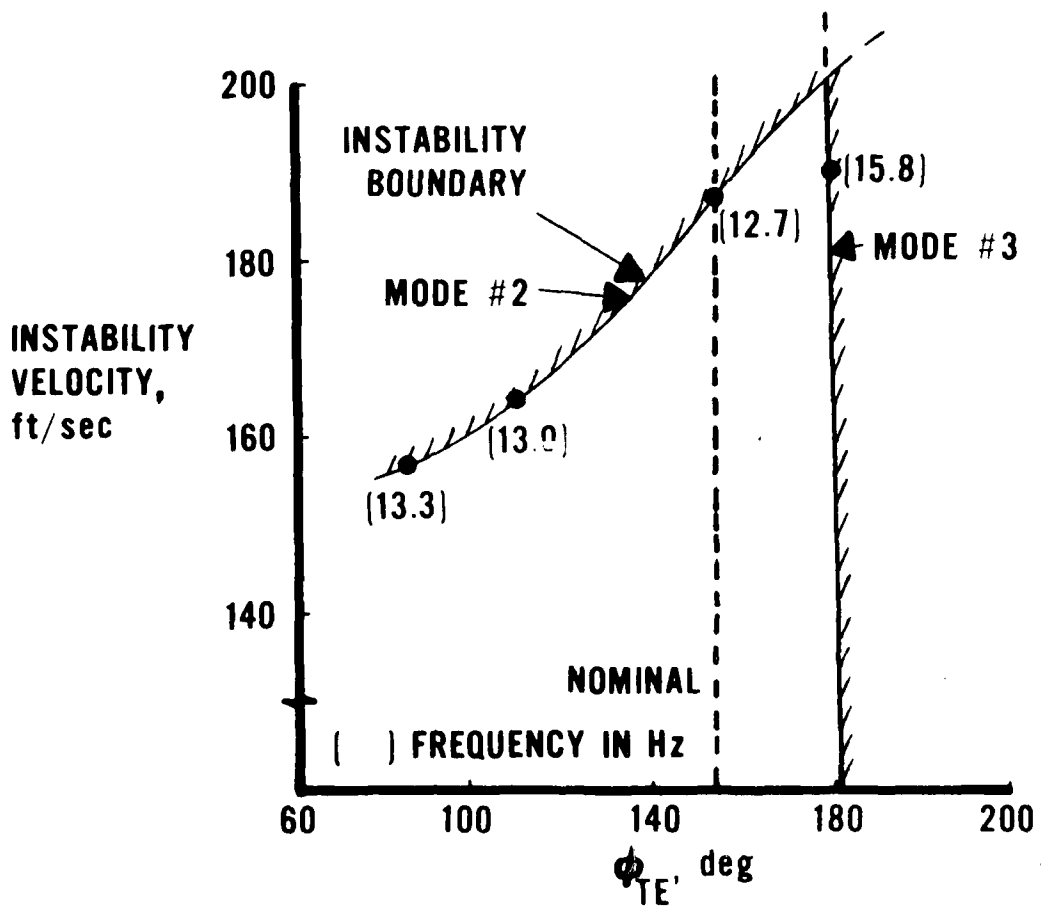
Figure 42 Stability Boundary with Variable ϕ_{TE}, Cantilever Wing

previous root locus plots, and the frequencies of the instability are shown in parentheses. The vertical dashed line represents the nominal control law. Once again, as one of the three parameters is varied, the other two are held constant at nominal values. Gain and phase margins can be easily determined from these figures. This is accomplished by projecting a horizontal line through a reference velocity on the figure and reading the gains or phase angles at the instability boundaries that the line intersects. These gains and phase angles are then compared to the nominal control law to determine the margins. A gain margin of -6db or less indicates that the feedback gain can be divided by a factor of two or more and the active system will continue to stabilize the model at the reference velocity. A gain margin of +6db or more indicates similar characteristics after multiplying the feedback gain by two or more. The positive and negative phase margins are similarly defined; that is, a phase margin of ± 45 degrees indicates that an angle of ± 45 degrees can be added to the system before neutral stability is obtained. These margins are factors of safety that are established for a control system design. These are needed to account for the uncertainties, either neglected or unknown, that are encountered in an analysis.

As K_{LE} is varied from 0. to -40. deg/in (Figure 40), the stability boundary changes from static divergence (mode #1) at low K_{LE}, to a dynamic instability involving the 2nd bending mode at moderate K_{LE}, and finally back to a dynamic instability involving the 1st bending mode at high K_{LE}. The intersection of the stability boundaries to the left of the nominal law represents a switching of the origin of the mode of instability and resembles a smooth transition from one mode to the other. Recall from Figure 37 that the 1st bending mode shows a tendency to be driven unstable with higher values of K_{LE}. The instability transition shown in Figure 40 demonstrates this change from mode #2 to mode #1 as expected. The gain margins on K_{LE} calculated at V_{fp} (as indicated previously) are -6.19 db and 18.74 db. This means that the gain can be decreased 51 percent or increased 8.6 times nominal before neutral stability is obtained.

Figure 41 presents a trend of the stability boundary with K_{TE}. The intersection of the boundaries to the left of the nominal control law shows a transition from mode #3 to mode #2, while the intersection of boundaries to the right shows an actual switching of the mode of instability back to mode #3. Figure 38 provided an indication that the torsion mode can be driven unstable at high K_{LE}. The gain margins on

90

K_{TE} at V_{fp} are found to be negative infinity and 12.04 db. The gain margin of negative infinity on the trailing edge surface is a result of selecting V_{fp} as a reference speed ($K_{TE} = 0$) to measure gain and phase margins.

The stability boundary resulting from a variation of ϕ_{TE} is shown in Figure 42. For this case the intersection of stability boundaries is in the classical manner. The instability speed involving mode #3 drops very rapidly with phase angle changes slightly greater than 180 degrees. The 155 degree phase lag at 17 Hz is the minimum phase angle at which a velocity improvement of 1.2 V_{fp} can be reached. Lower phase angles result in lower speed increases but higher phase margins; higher phase angles result in higher speed increases but lower phase margins. This trend continues up to about 182 degrees phase angle at which time further increases cause low speed instabilities. Phase margins of at least ± 45 degrees can be obtained if the desired flight envelope expansion is limited to 53 percent (13 percent above V_{fp}). Although not investigated, notch filters can be used to improve the gain and phase margins for some cases.

Model Free in Pitch

The velocity root locus for the two-surface control law developed for the model free in pitch is presented

in Figure 43. This system decouples the 1st bending and
rigid pitch modes, and the 1st torsion and 2nd bending
modes through the addition of aerodynamic stiffness.
The increasing aerodynamic stiffness does, however,
cause the 1st bending mode to become unstable at the
design airspeed thus becoming the critical mode of
interest. As a result of eliminating the body freedom
instability, the velocity flight envelope of the model
free in pitch is increased 252 percent using the active
system.

Figure 44 provides the velocity versus damping and
velocity versus frequency plots for the model free in
pitch with the system operating and off. This figure
illustrates a potential low speed hump mode instability
involving the rigid pitch mode between 40 and 80 ft/sec
when the system is operating. Hump modes in general are
sensitive to small perturbations in the aeroelastic
system and to changes in feedback parameters. The
degree of sensitivity of this mode to the feedback
parameters will be illustrated in later figures (see
Figures 45 and 48).

The effect of varying the leading edge gain ± 6db
from nominal is illustrated in Figure 45. Because of the
high gain associated with the leading edge control law,
the wing torsion mode is somewhat affected, although not
to the degree that the pitch mode and wing 1st bending

92

IMAG, ω(Hz)

40.0

30.0

20.0

10.0

$V_{f_a} = 183$ ft/sec

$\omega_{f_a} = 14.9$ Hz

2.0

0

-2.0

-4.0

-6.0

-8.0

-10.0

REAL, σ

SYMBOL VELOCITY

0

$V_{f_{p_1}}$

$V_{f_{p_2}}$

1.2 $V_{f_{p_2}}$

1.3 $V_{f_{p_2}}$

93
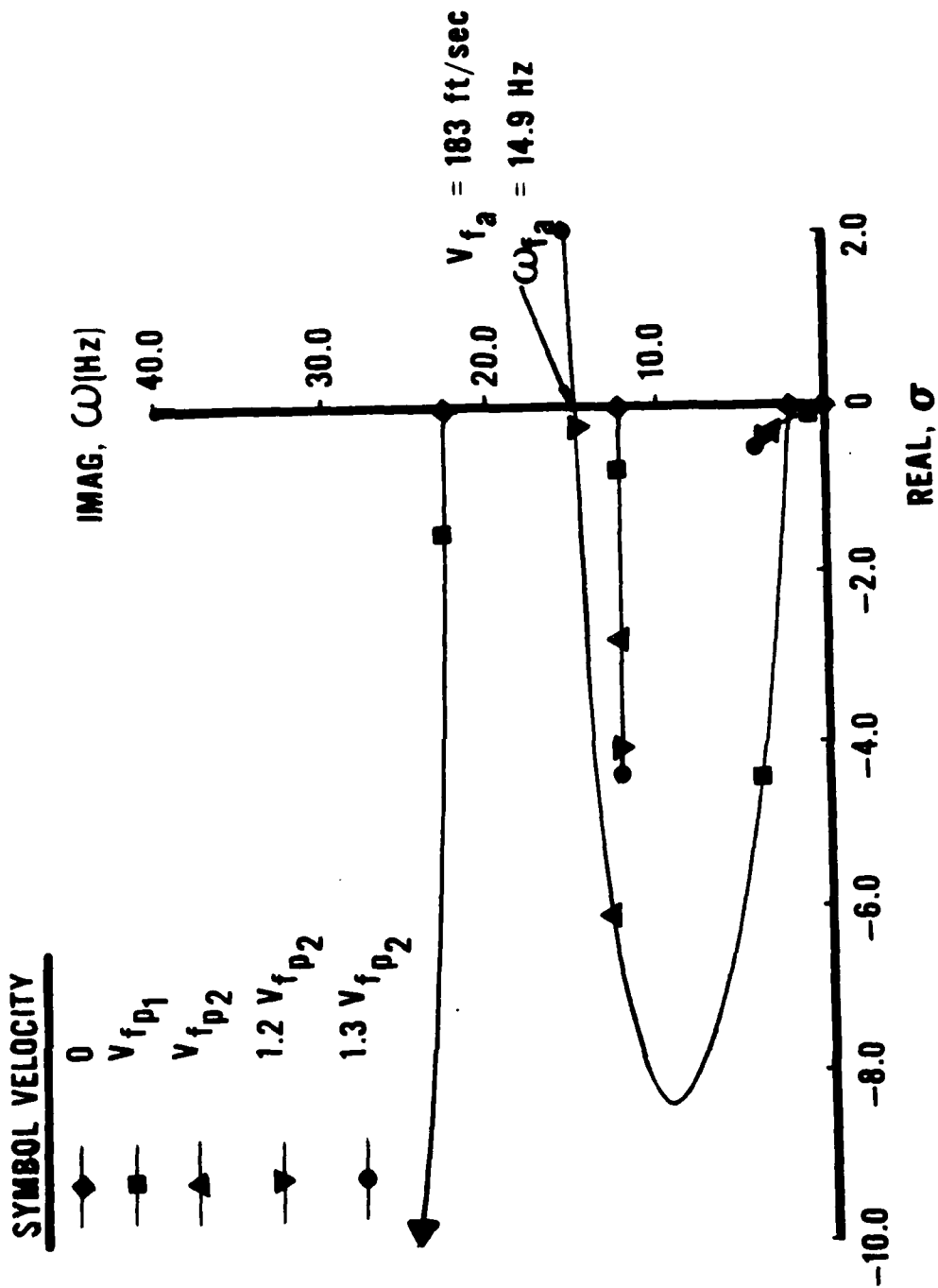
Figure 43 Root Locus for the Model Free in Pitch, Nominal Two-Surface Control System ($K_{LE} = -122.0$, $K_{TE} = .026$, $\phi_{TE} = 173°$ @ 17 Hz)
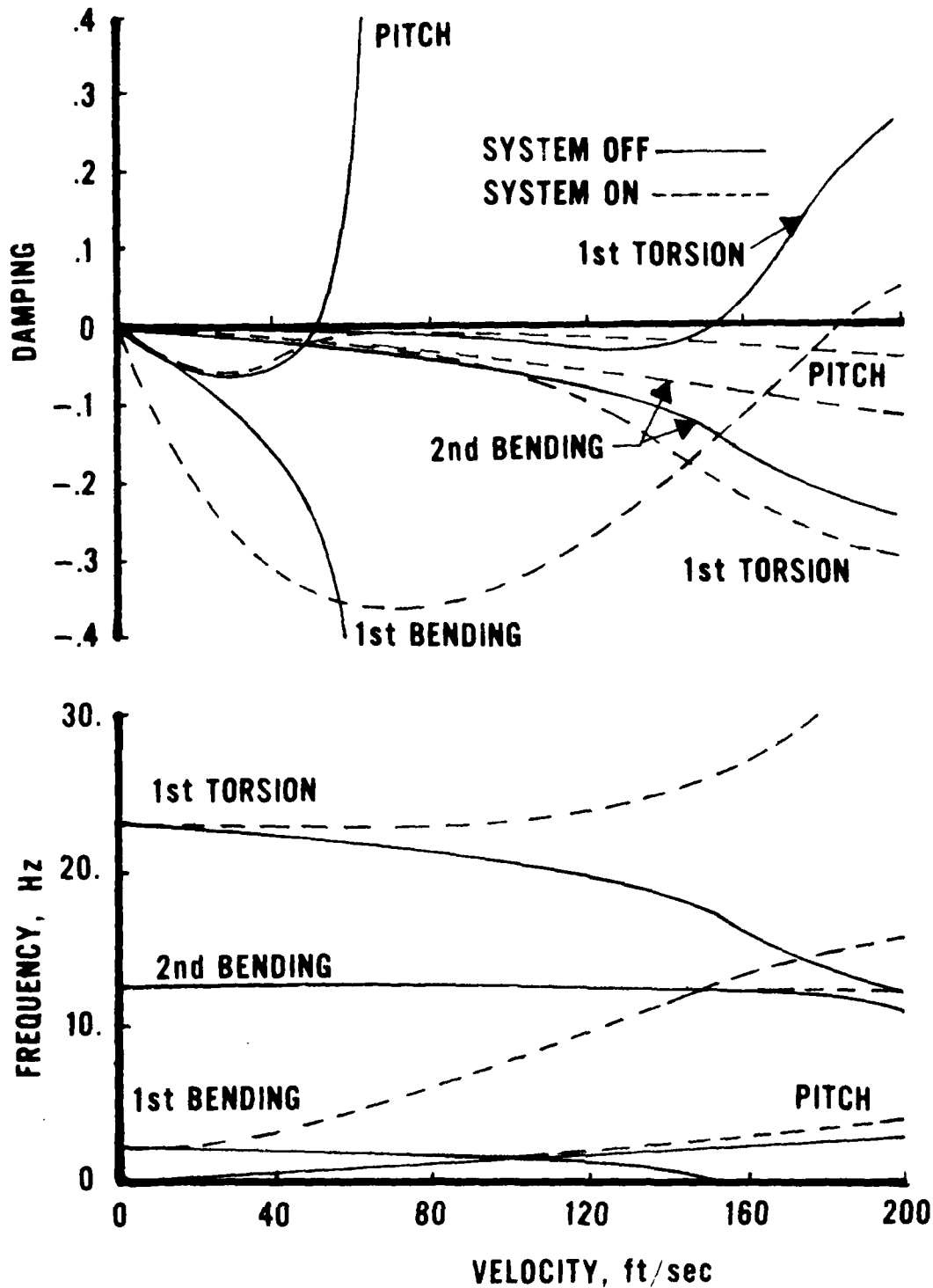
Figure 44   Comparison of V-g and V-ω Plots, Two-Surface Control
System Operating and Off, Model Free in Pitch
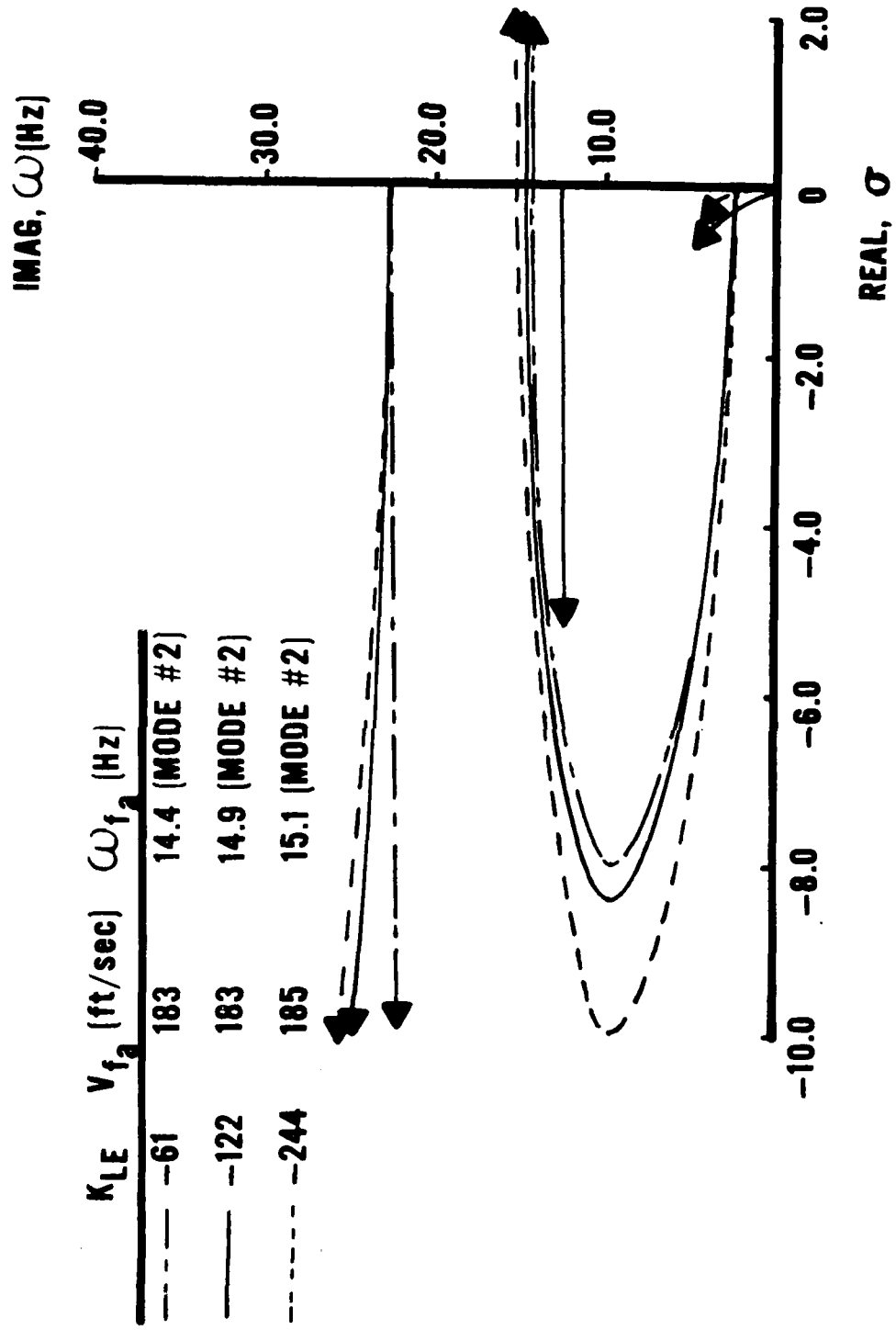
Figure 45   Effect of Leading Edge Gain Variations, Model Free in Pitch (Nominal K_{TE} and ϕ_{TE})

95

mode are affected. The effect is minor and does not cause higher frequency instabilities. This system greatly affects both the rigid pitch mode and the 1st bending mode since it was designed to control the coupling of these modes.

Leading edge gains with absolute values less than 61 deg/in are not sufficient to prevent a hump mode instability involving the rigid pitch mode. The possibility of a hump mode occuring can be seen by noting the shape of the rigid pitch mode in the V-g plot of Figure 44. The behavior of the rigid pitch root (comparing Figures 17 and 43) for gains between 0 and -61 deg/in (from passive to fully augmented) is to swing back to the left hand plane creating the hump mode appearance. The locus crosses the imaginary axis but is still unstable at low to moderate speeds. At a gain near -61 deg/in, the hump is completely in the left hand side of the root locus as shown in Figure 45.

The effect of trailing edge gain variations with K_{LE} and ϕ_{TE} held constant at nominal values for the model free in pitch is illustrated in Figure 46. The bending/torsion flutter characteristics are shown to be fairly sensitive to variations of $\pm$ 6db on K_{TE}. Also as the gain approaches zero, the unstable 1st bending mode gradually approaches V_{fp2}. The switch in the mode of instability from the 1st bending mode to the torsion

96
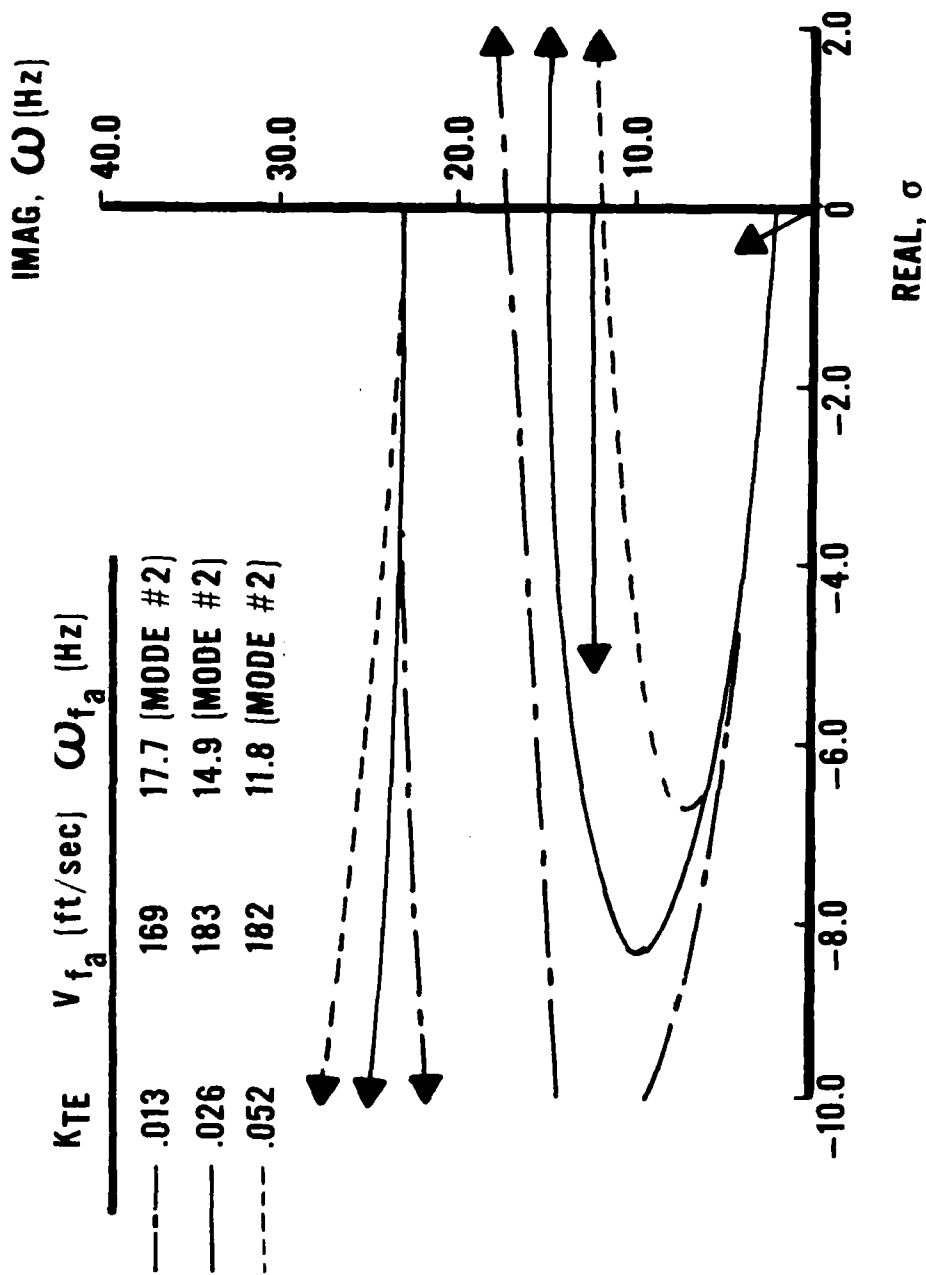
Figure 46 Effect of Trailing Edge Gain Variations, Model Free in Pitch (Nominal K_{LE} and ϕ_{TE})

97

mode is found to be gradual with decreasing K_{TE}. This transition of the mode of instability is better illustrated in a later stability boundary plot (see Figure 49).

Figure 47 illustrates the effect of varying the trailing edge phase lag from nominal while keeping K_{LE} and K_{TE} constant at nominal values. Phase lag angles less than nominal cause the instability speed of the 1st bending mode to drop, while phase lag angles *higher than nominal cause a control* induced instability in the torsion mode at a speed less than V_{fp2}. This interaction with two separate modes of instability causes the phase margins to be quite low for this configuration. Neither ϕ_{TE} nor K_{TE} variations within the range investigated affects the rigid pitch mode or the 2nd bending mode. *This lack of interaction is understandable for the rigid pitch mode since the trailing edge system uses only wing tip angular acceleration feedback.* For the 2nd bending mode, the lack of interaction is probably attributed to the feeding of the system energy into the 1st bending mode which is very near the 2nd bending frequency in the critical velocity range as a result of the closed leading edge loop.

In terms of stability boundaries, the effects of varying the three feedback parameters, separately, from
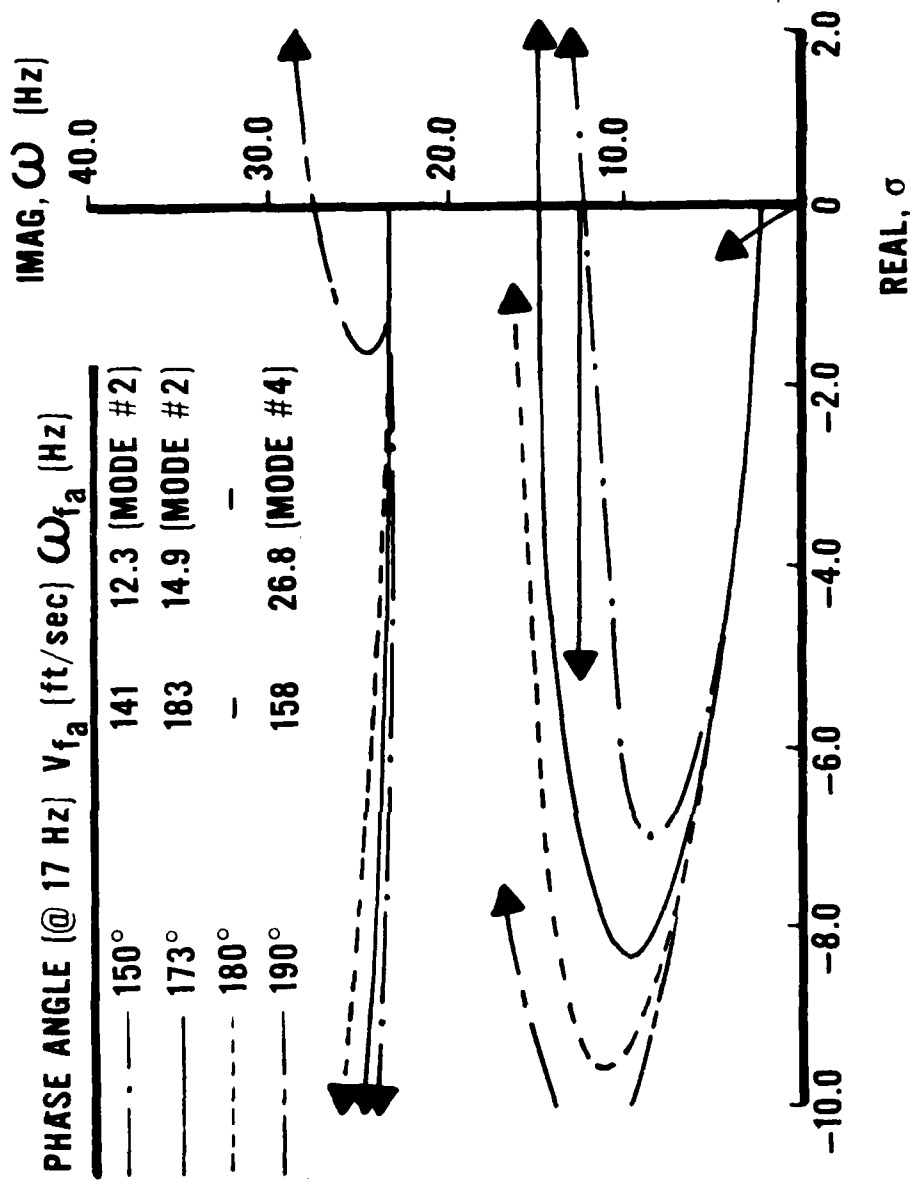
Figure 47 Effect of Trailing Edge Phase Angle Variations, Model Free in Pitch (Nominal K_{LE} and K_{TE})

99

the nominal two-surface control law are presented in Figures 48 to 50. The vertical dashed line in each figure, again, represents the nominal control law. Each figure presents a perturbation of a particular feedback parameter while the other two are held constant at nominal values. These results are similar in terms of the potential instability switching mechanisms possible as is seen for the cantilever wing.

Three forms of mode switching are seen for the model free in pitch. The first form of mode switching is demonstrated in Figure 48. This figure shows the appearance of the low speed hump mode instability involving pitch that becomes stable when the absolute value of K_{LE} is greater than about 61 deg/in causing a switch to a higher speed instability in the 1st elastic mode (mode #2). This figure also shows the positive infinity gain margin on K_{LE}.

The second form involves switching in the origin of the mode of instability and is experienced when K_{TE} is increased. This mechanism is shown in Figure 49. The frequency and shape characteristics of mode #4 are gradually altered to a condition where the instability changes to the characteristics of mode #2. The third type of instability mode switching is encountered when phase lag is varied. This mechanism involves the more classical abrupt change in frequency as shown in Figure

100
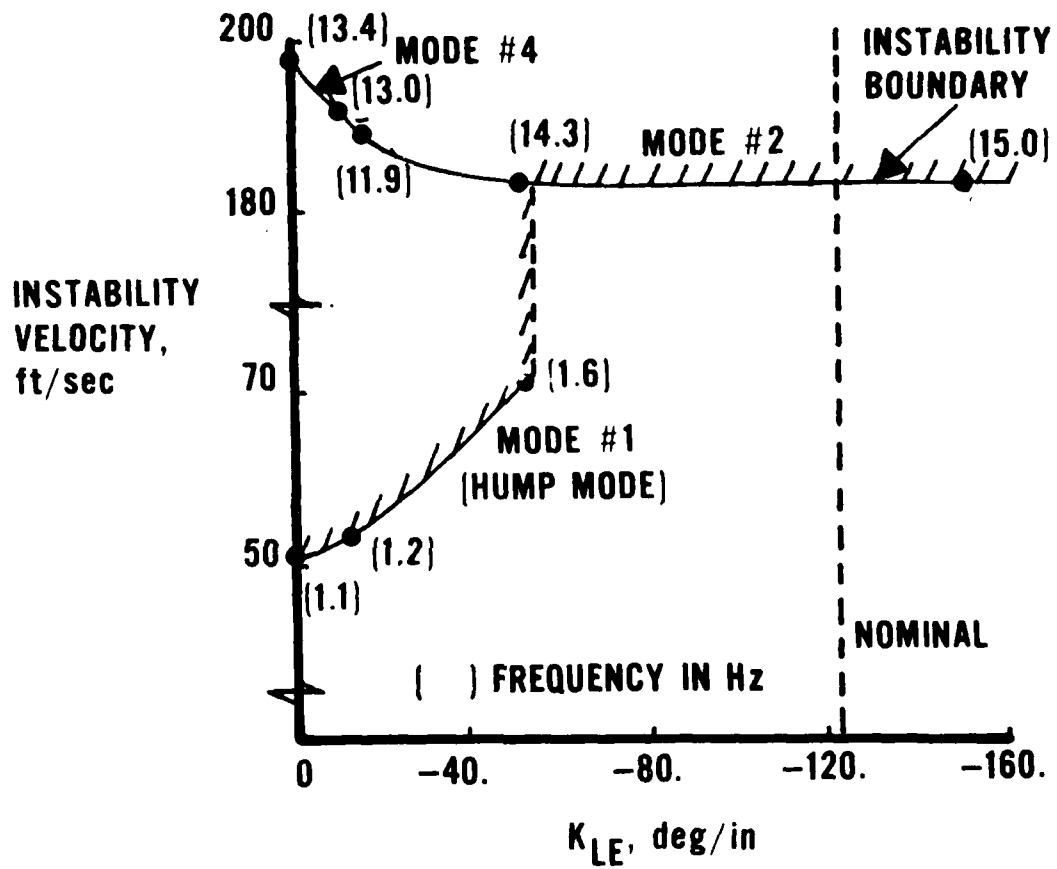
Figure 48 Stability Boundary with Variable K_{LE}, Model Free in Pitch
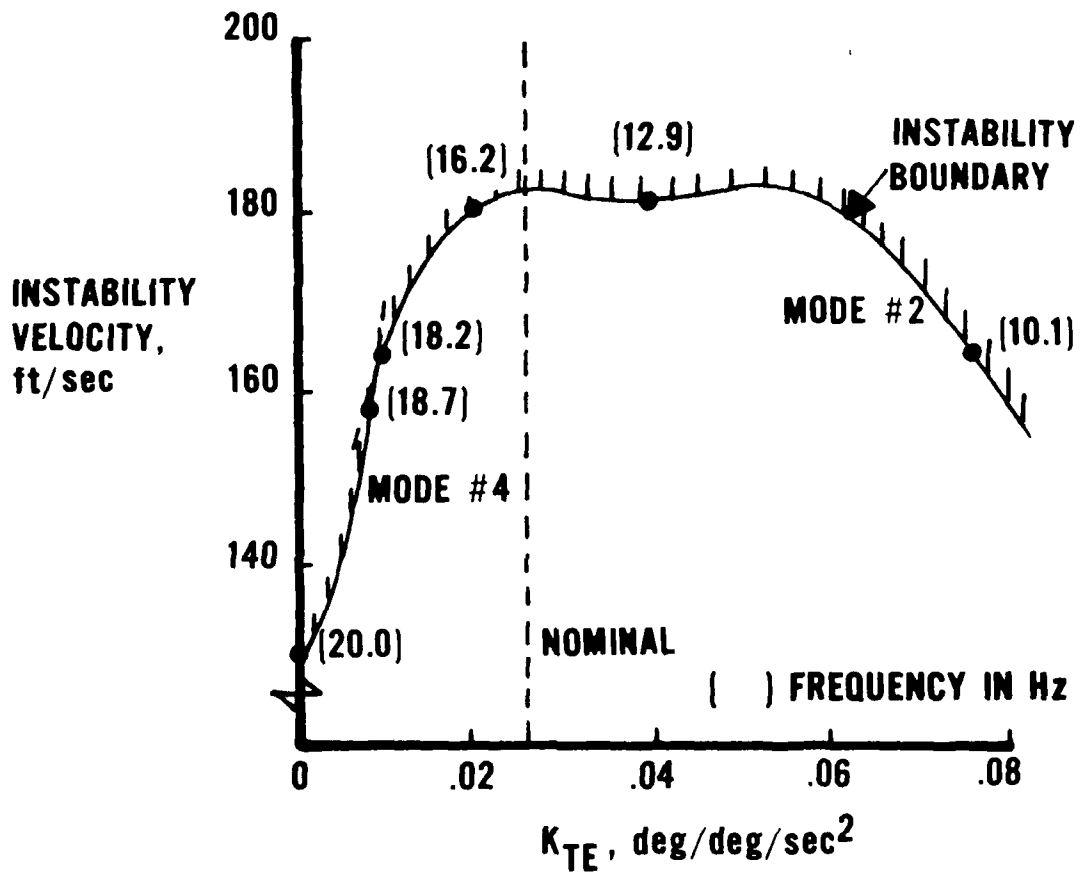
Figure 49   Stability Boundary with Variable K_{TE}, Model Free in Pitch
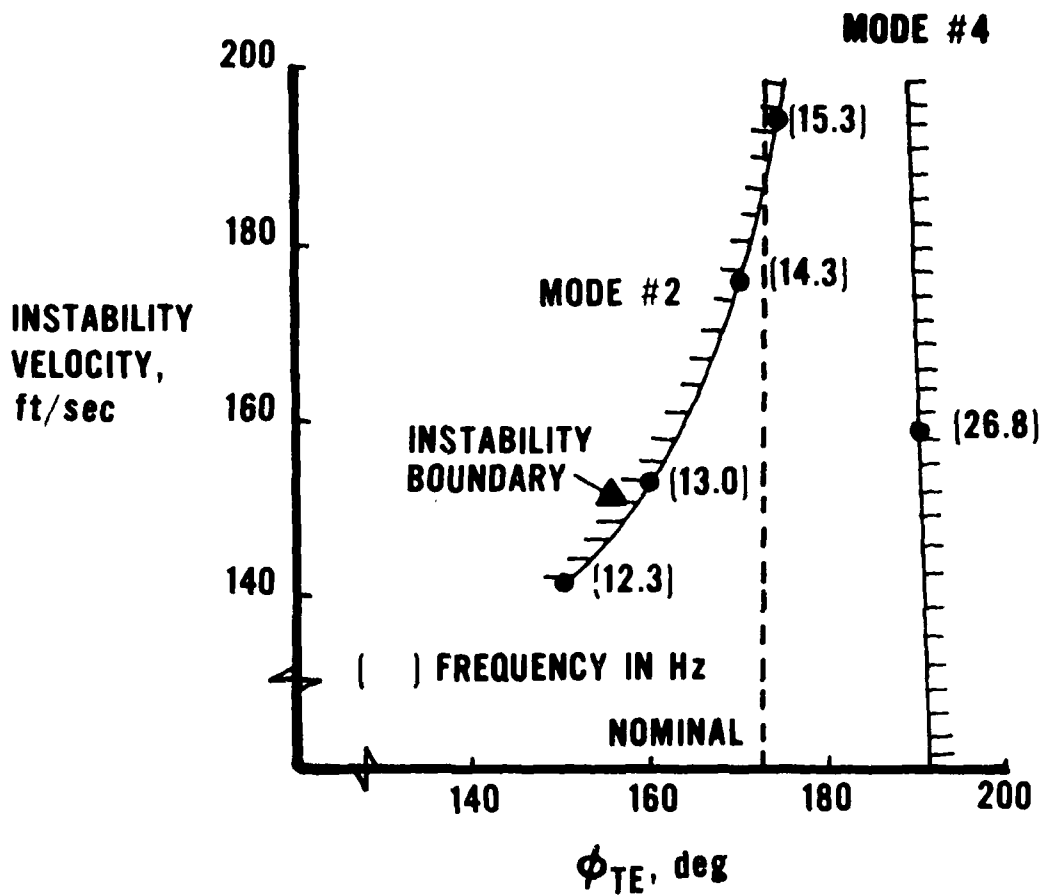
Figure 50 Stability Boundary with Variable ϕ_{TE}, Model Free in Pitch

50. As for the cantilever wing, phase lags slightly greater than 180 degrees cause a rapid drop in an instability speed associated with the torsion mode. The torsion mode is unstable at all speeds for phase lag angles near 190 degrees. This near vertical drop in the stability boundary limits the possible range of phase margins for this configuration and system logic.

Model Free in Pitch and Plunge

Figure 51 presents the closed loop results of the two-surface control law for the model free in pitch and plunge over the velocity range of interest. This control law performs well up to 1.2 V_{fp2} (182 ft/sec). At this speed two simultaneous instabilities are predicted to occur. The higher frequency instability is the bending/torsion flutter mode; the second instability is similar to the control induced instability that occurs in the 1st bending mode when the model is free in pitch only. For this case, however, the control induced instability is found to be a hump mode and is sensitive to changes in the feedback parameters. The flight velocity envelope expansion for this configuration is 153 percent.

Velocity versus frequency and damping plots for the model free in pitch and plunge are shown in Figure 52 for the system operating and off. This figure clearly shows the hump mode present (1st bending) when the
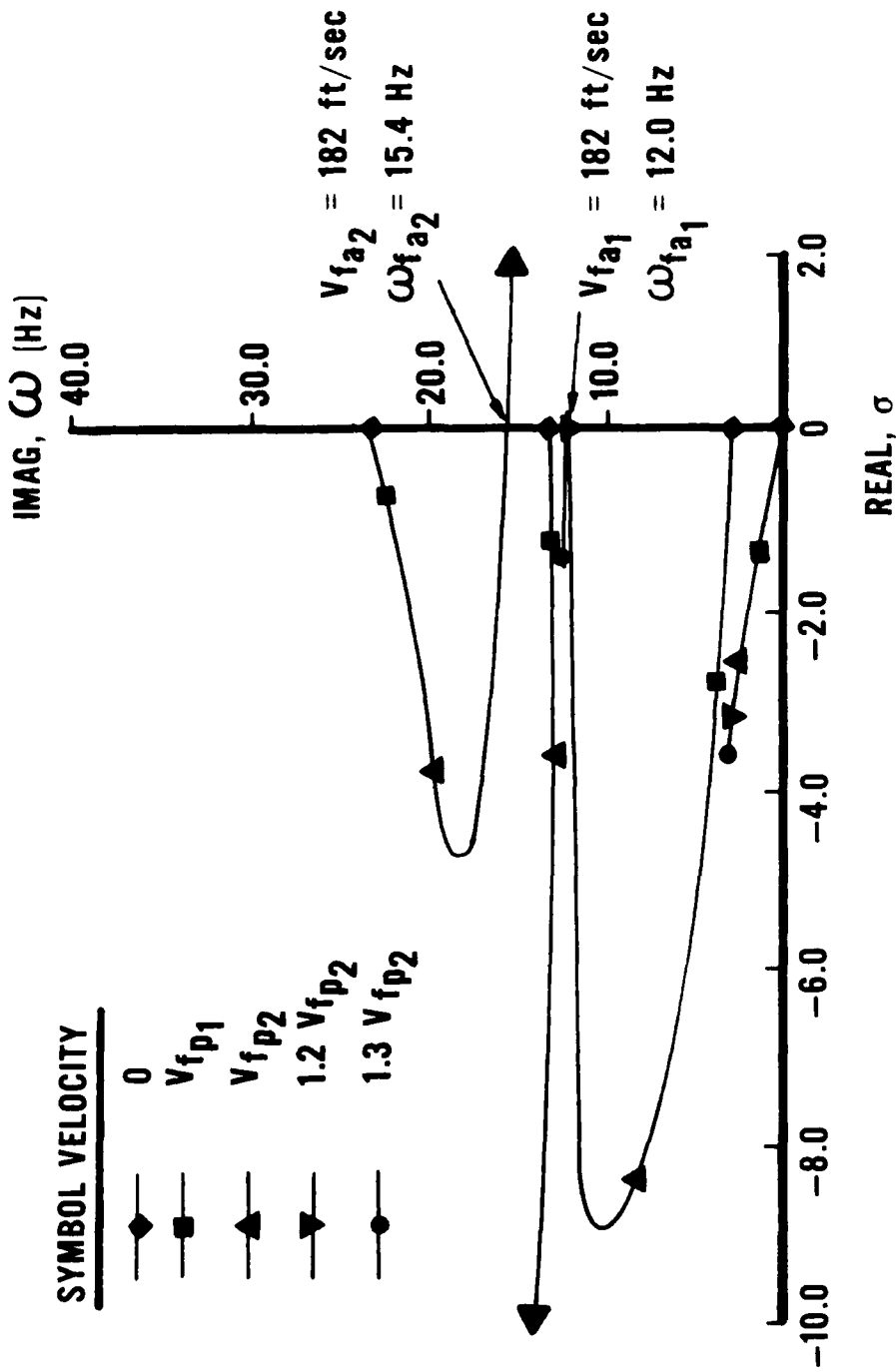
Figure 51 Root Locus for the Model Free in Pitch and Plunge, Nominal Two-Surface Control System
(K_{LE} = -25.2, K_{TE} = .0203, ϕ_{TE} = 175° @ 17 Hz)
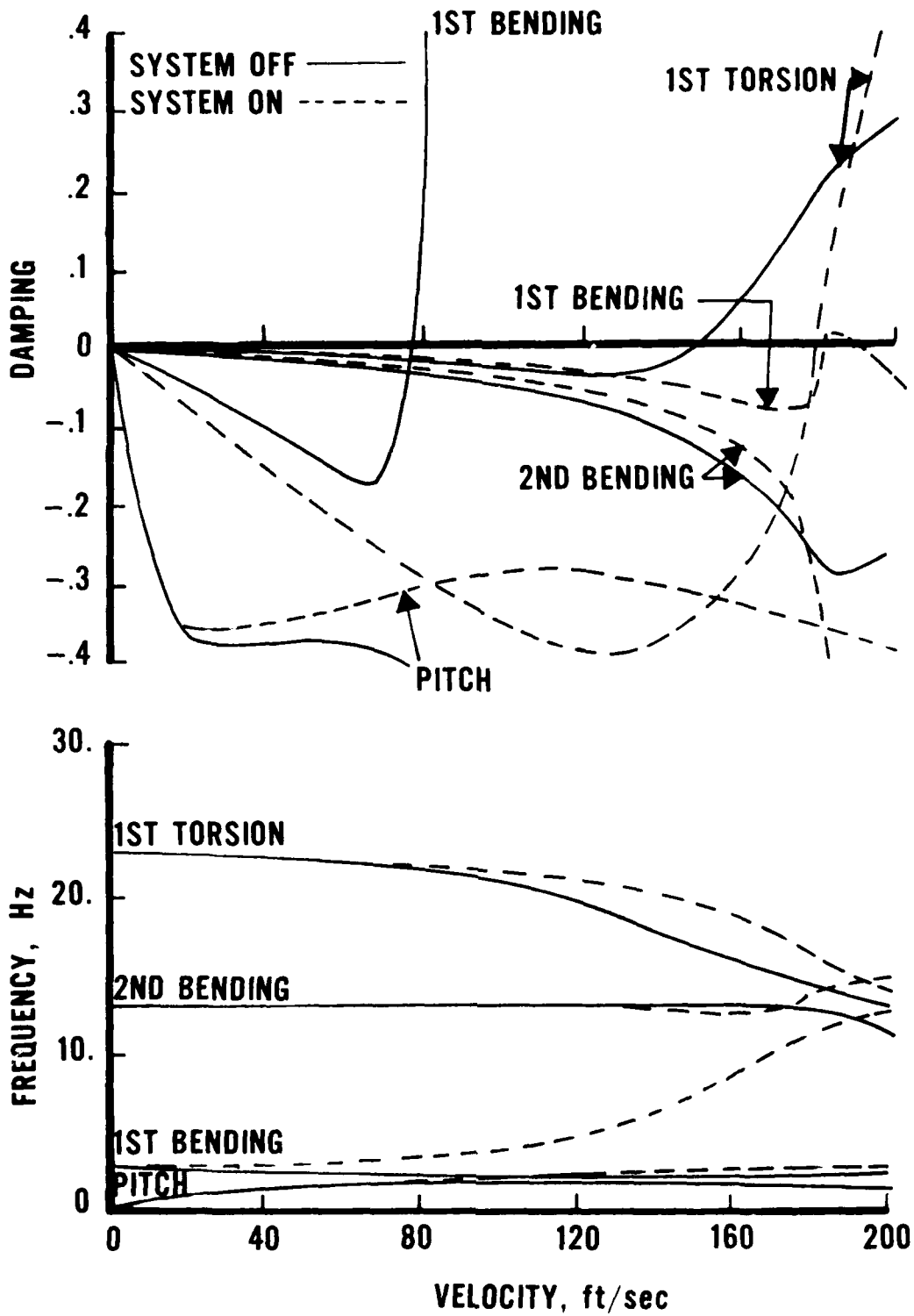
Figure 52   Comparison of V-g and V-ω Plots, Two-Surface Control System
Operating and Off, Model Free in Pitch and Plunge

106

system is operating. The lower figure involving
frequency also shows the significant modal interaction
at high speed. As for the other configurations, this
interaction is a clear indication that mode switching is
likely to occur with changes in the feedback parameters.

Figure 53 presents a velocity root locus plot for
the model free in pitch and plunge that demonstrates the
effects caused by changes in leading edge gain. The
gain variation shown in the figure represents $\pm$ 6db
variations from the nominal condition. The gain range
investigated is shown to interact significantly with all
three of the elastic modes but very little with the
rigid pitch mode. For gains with an absolute value
between zero and about 12.6 deg/in, the unstable 1st
bending mode is brought back to the left hand side
(stable). Further increases in gain add aerodynamic
stiffness to the 1st bending mode causing an instability
to occur near 12 Hz. This instability as described
earlier, involves a hump mode and is later found to be
quite sensitive to changes in the control system
parameters. The effect that K_{LE} has on the 3rd elastic
mode (torsion) is a little different in that the torsion
root changes drastically with increasing K_{LE} but the
instability speed and frequency change only slightly.

The effects of trailing edge gain (K_{TE}) variations
on the model free in pitch and plunge are shown in

107

K_{LE}	V_{fa_1} (ft/sec)	ω_{fa_1} (Hz)	V_{fa_2} (ft/sec)	ω_{fa_2} (Hz)
−·−·− −12.6	—	—	182	15.3 (MODE #5)
———— −25.2	182	12.0 (MODE #3)	182	15.7 (MODE #5)
− − − − −50.4	164	12.0 (MODE #3)	185	15.8 (MODE #4)

IMAG, ω (Hz)

REAL, σ
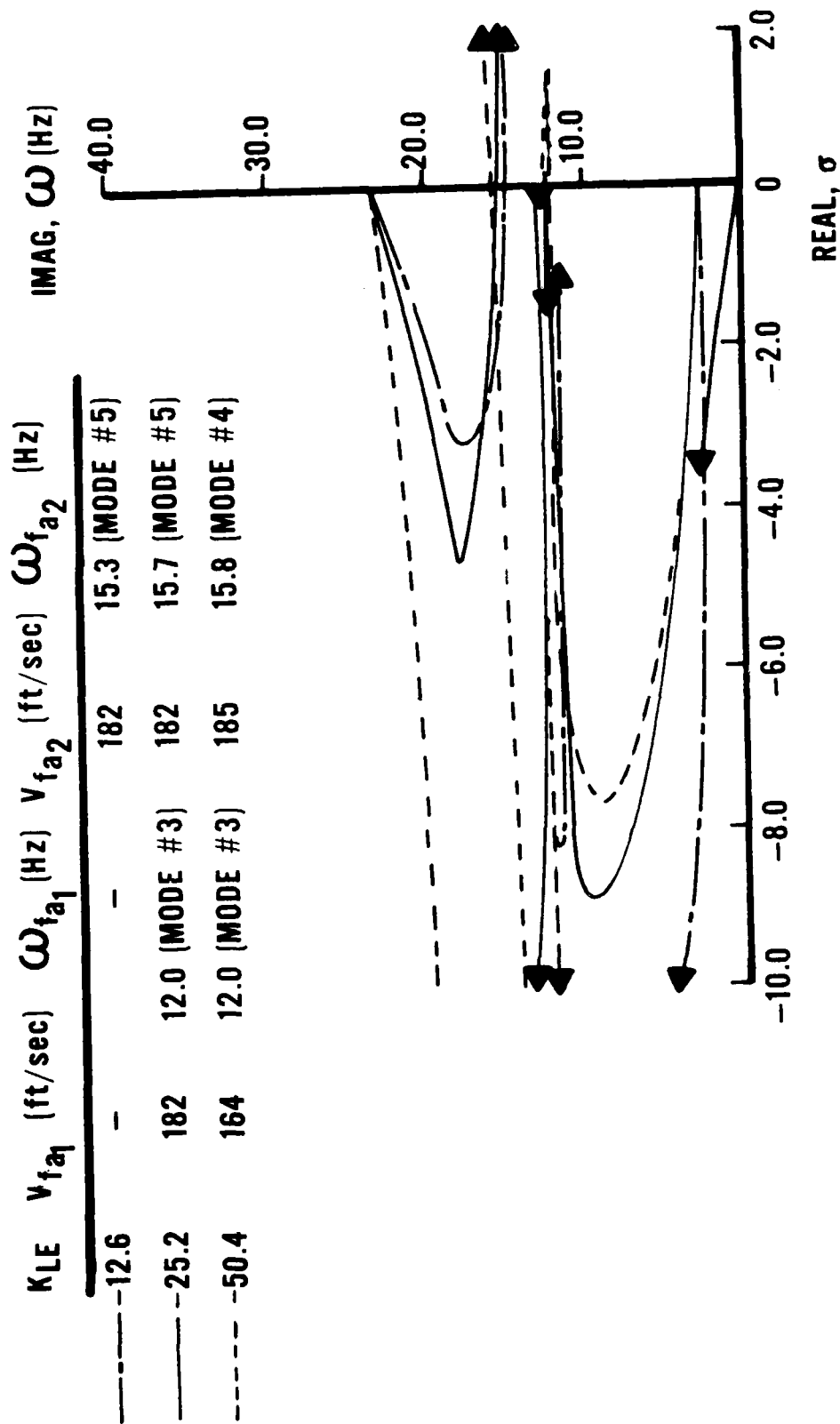
Figure 53 Effect of Leading Edge Gain Variations, Model Free in Pitch and Plunge (Nominal K_{TE} and ϕ_{TE})

108

Figure 54. The trailing edge system not only affects the torsion mode as designed, but also significantly interacts with the 1st bending mode which again is characterized as a hump mode. The plot indicates that there is very little movement of the loci associated with the rigid pitch mode and the 2nd bending mode, indicating an insignificant interaction of these modes with the active system with variations in this feedback gain.

Variations of the trailing edge phase angle from nominal and the effects these have on the root loci of the elastic modes are presented in Figure 55. For this configuration, phase angle variations from the nominal control law affect all three of the elastic modes. All three elastic modes can be driven unstable depending upon the phase lag network used in the system. A high phase angle causes the torsion mode to become unstable at low speeds similar to the other two configurations. A low phase angle causes instabilities in either the 1st bending or 2nd bending modes depending upon the range of the phase angle used.

The stability boundary plots for the three feedback parameters (K_{LE}, K_{TE}, and ϕ_{TE}) are found in Figures 56 through 58. Mode of instability switching is shown to take place similar to that found for the other configurations.
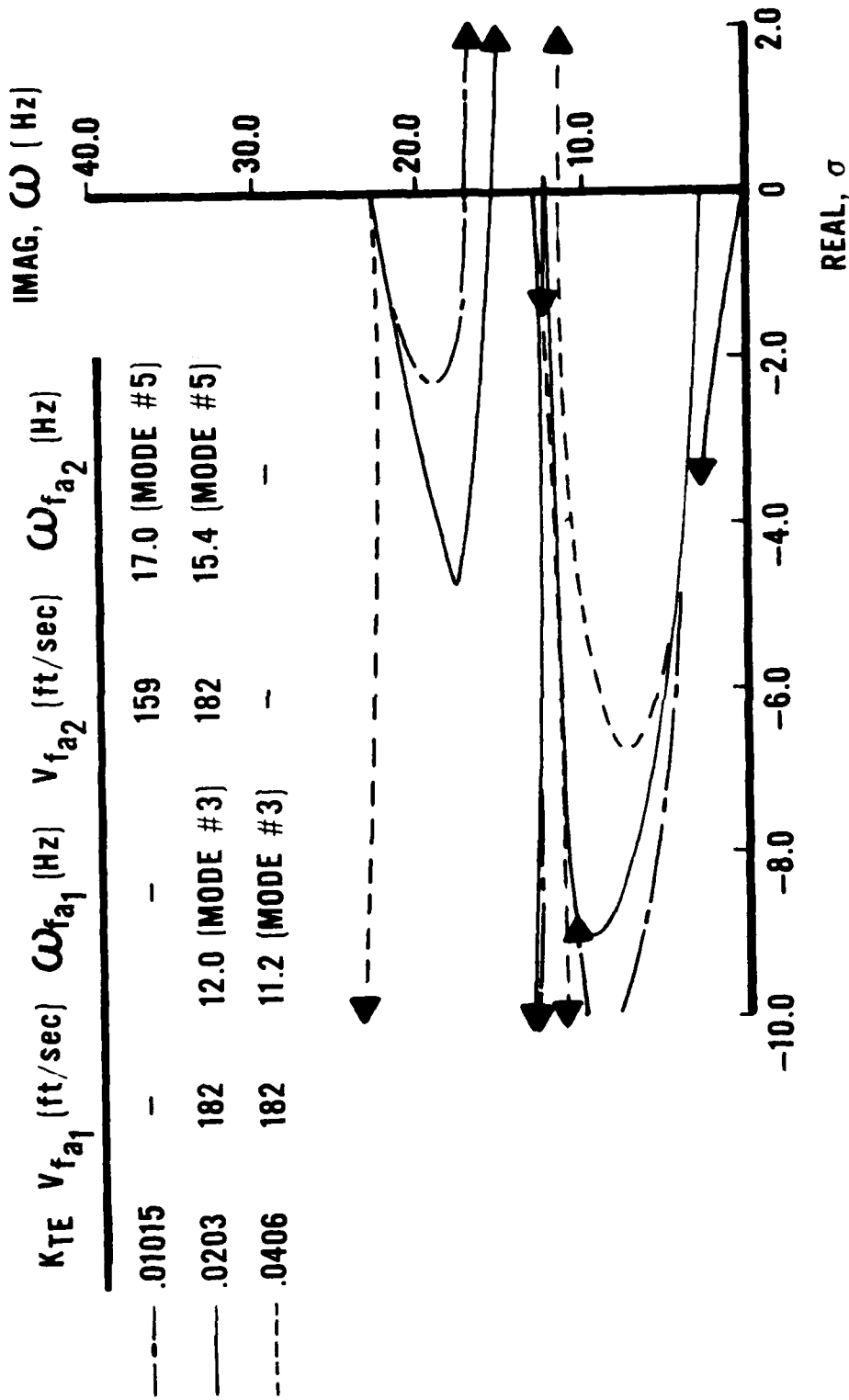
Figure 54   Effect of Trailing Edge Gain Variations, Model Free in
           Pitch and Plunge (Nominal K_{LE} and ϕ_{TE})
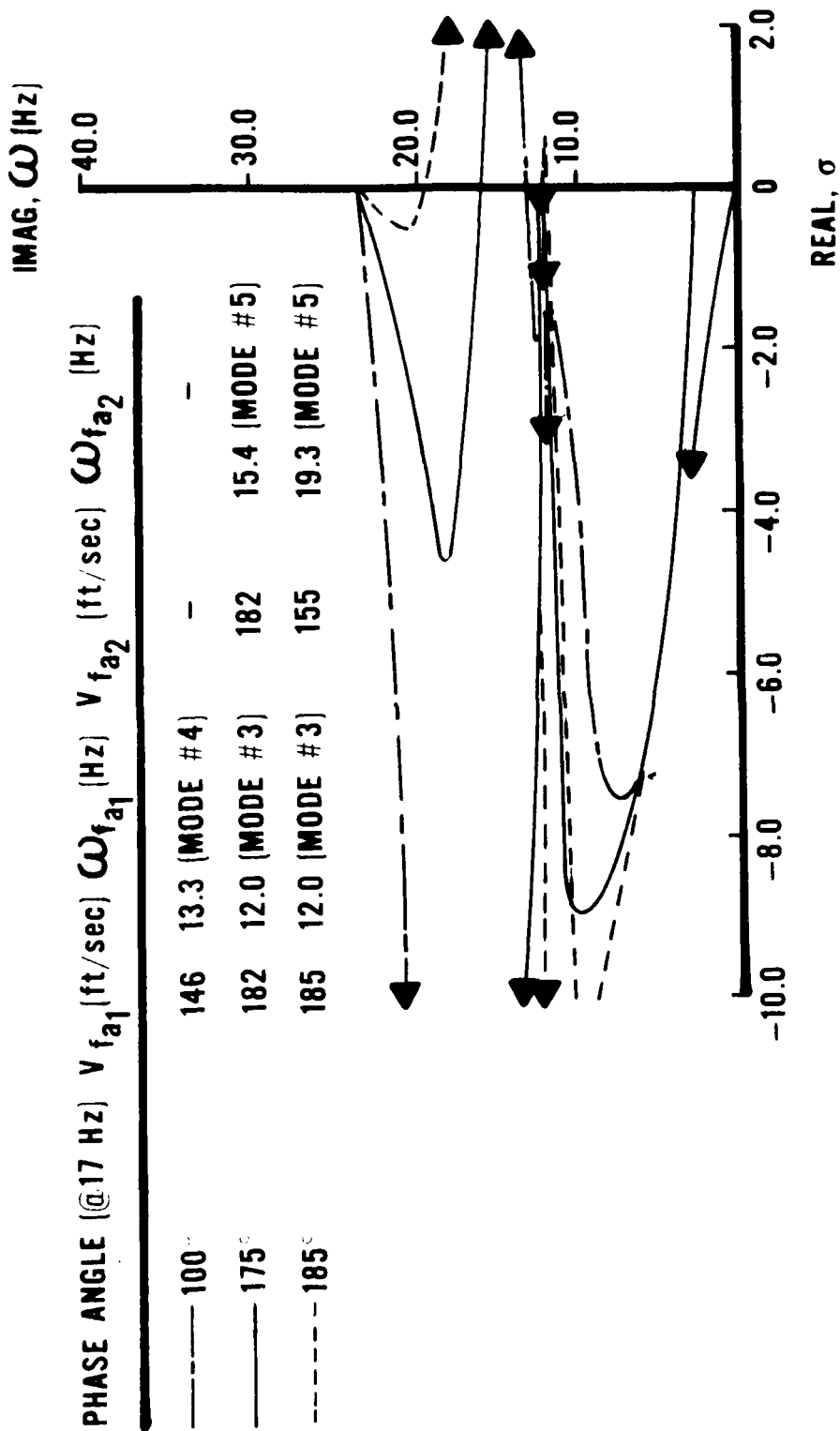
Figure 55   Effects of Trailing Edge Phase Angle Variations, Model Free in Pitch and Plunge (Nominal K_{LE} and K_{TE})
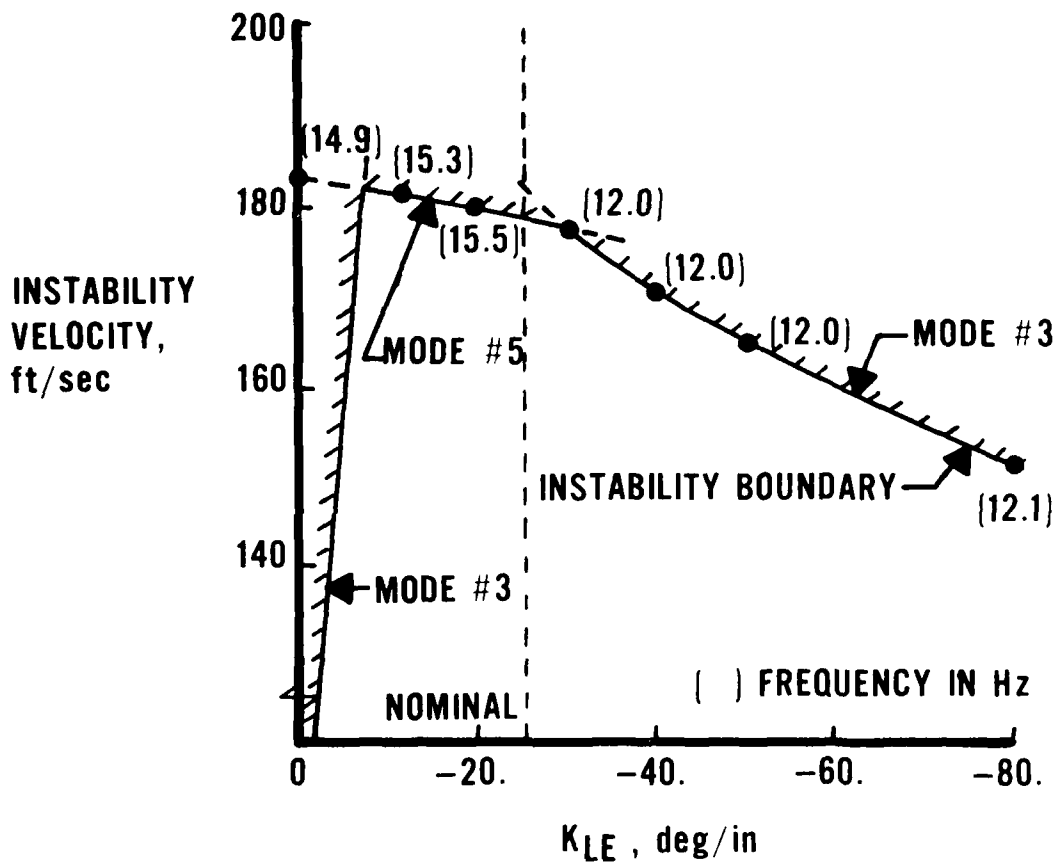
Figure 56 Stability Boundary with Variable K_{LE}, Model Free in Pitch and Plunge
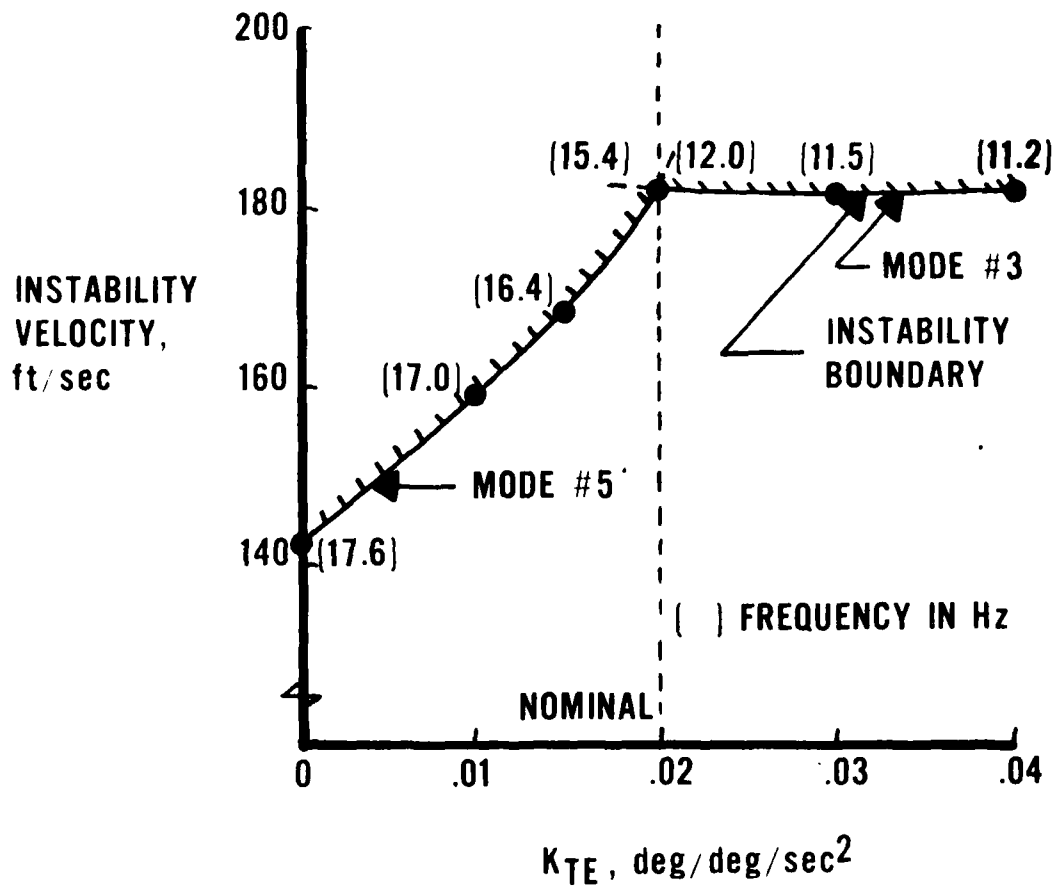
Figure 57 Stability Boundary with Variable K_{TE}, Model Free in Pitch and Plunge
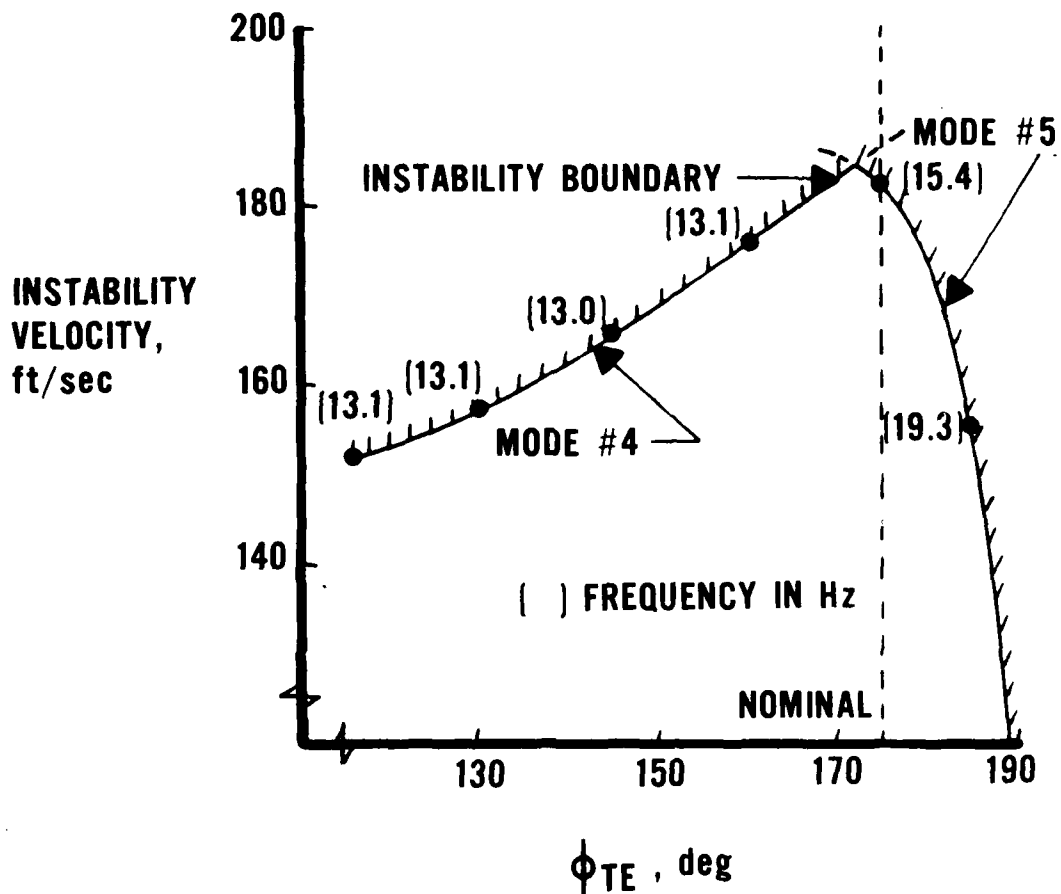
Figure 58 Stability Boundary with Variable ϕ_{TE}, Model Free in Pitch and Plunge

The nominal control law represented as the dashed vertical line intersects the stability boundary of Figure 56 at 182 ft/sec and in mode #5 (torsion). This boundary is positioned at this airspeed by the trailing edge control law (goal of 1.2 V_{fp2}). An increase in gain is shown to cause a classical change in the mode of instability from the torsion mode to the 1st bending mode (mode #3). A decrease in K_{LE} causes body freedom flutter to occur with the instability again occurring in the 1st bending mode.

The determination of the nominal trailing edge gain is quite difficult in that two of the elastic modes are driven unstable near the same airspeed (Figure 57). The highest speed obtainable for this control logic and for this configuration is 182 ft/sec. The nominal control law for this configuration passes through the intersection of the two stability boundaries. The positive gain margin on K_{TE} appears to be infinity; however, at gains near .05, a low speed instability (hump mode) is encountered in the torsion mode.

Figure 58 presents the stability boundaries as a function of the phase angle used in the system (referenced to 17 Hz). This plot indicates, as for the other configurations, that higher phase margins can be obtained by sacrificing speed improvement. It also shows the possibility of the mode of instability

switching as ϕ_{TE} changes.

CHAPTER VI

SUMMARY, CONCLUSIONS AND RECOMMENDATIONS

An active feedback system was designed using several sensors and two active surfaces to suppress the aeroelastic instabilities associated with a forward swept wing aircraft. Objectives of preventing two aeroelastic modes of instability simultaneously using a simple feedback system were accomplished. For a cantilever wing, the static divergence and the wing bending/torsion flutter speeds were increased 20 percent above the latter. This resulted in a 63 percent improvement in the usable velocity flight envelope. Analysis with the active system operating predicted that *for a similar speed increase, body freedom flutter could be increased 252 percent for the model free in pitch and 153 percent for the model free in both pitch and plunge.*

Summary

A summary of the analyses are provided below.

1. The unsteady aerodynamic force coefficients were approximated using low order Pade' polynomials. Passive calculations using the Pade' approximations of the aerodynamic forces and a root locus analysis procedure predicted flutter characteristics that agreed very well with conventional flutter prediction

techniques. It was concluded that low order Pade'
polynomials accurately fit the unsteady aerodynamic
force coefficients in the low subsonic speed range.

2. The active system for each wing boundary
condition consisted of two active surfaces located at
about the wing 3/4 span. A leading edge surface was
commanded by a displacement sensor positioned near the
intersection of the wing 2nd bending and the wing
torsion node lines. This location provided the best
position for minimizing inputs from these modes while
providing adequate response in the 1st bending mode.
When the model was free to pitch or pitch and plunge,
the translations at the displacement sensor due to rigid
aircraft rotation and plunge, were subtracted from the
signal. The second loop consisted of a trailing edge
control surface commanded by angular acceleration. This
sensor was positioned near the wing tip to maximize the
torsion input signal. Angle of twist was employed to
minimize feedback from the lower bending modes.

3. The leading edge system was specifically
designed to suppress the divergence tendencies of the
wing. This included static divergence of the cantilever
wing and body freedom flutter of the model when free in
pitch or free in both pitch and plunge. The trailing
edge system was designed to suppress the high frequency

118

bending/torsion flutter mode encountered with all wing
boundary conditions.

4. Variations of the feedback parameters from the
nominal values caused changes in the mode of
instability. These changes in the mode of instability
were either classical mode switching (abrupt changes in
frequency) or a transition from one mode to another
(continuous frequency variation).

5. Gain margins of ± 6db were not difficult to
obtain for any of the wing boundary conditions
investigated. Phase margins of ± 45 degrees could not
be obtained without more complicated control laws.
Analyses indicated that phase margins could be increased
by trading speed improvement.

6. The divergence system (leading edge system) did
not significantly interact with the flutter instability.
Also, the flutter suppression system (trailing edge
system) did not affect the divergence instability. For
both cases, the lack of interaction was attributed to
the frequency separation of the two modes of instability
and the sensors being fed back. Both systems, however,
significantly affected the 2nd bending mode.

Conclusions

The studies reported herein have established the
feasibility of applying active feedback control systems
for preventing the aeroelastic instabilities associated

with forward swept wings. The application of the concept for aeroelastic control is an efficient, adaptable, low weight approach compared to the classical techniques of adding weight, stiffening the wings, or imposing aircraft speed placards. The classical approaches for flutter and divergence prevention have historically resulted in a loss in aircraft performance and survivability. With the advent of high-gain digital/adaptive flight control systems, it is easily conceivable that the flutter and divergence control systems could become integral parts of the flight control system using common components designed for reliability and redundancy.

It is speculated that an active system for aeroelastic control would be most beneficial when one considers damaged composite wings resulting in a loss of stiffness, or the external store carriage issue that causes many flutter problems. It is expected that a forward swept wing aircraft will evolve in terms of operational deployment similar to what has occurred in the past on such aft swept wing aircraft as the F-4, the F-5, the A-7 and the F-111. The use of external stores by these vehicles have, for practical purposes, grown unbounded with time. Historically, fighter aircraft are designed for a primary mission involving air-to-air combat and are later used in off-design missions that

involve a certain number of external stores for air-to-ground combat. Later in the life of the aircraft, air-to-ground becomes an important mission to the operational commanders requiring even more store configurations. Aeroelastic problems are found to be critical as a result of the many new external stores required for carriage. These new stores result in thousands of possible take-off and downloadings, many of which are flutter critical. An adaptive control system, a logical extension of the concept studied, offers significant promise for the external store flutter issue.

It is expected that an active control system will be initially used to obtain aeroelastic instability margins of safety (15 percent above the aircraft maximum speed as required by Military Specs). The system in this case will be operating at speeds near the aircraft maximum speed but the vehicle will never be operating at a passively unstable flight condition. As more confidence is developed for such a system, it will be used to prevent aeroelastic problems that are occuring deep within the flight envelope of the vehicle (external store flutter problem). Large payoffs in terms of aircraft performance and survivability are expected as a result of this application.

This study defined the usefulness of active control

121

systems for controlling aeroelastic instabilities
associated with forward swept wing aircraft. It is
important now that this work continue so that practical
systems can be developed, fabricated and tested in the
wind tunnel to verify these feasibility analyses. The
results of this study warrant continued research in this
technical discipline.

Recommendations

As a result of these and other active flutter
suppression and divergence analyses on cantilever wings
and wings with rigid modes, the tools of design appear
to be available. However, there are several important
analytical and experimental aspects related to this
subject that require additional investigation. From an
analytical viewpoint, the effects of Mach number and
dynamic pressure should be evaluated to form sensitivity
trends. Furthermore, variables such as static margin
and forward sweep angle should be addressed. These
sensitivity trends may define the need for adaptive
control laws for variable flight conditions in addition
to the need of such a system for external store
applications. Regarding aerodynamics, the effects of
nonlinearities in the transonic flow region neeu to be
evaluated. Also, alternate design procedures involving
the time domain need to be further developed to evaluate
these nonlinearities.

There is currently a need and a desire to demonstrate through wind tunnel tests, the suppression of divergence on a cantilever wing using displacement feedback. Evaluations of the effects of symmetric rigid body modes such as rigid pitch and plunge on the suppression of body freedom flutter should also be seriously considered using wind tunnel models.

Analyses and wind tunnel tests also need to be conducted to evaluate the antisymmetric rigid and elastic modes of a forward swept wing to determine if other unexpected aeroelastic instabilities are not hidden in the shadows of simplifying assumptions. Finally, free-flying wind tunnel models incorporating all six rigid body degrees of freedom need to be used to investigate the feasibility and practicality of active aeroelastic control systems.

REFERENCES

1. Knight, M., and Noyes, R., "Span Load Distribution as a Factor in Stability in Roll", NACA Report No. 393, 1931.

2. Jones, R. T., "Notes on the Stability and Control of Tailless Airplanes", NACA TN 837, Dec 1941.

3. Diederick, F. W., and Budiansky, B., "Divergence of Swept Wings", NACA TN 1680, 1948.

4. Krone, N., "Divergence Elimination with Advanced Composites", AIAA Aircraft Systems and Technology Meeting, Los Angeles, California, Aug 1975.

5. Triplett, W. E., "Aeroelastic Tailoring of a Forward Swept Wing and Comparisons with Three Equivalent Aft Swept Wings", AIAA 21st SDM Conf., Seattle, WA, May 1980.

6. Weisshaar, T. A., "The Influence of Aeroelasticity on Swept Composite Wings", AFWAL-TR-80-3137, Nov 1980.

7. Sherrer, V. C., Hertz, T. J., and Shirk, M. H., "Wind Tunnel Demonstration of the Principle of Aeroelastic Tailoring Applied to Forward Swept Wings", AIAA 21st SDM Conf., Seattle, WA, May 1980.

8. Wilkinson, K., and Rauch, F., "Predicted and Measured Divergence Speeds of an Advanced Composite Forward Swept Wing Model", AFWAL-TR-80-3059, July 1980.

9. Ellis, J. W., Dobbs, S. K., and Miller, G. D., "Structural Design and Wind Tunnel Testing of a Forward Swept Fighter Wing", AFWAL-TR-80-3073, July 1980.

10. Miller, G. D., Wykes, J. H., and Brosnan, M. J., "Rigid Body-Structural Mode Coupling on a Forward Swept Wing Aircraft", Paper No. 82-0683, New Orleans, LA, May 1982.

11. Weisshaar, T. A., "Divergence Suppression of Forward Swept Wings", Final Report NASA Grant, NASI-15080-Task 16, Virginia Polytechnic Institute and State University, Sep 1980.

12. Weisshaar, T. A., Zeiler, T. A., Hertz, T. J., and Shirk, M. H., "Flutter of Forward Swept Wings, Analysis and Test", paper presented at the 23rd AIAA SDM Conference, New Orleans, LA, Apr 1982.

13. Gaukroger, D. P., "Wind Tunnel Flutter Tests on Model Delta Wing under Fixed and Free-Root Conditions", British A.R.C., R&M 2826, 1955.

14. Cunningham, H. J., and Lundstrom, R. R., "Description and Analysis of a Rocket-Vehicle Experiment on Flutter Involving Wing Deformation and Body Motions", NACA TN-3311, Jan 1955.

15. Griffin, K. E., and Eastep, F. E., "Active Control of Forward Swept Wings with Divergence and Flutter Aeroelastic Instabilities", AIAA Paper No. 81-0637, Atlanta, GA, Apr 1981.

16. Chipman, R. R., Zislin, A. M., and Waters, C., "Active Control of Aeroelastic Divergence", Paper No. 82-0684, New Orleans, LA, May 1982.

17. Giesing, J. P., Kalman, T. P., and Rodden, W. P., "Subsonic Unsteady Aerodynamics for General Configurations", AFFDL-TR-75-5 Part I, Vols I and II, Nov 1971.

18. Baker, G. A., "Essentials of Pade' Approximates", Academic Press, 1975.

19. Vepa, R., "On the Use of Pade' Approximates to Represent Unsteady Aerodynamic Loads for Arbitrary Small Motions of Wings", AIAA Paper No. 76-17, Jan 1976.

20. The NASTRAN User's Manual, (Level 17.0), NASA SP-222 (04), National Aeronautics and Space Administration, Dec 1979.

21. "FASTOP-3: A Strength, Deflection and Flutter Optimization Program for Metallic and Composite Structures", AFFDL-TR-78-50, Vol. II, May 1978.

22. Pendleton, E. W., "Vibration Testing Results of a
    Forward Swept Wing Model with Fuselage Pitch
    Freedom", AFWAL-TM-82-178-FIBRC, May 1982.

126

APPENDIX A

SELECTION OF A FORWARD SWEPT WING CONFIGURATION

A forward swept wing wind tunnel model previously tested to investigate divergence and body freedom flutter was selected as the basis of the configuration and dynamic characteristics desired for use in this study. The planform of the model with key dimensions of the wing and fuselage bar assembly are provided in Figure 2 of the main text.

Finite Element Representation

To obtain the calculated natural frequencies and node lines for each of the important vibration modes of the wind tunnel model, finite element techniques were used. In the following, any reference to "plate" concerns the aluminum load carrying member of the wing; any reference to "model" concerns the entire wing (plate, sleeve and fuselage). Also, the "basic wing" represents the wind tunnel model, while "modified wing" includes one pound of weight distributed along the outboard six sections of the wind tunnel model near the trailing edge of the wing.

The plate was represented by 18 finite beam elements and the hollow steel fuselage bar was represented with 6 elements. Figure A-1 shows the
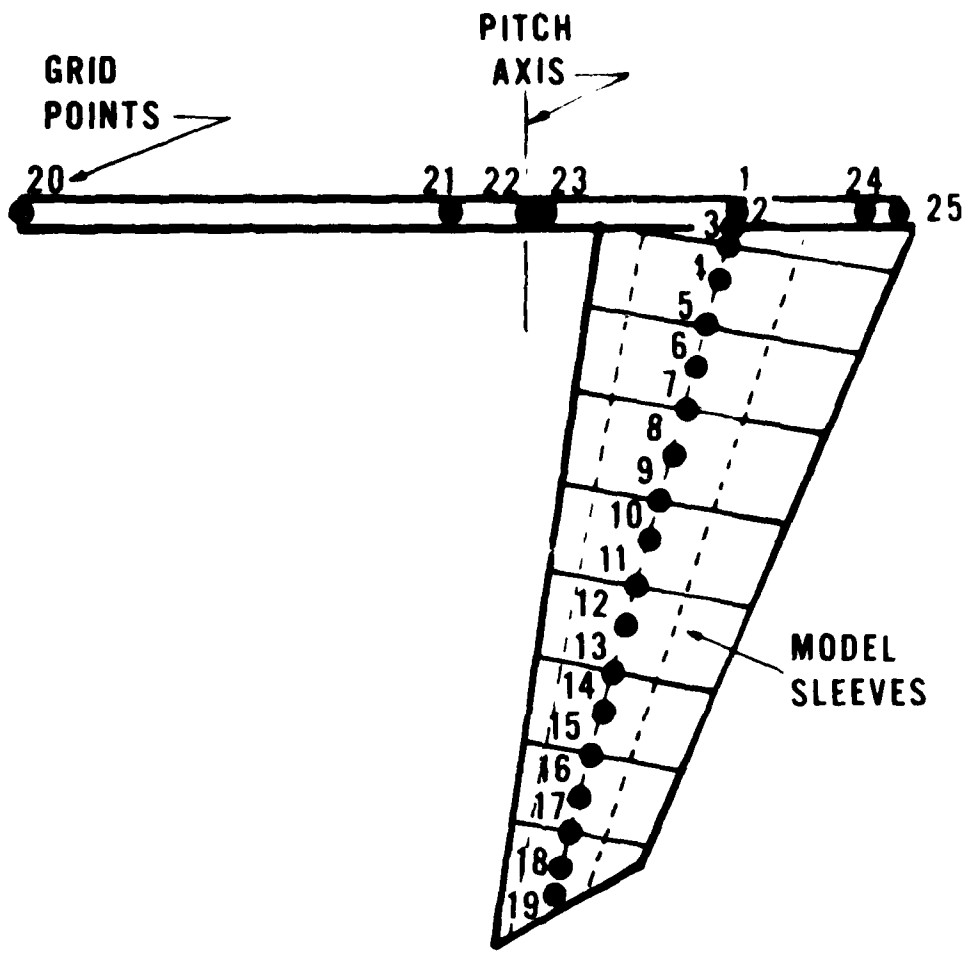
Figure A-1   Beam Finite Element Grid Points

128

relative locations of the grid points for this representation, and Table A-1 presents the global coordinates of the grid points. The origin of the global coordinate system used in the analyses was located at grid point #1 with x positive aft along the bar and y positive out the span of the wing (z + down). A second coordinate system with the origin located at grid point #1 but rotated 15 degrees forward such that the y-direction was along the reference axis (elastic axis) was also used in the analysis. This system located the masses and inertias of the plate and sleeves in a dumbbell sense about the elastic axis of the model. Again, the x-direction was positive aft. The dumbbell moment arms were determined using the mass (m), the mass moment of inertia (I_α), and the static unbalance (e) of each section and the equations,

$$d_1 = \sqrt{\frac{I_\alpha}{m} - e^2} + e \qquad\qquad (1)$$

$$d_2 = \sqrt{\frac{I_\alpha}{m} - e^2} - e \qquad\qquad (2)$$

Table A-2 provides the value of the mass located at each grid point used in the analysis and identifies the masses as coming from the plate, the sleeves, the bar or the flutter weights (if applicable). The masses on the wing are offset from the reference axis at each grid point by the dumbbell distances provided in Table A-3.

129

Table A-1   Finite Element Grid Point Coordinates

| GRID PT | COORDINATES (IN) | |
	X	Y
1	0.	0.
2	-.17	.65
3	-.43	1.60
4	-.76	2.85
5	-1.45	5.40
6	-1.92	7.15
7	-2.48	9.25
8	-2.96	11.05
9	-3.52	13.15
10	-3.98	14.85
11	-4.58	17.10
12	-5.05	18.85
13	-5.63	21.00
14	-6.08	22.70
15	-6.66	24.85
16	-7.11	26.55
17	-7.58	28.30
18	-8.01	29.90
19	-8.32	31.06
20	-32.50	0.
21	-12.50	0.
22	-9.46	0.
23	-8.50	0.
24	6.00	0.
25	7.50	0.

Table A-2   Finite Element Grid Point Masses

GRID PT	MASS (LBM)			
	PLATE	SLEEVE	BAR	FLUTTER WGTS
1	.0230	-	1.2364	-
2	.0569	-	-	-
3	.0776	-	-	-
4	.1289	.2710	-	-
5	.1411	-	-	-
6	.1200	.2403	-	-
7	.1166	-	-	-
8	.1106	.2077	-	.1667
9	.1031	-	-	-
10	.1007	.1821	-	.1667
11	.0973	-	-	-
12	.0894	.1557	-	.1667
13	.0832	-	-	-
14	.0764	.1299	-	.1667
15	.0716	-	-	-
16	.0594	.0931	-	.1667
17	.0538	-	-	-
18	.0414	.0788	-	.1667
19	.0167	-	-	-
20	-	-	1.7054	-
21	-	-	1.9644	-
22	-	-	.3341	-
23	-	-	.9828	-
24	-	-	.8153	-
25	-	-	.1279	-

Table A-3 Moment Arms for Wing Inertia Using a Dumbbell Representation

GRID PT	DISTANCES[2] (IN)		
	PLATE[1]	SLEEVE[1]	FLUTTER WGTS
1	±1.809	-	-
2	±1.817	-	-
3	±1.799	-	-
4	±1.733	3.972, -2.512	-
5	±2.257	-	-
6	±2.286	3.469, -2.739	-
7	±1.528	-	-
8	±1.450	3.226, -2.468	5.5
9	±1.385	-	-
10	±1.304	3.017, -2.173	5.0
11	±1.243	-	-
12	±1.163	2.752, -1.958	4.5
13	±1.095	-	-
14	±1.016	2.479, -1.681	4.0
15	±.953	-	-
16	±.882	2.221, -1.495	3.0
17	±.820	-	-
18	±.765	1.592, -1.544	1.0
19	±.737	-	-

Notes:

1. Half of the Mass at each location

2. Perpendicular to reference axis at grid point

The calculated center of mass for the basic model was only 1/4-inch off from the measured value for the configuration selected.

Vibration Analysis

An analysis was conducted to obtain the frequencies and node lines of the first three normal modes of vibration (1st bending, 2nd bending, and 1st torsion) of the wind tunnel model. This analysis was necessary to provide the confidence required to assure that the finite element model accurately represented the wind tunnel model. Good correlation with ground vibration test data[22] provided that confidence. The analysis was conducted for both the plate and the basic model cantilevered and free in pitch. The frequencies of the first three modes are summarized in Table 1 of the main text. Analyses were also conducted for the basic model free in pitch and plunge, although no test data were available for correlation. Node lines and the frequencies (calculated and test, where applicable) for three modes for the three wing boundary conditions are provided in Figures A-2 thru A-4.

Once good correlation was obtained with experimental results, the basic model was modified by adding mass along the trailing edge of the wing to lower the bending/torsion flutter speed. A vibration analysis was conducted in parallel with a flutter/divergence
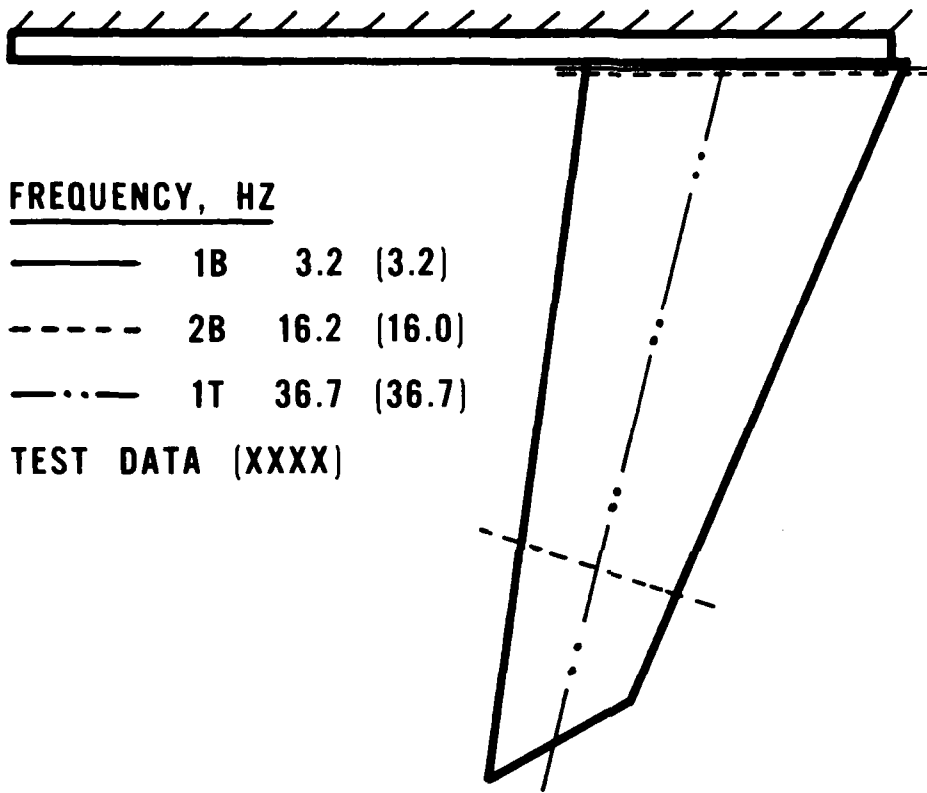
FREQUENCY, HZ

——————— 1B   3.2 (3.2)

— — — — — 2B   16.2 (16.0)

—··—   1T   36.7 (36.7)

TEST DATA (XXXX)

Figure A-2 Calculated Frequencies and Node Lines of
Basic Cantilever Model

FREQUENCY, HZ

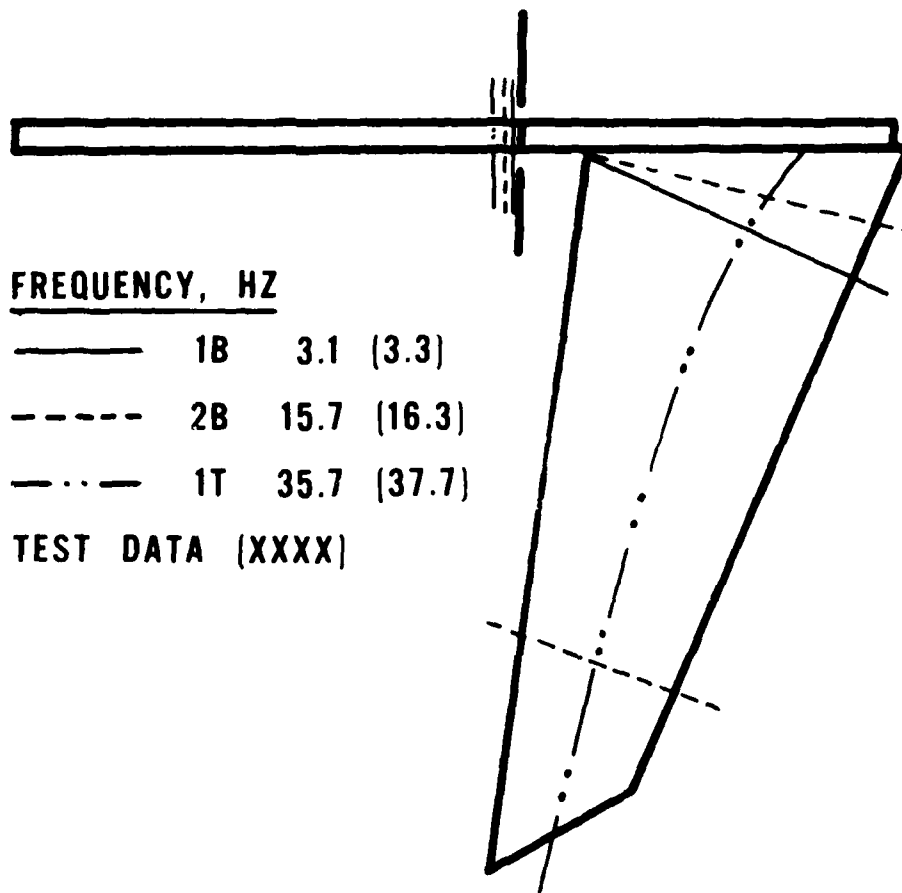|		
————	1B	3.1 (3.3)
— — — —	2B	15.7 (16.3)
— ·· —	1T	35.7 (37.7)

TEST DATA (XXXX)

Figure A-3 Calculated Frequencies and Node Lines of
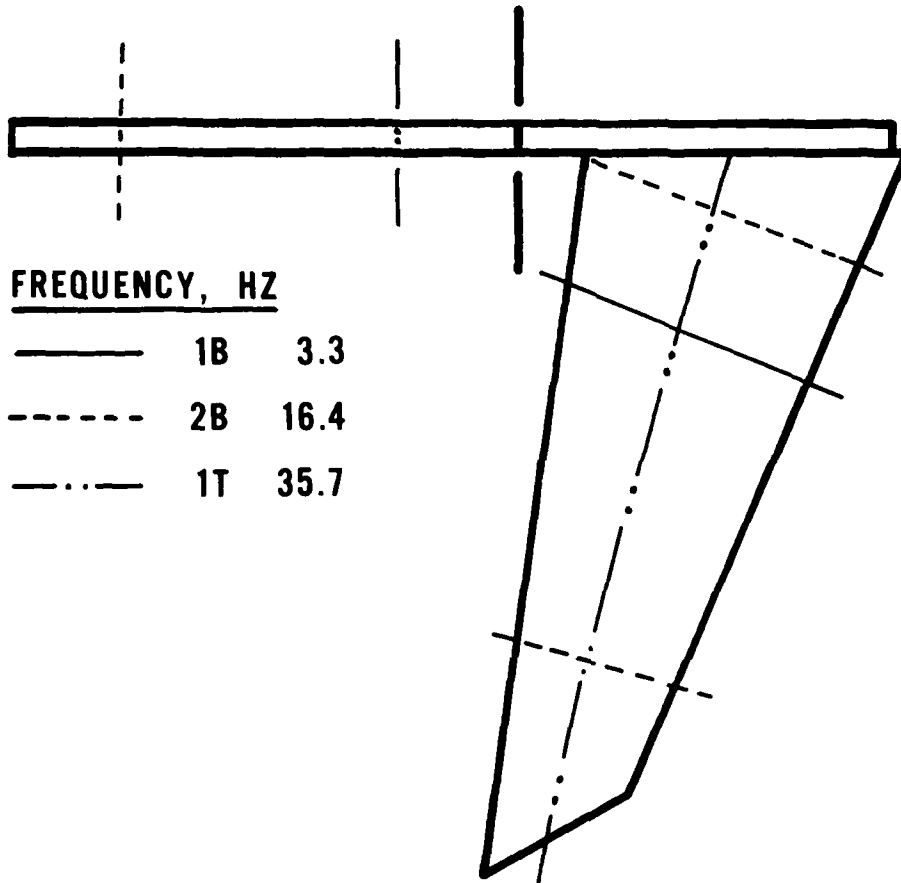Basic Model Free in Pitch

Figure A-4 Calculated Frequencies and Node Lines of
Basic Model Free in Pitch and Plunge

136

analysis to accomplish this objective.

Table A-4 and Figures 4 through 6 of the main text present the calculated frequencies and node lines of the modified model for the three wing boundary conditions. All natural frequencies are about 18 to 35 percent lower than the respective frequencies calculated for the basic model. Also the torsional node line has shifted significantly aft as a result of the masses near the trailing edge.

Flutter Analysis

The subsonic doublet lattice theory was used to calculate the unsteady aerodynamic force coefficients for the flutter and divergence analyses. The k-method was used for the cantilever aeroelastic analyses where zero frequency divergence was of concern. This method provided answers that correlated well with test data and other static aeroelastic analysis results. When the model was in a free-free state, both the k-method and the P-k method were considered for flutter calculations. The P-k method was subsequently eliminated when an aerodynamic interpolation problem was encountered. This problem is discussed in more detail in Appendix B.

Figure 3 of the main text shows the aerodynamic paneling arrangement used in these studies. Two of the outboard panels represent the leading edge and the trailing edge control surfaces. The locations of these

137

Table A-4   Modified Model Calculated Frequencies

ROOT CONDITION	MODE	ANALYSIS (HZ)
CANTILEVER	1B	2.4
	2B	12.6
	1T	23.6
	3B	34.3
FREE IN PITCH	1B	2.3
	2B	12.5
	1T	23.1
	3B	33.4
FREE IN PITCH AND PLUNGE	1B	2.6
	2B	13.1
	1T	23.1
	3B	34.0

two control surfaces relative to the model aerodynamic sleeves are shown in Figure A-5.

Damping versus velocity and frequency versus velocity plots for the basic and modified model for the three wing boundary conditions are found in Figures A-6, A-7 and A-8. These figures show only the first three elastic modes. A modal elimination analysis indicated that the fourth elastic mode (3rd bending mode) had little or no effect on the prediction of the divergence and flutter characteristics. Table A-5 summarizes the flutter and divergence calculations for the basic and modified models.

COORDINATES OF CONT SURF

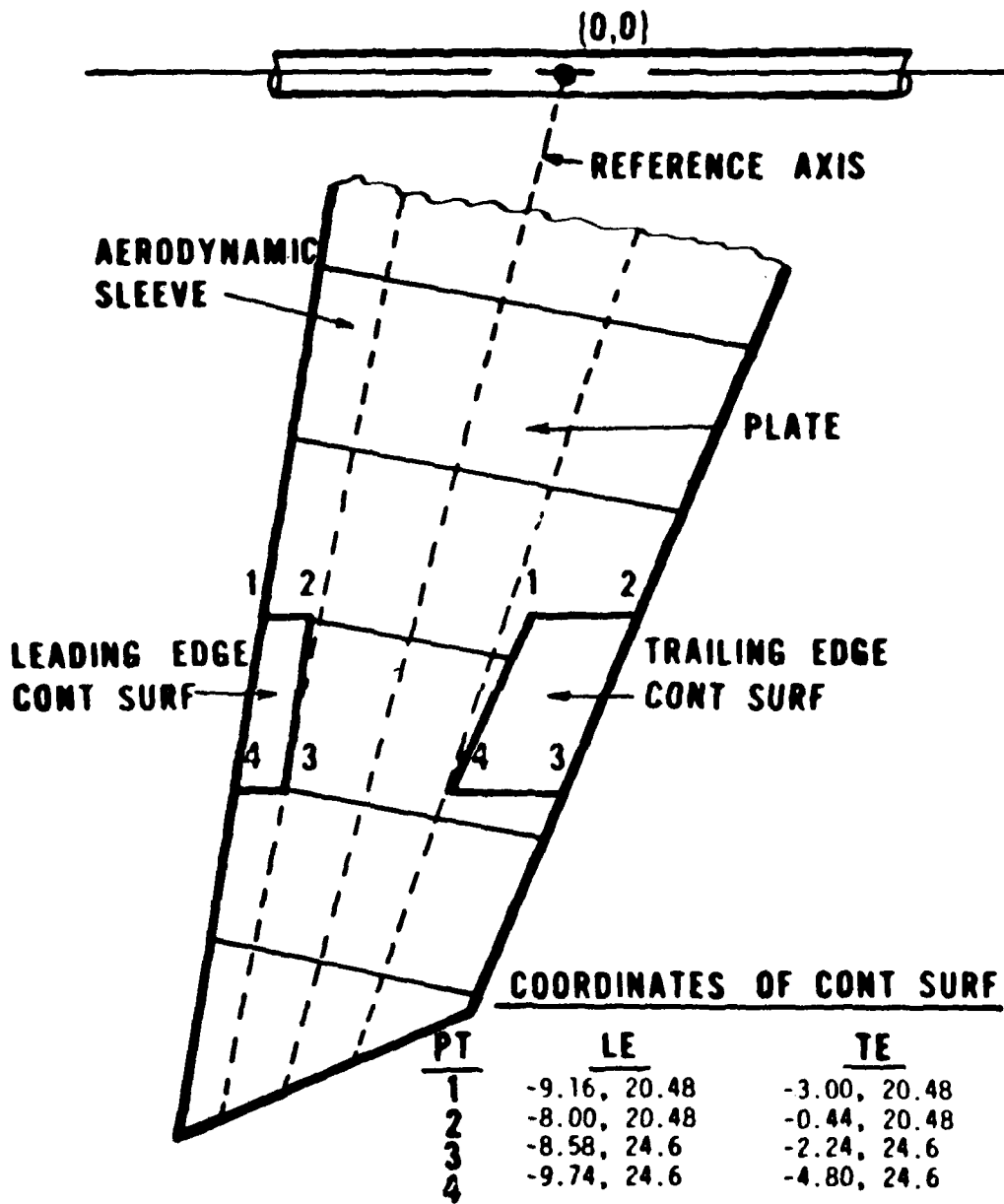| PT	LE	TE
1	-9.16, 20.48	-3.00, 20.48
2	-8.00, 20.48	-0.44, 20.48
3	-8.58, 24.6	-2.24, 24.6
4	-9.74, 24.6	-4.80, 24.6

Figure A-5 Leading and Trailing Edge Control Surface Locations
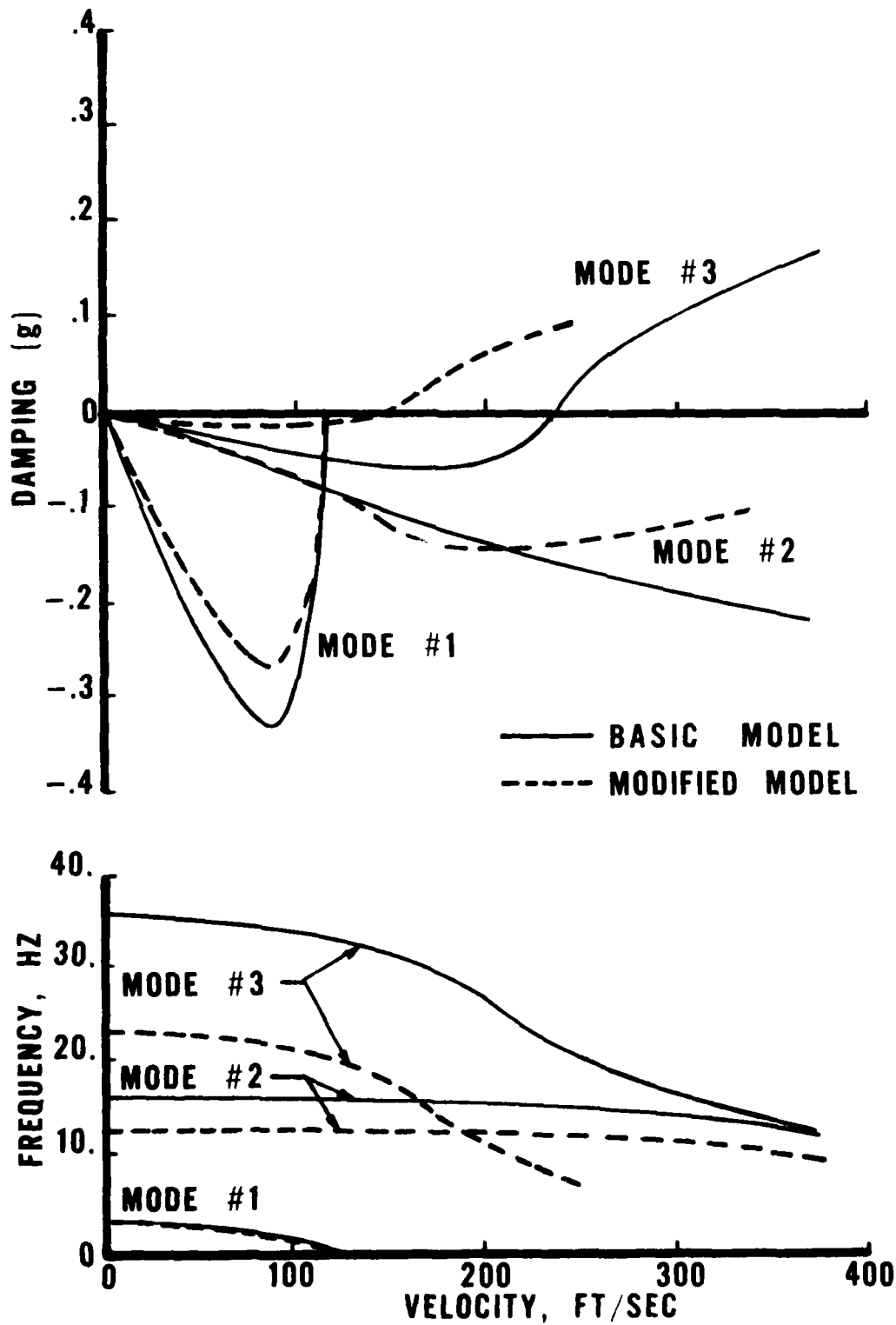Relative to Model Aerodynamic Sleeves

Figure A-6   Flutter Analysis Results for the Basic and Modified
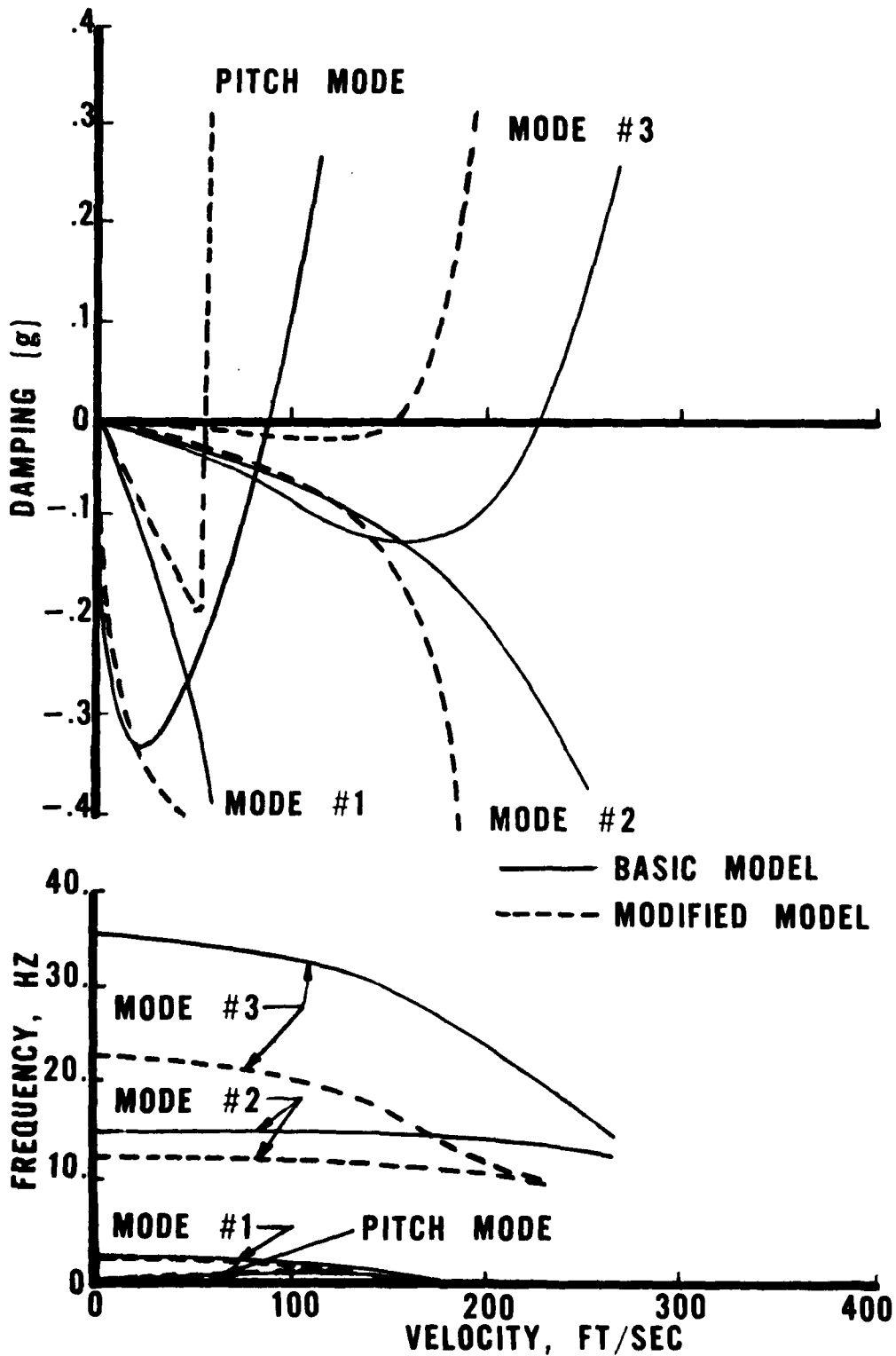Model, Cantilever Wing

141

Figure A-7   Flutter Analysis Results for the Basic and Modified Model, Model Free in Pitch
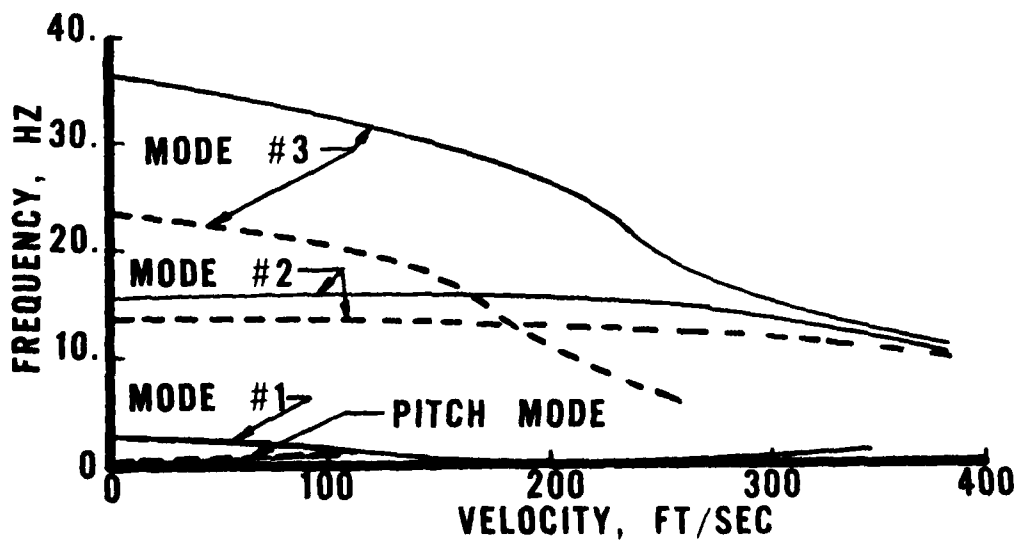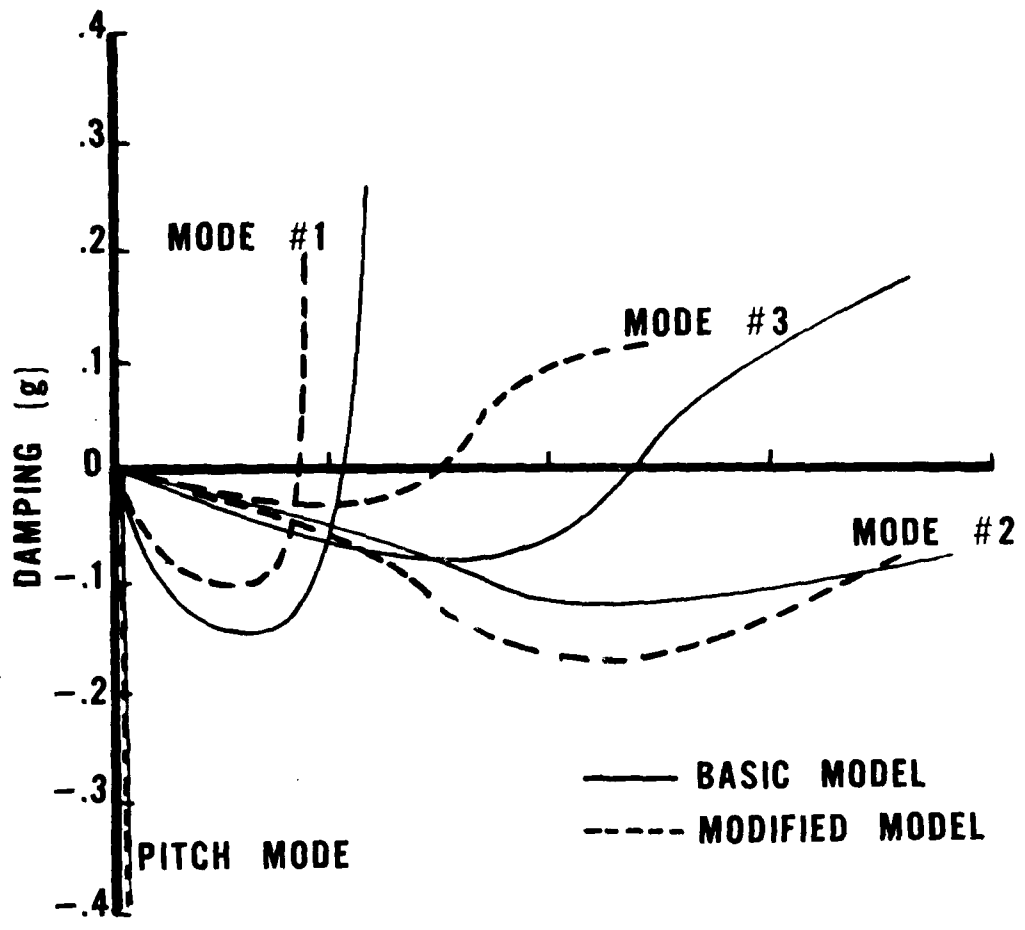
142

Figure A-8   Flutter Analysis Results for the Basic and Modified
Model, Model Free in Pitch and Plunge

Table A-5 Flutter and Divergence Analysis Results

CONFIGURATION		4 MODES	3 MODES
BASIC MODEL CANTILEVER	V_D	119	119
	V_f	155	155
	ω_f	16.9	16.9
FREE IN PITCH	V_{f_1}	53	53
	ω_{f_1}	1.2	1.2
	V_{f_2}	156	156
	ω_{f_2}	16.0	16.0
FREE IN PITCH AND PLUNGE	V_{f_1}	75	75
	ω_{f_1}	1.9	1.9
	V_{f_2}	153	153
	ω_{f_2}	16.5	16.5
MODIFIED MODEL CANTILEVER	V_D	119	119
	V_f	236	236
	ω_f	21.8	21.8
FREE IN PITCH	V_{f_1}	90	90
	ω_{f_1}	1.4	1.4
	V_{f_2}	227	227
	ω_{f_2}	20.8	20.8
FREE IN PITCH AND PLUNGE	V_{f_1}	105	105
	ω_{f_1}	1.7	1.7
	V_{f_2}	238	235
	ω_{f_2}	20.9	21.0

V, FT/SEC ; ω , HZ

144

APPENDIX B

VARIATION OF UNSTEADY AERODYNAMIC FORCES WITH REDUCED

FREQUENCY

One of the more surprising aspects of performing a flutter analysis for the model free in rigid pitch concerned the interpolation of the unsteady aerodynamic forces. It was found that the prediction of the body freedom flutter characteristics was very dependent on the selection of the reduced frequencies used during the calculation of the unsteady aerodynamic forces. Figure B-1 illustrates a potential concern (rapid variation of the force coefficient in a small reduced frequency range) that could be overlooked during a body freedom flutter analysis. This figure presents a variation of the aerodynamic force in the rigid pitch mode due to the pressure caused by the rigid pitch mode as reduced frequency was varied. The region of interest lies between a reduced frequency of 0.1 to 0.2, the range in which body freedom flutter occurred.

Initially, a P-k flutter analysis approach was used to predict body freedom flutter. This technique required the calculation of aerodynamic forces at several reduced frequencies which covered the frequency and velocity ranges of interest. An interpolation of
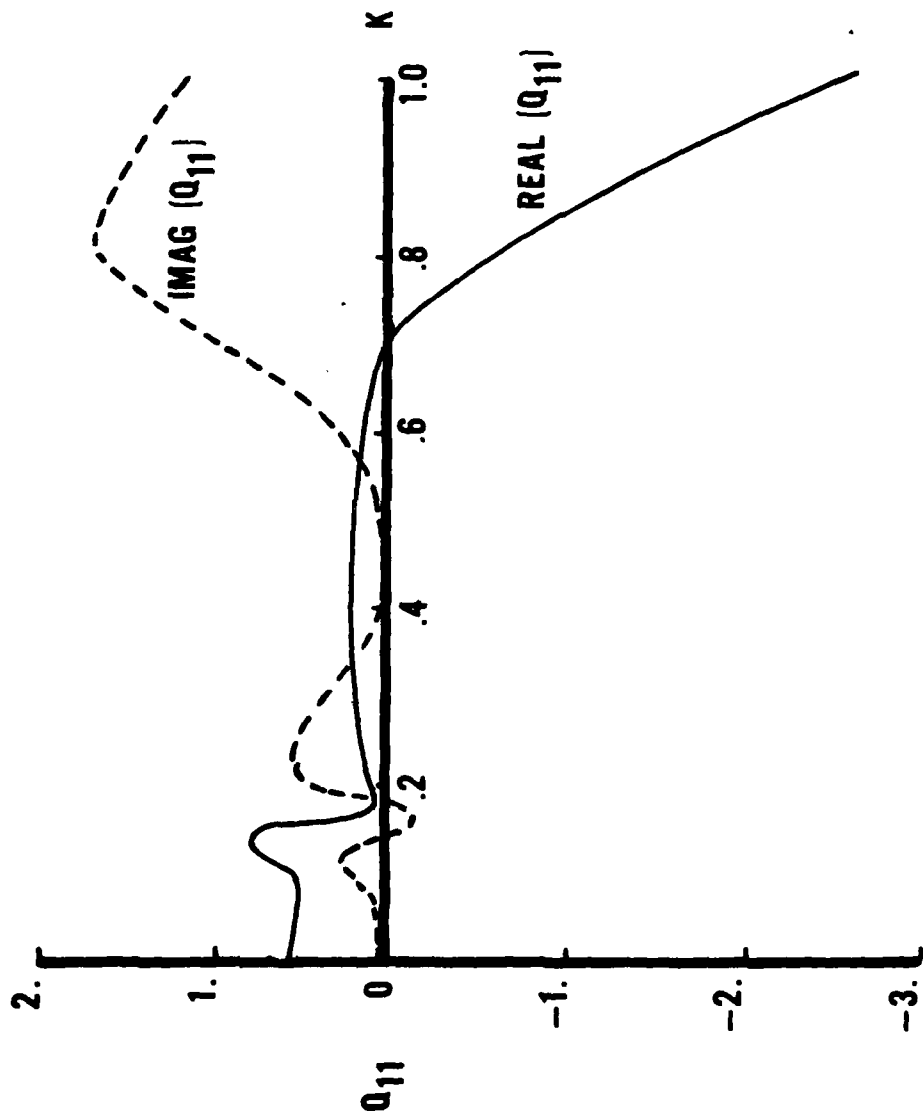
Figure B-1 Variation of Rigid Body Pitch Aerodynamic Force
Coefficient with Reduced Frequency

146

aerodynamics based on these calculated forces was used in the P-k analysis. For the model free in pitch, two dynamic instabilities were in the speed range of interest. The high frequency bending/torsion flutter mode occurred near a reduced frequency of 0.7. As a result, the P-k flutter analysis was conducted using aerodynamic force coefficient data calculated at reduced frequencies between .05 to 1.0. Since only six values could be used in the flutter analysis procedure for the P-k technique, this range of reduced frequencies selected appeared reasonable at the time. However, the rapid variation of this force coefficient (determined at a later time) could not be reproduced by aerodynamic interpolation and erroneous flutter results were obtained.

The P-k flutter analysis predicted a body freedom flutter instability 30 percent below the test speed for the basic wing discussed earlier. After undergoing a detailed inspection of the analyses and calculating aerodynamic force coefficients at additional values of reduced frequency, Figures B-1 thru B-6 were developed. Using a k-flutter prediction method and no aerodynamic force interpolation, the flutter speed was predicted to occur at 90 ft/sec which was only 4 ft/sec different from test data. This analysis was conducted using
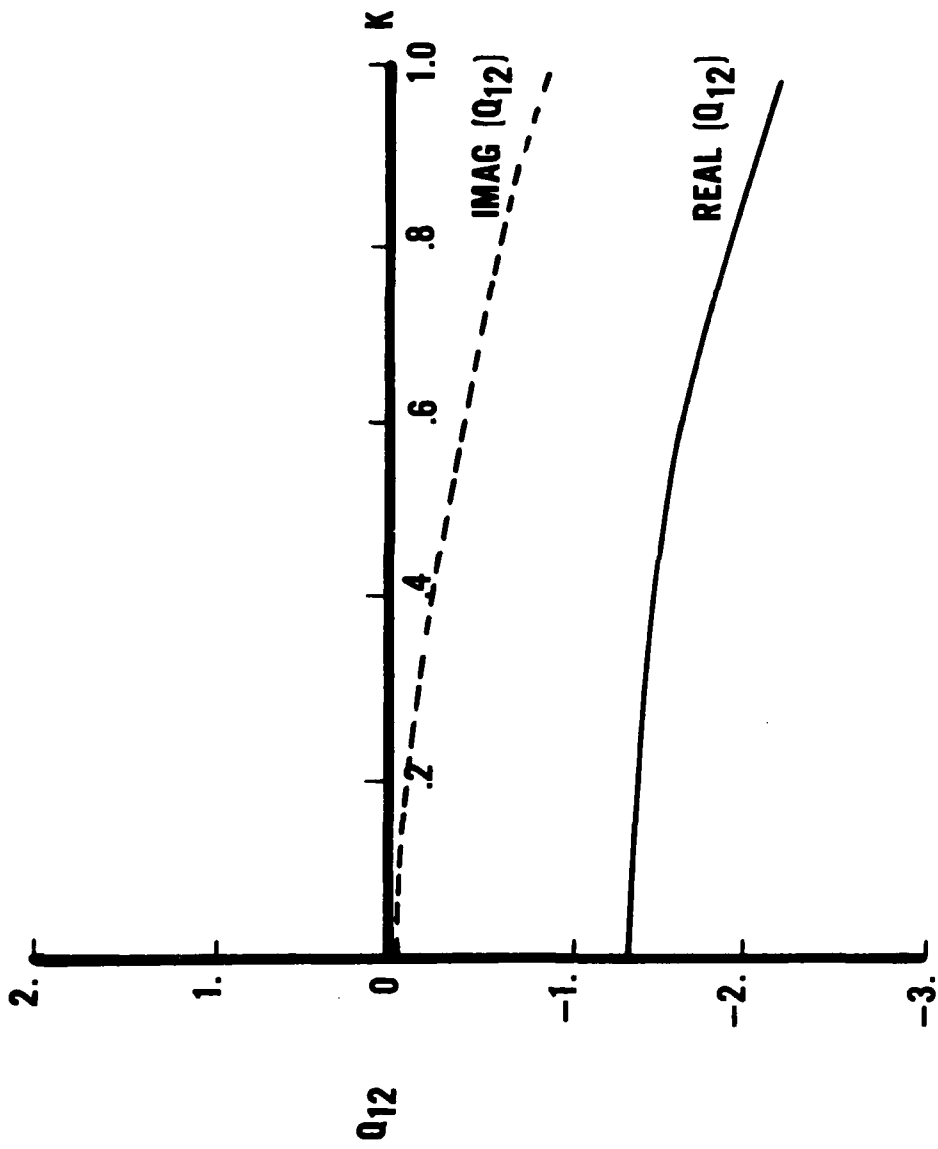
147

Figure B-2 Variation of Rigid Body Pitch/1st Bending Aerodynamic Force Coefficient with Reduced Frequency
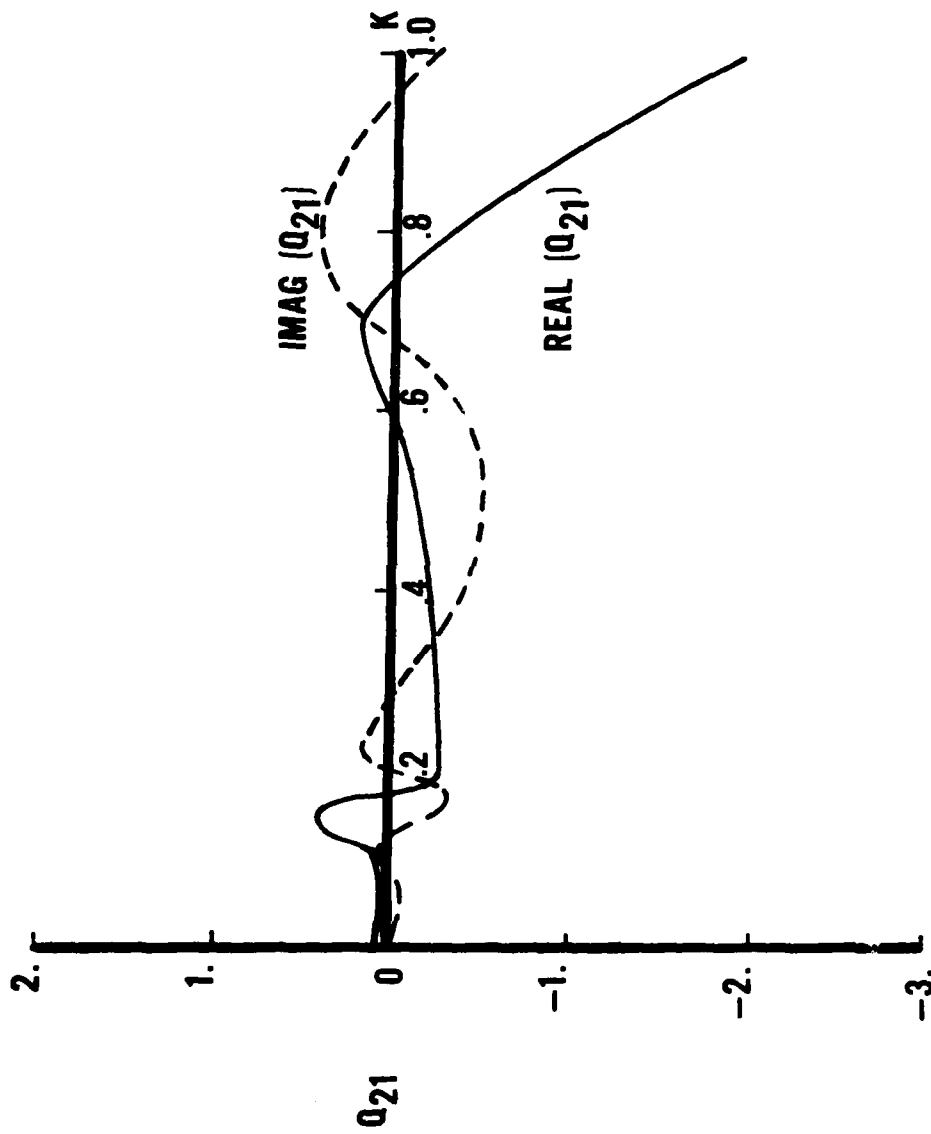
Figure B-3   Variation of 1st Bending/Rigid Body Pitch Aerodynamic Force Coefficient with Reduced Frequency
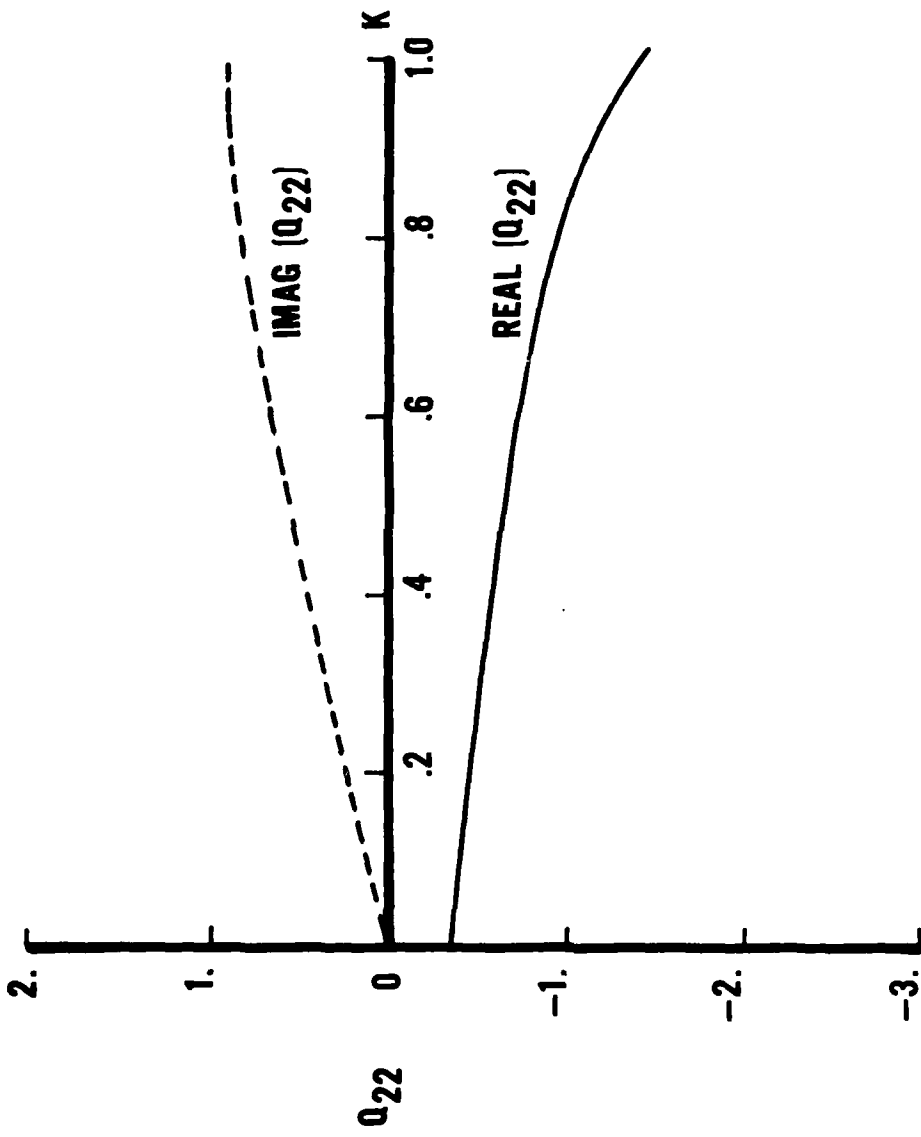
Figure B-4 Variation of 1st Bending Aerodynamic Force Coefficient with Reduced Frequency
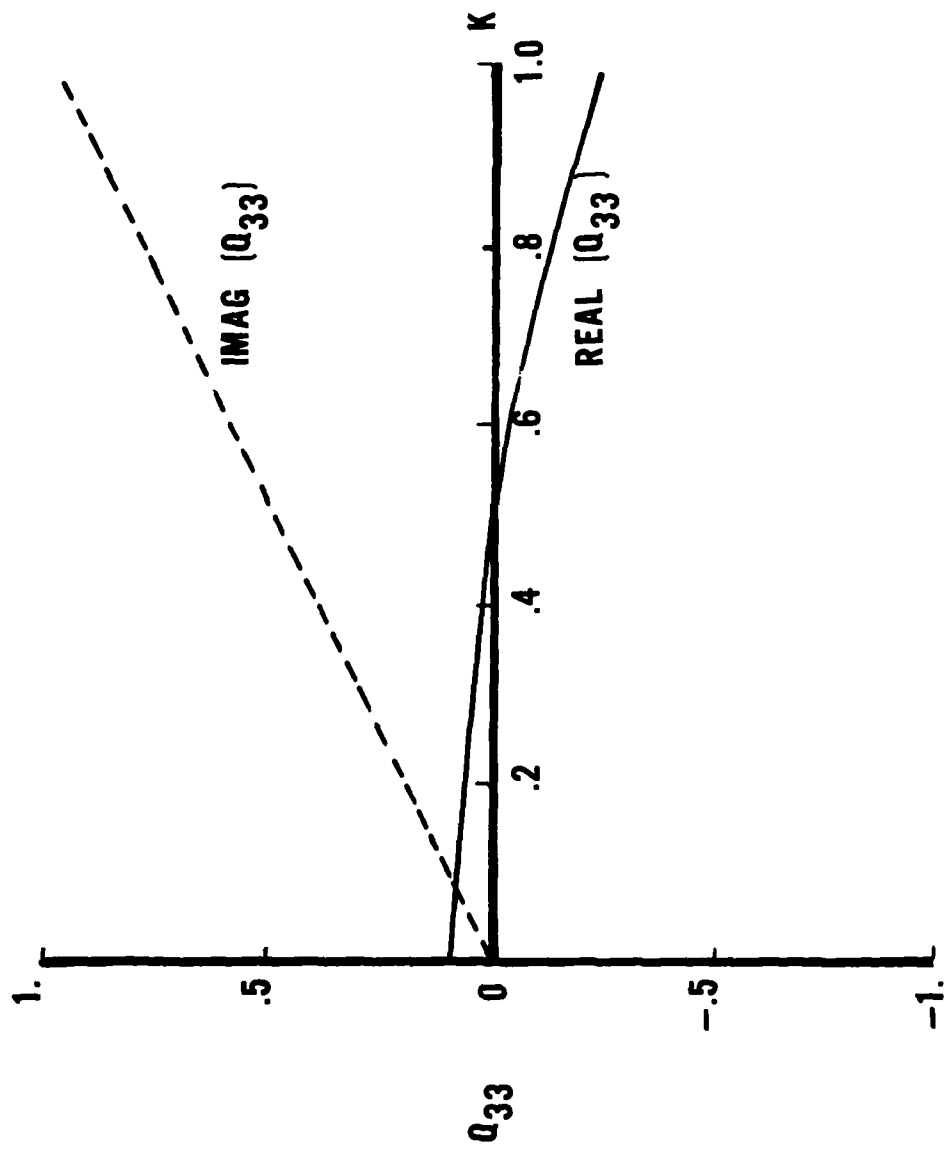
Figure B-5 Variation of 2nd Bending Aerodynamic Force Coefficient with Reduced Frequency
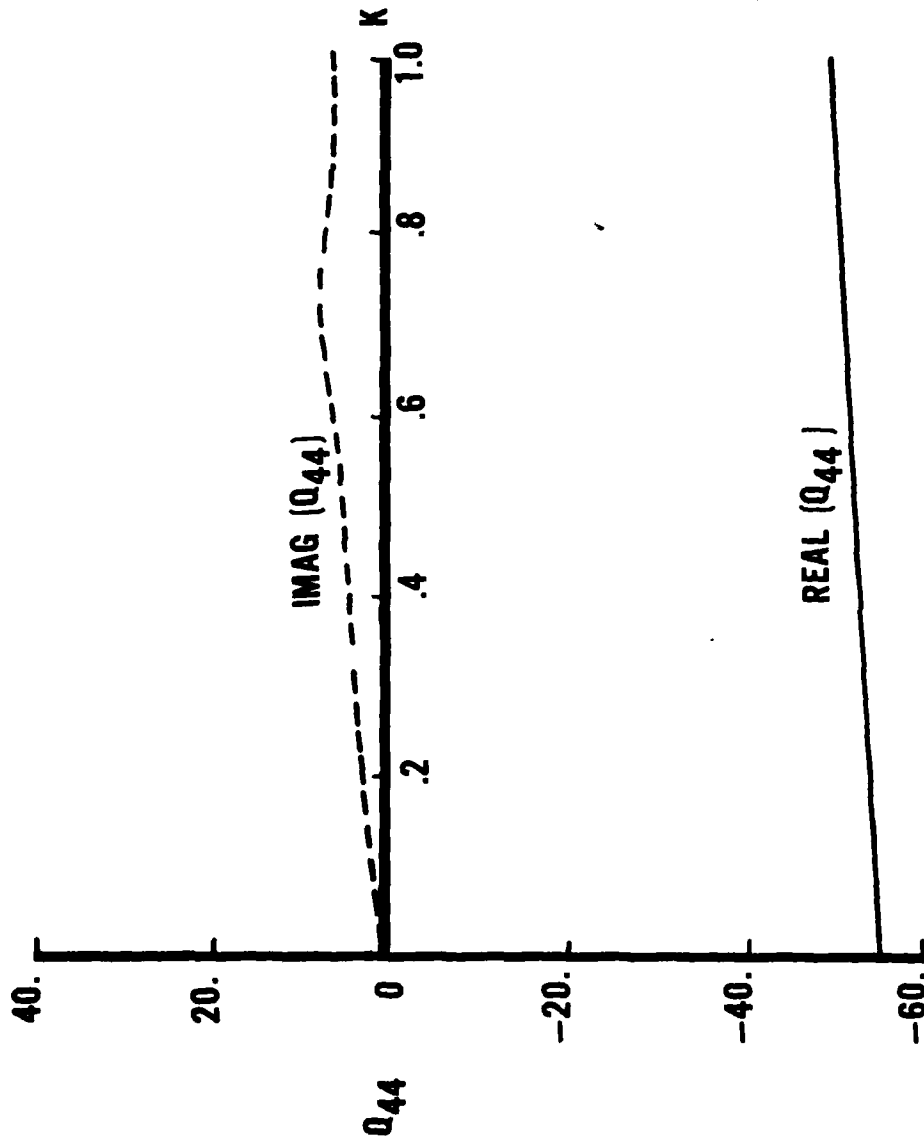
Figure B-6 Variation of Torsion Aerodynamic Force Coefficient with Reduced Frequency

aerodynamics calculated at every .005 reduced frequency increment between 0.1 to 0.2. The prediction of the higher frequency flutter mode did not involve rapidly varying aerodynamics over a narrow k range which is normal for most flutter modes and, therefore, was not a problem for either technique.

The above experience implies that when performing flutter analyses with rigid modes, care must be taken to assure that the aerodynamic force coefficients due to the rigid modes are properly represented over the reduced frequency range of interest. This is particularly true if any of the rigid modes are expected to participate in the flutter mode such as body freedom flutter. Without care, at best overly conservative flutter speeds may be predicted as was the case reported here. It is quite possible, however, that the instability may not be predicted at all, resulting in later potentially serious problems.